Summer 8-2-2012

II-VI Core-Shell Nanowires: Synthesis, Characterizations and Photovoltaic Applications

Kai Wang
kwang1@uno.edu, kwang1@uno.edu

II-VI Core-Shell Nanowires:
Synthesis, Characterizations and Photovoltaic Applications

A Dissertation

Submitted to the Graduate Faculty of the
University of New Orleans
in partial fulfillment of the
requirements for the degree of

Doctor of Philosophy
in
Engineering and Applied Science
Physics

by

Kai Wang

M.S. Southwest Jiaotong University, 2006
B.S. Southwest Jiaotong University, 2003

August, 2012

To my family

Acknowledgments

In the first place I would like to record my greatest gratitude to my advisor, Prof. Weilie Zhou, for his guidance, advice, supervision throughout the work, for the continuous encouragement and support he provided in various ways, and for the opportunities he offered to me to broaden my horizons and enrich my life experience. I am indebted to him more than he knows.

I gratefully thank the academic committee members: Prof. Leszek Malkinski, Prof. Kevin Stokes, Prof. Paul Schilling and Prof. Ashok Puri for their valuable discussion, insightful suggestion and constructive comment during my study, research, and, especially, on this dissertation.

I gratefully acknowledge Prof. Yong Zhang for his advice and crucial contribution to this dissertation. His involvement with his originality has triggered and nourished my intellectual maturity that I will benefit from.Many thanks go in particular to Dr.Yanfa Yan and Dr. John Pern. I am much indebted to Dr.Yanfa Yan for allowing me to the field-emission Transmission Electron Microscopy and his constant support on the structure analysis. I have also benefited by helpful advice from Dr. John Pern.

I would like to extend my appreciation to the previous and present members in Prof. Zhou's group. My special thanks go to Dr. Jiajun Chen for being the first person who taught me how to work in nanostructure synthesis. I am very grateful to Dr. Zhongming Zeng, Dr. Kun Yao, Dr. Baobao Cao, Dr. Ying Li for their kindly help and support on the device fabrication and TEM analysis. I would also acknowledge Renhai Long, Jie Zhou, Hui Ma, Haiqiao Su, Satish Rai, Sarah Wozny and Zhi Zheng for their advice and their willingness to share their bright thoughts with me.

It is a pleasure to express my appreciation to my friends, Jingjing Liu, Sikai Chen and Haiou Qu, for the happy time we enjoyed together and the tough time they supported me.

My parents, who are always proud of their son, deserve special mention for their inseparable support and encouragement and for their endless love and understandings. Thanks my sister,

Wenxiu Wang, for being supportive and caring sibling in all the aspects of my study. Words fail me to express my appreciation to my wife, Yan Huang, whose dedication, love and confidence in me, has taken the load off my shoulder. I owe her a lot for the sacrifices she made for our family.

Finally, I would like to thank AMRI for continuous support of graduation assistantship. I grateful acknowledge the financial support from the DARPA Grant No.HR0011-07-1-0032, research grants from Louisiana Board of Regents Contract No. LEQSF (2008-11)-RD-B-10 and American Chemical Society Petroleum Research Fund PRF No 48796-DN110.

List of Figures

heterointerface. The interfacial emission energy is determined by Eg12. (b) Electronic energy levels of selected II-VI and III-V semiconductors showing the materials selection to construct type II heterojunction.

Figure 3.2 (a) SEM image of a well-aligned ZnO nanowire array grown on TCO substrate by CVD. The average length of the nanowires is about 10 μm and the diameters are about 100 nm. (b) SEM image of well-aligned ZnO/ZnSe Core-shell nanowire array prepared by PLD. The insets in (a) and (b) are enlarged images of ZnO nanowire and Core-shell nanowire tips, respectively.

Figure 3.3 XRD patterns of ZnO and ZnO/ZnSe nanowire arrays. The inset shows clear peak shifting of ZnO/ZnSe to low angle region.

Figure.3.4 Low magnification TEM micrograph of a ZnO/ZnSe Core-shell nanowire. A thin layer of ZnSe was coated on the ZnO nanowire. b) High resolution TEM image of the interface of the Core-shell heterostructure, enlarged from the rectangular area in (a), showing the epitaxial growth relationship of ZnO wurtzite core and ZnSe zinc blende shell. c) and d) Fast Fourier transfer (FFT) patterns of rectangular areas in (b). e) EDS nanoprobe line-scan on elements Zn, Se, and O, across the ZnO/ZnSe Core-shell nanowire, indicated by a line shown in (a).

Figure.3.5 TEM images of room temperature PLD deposited ZnSe shell on ZnO nanowire. (a) Low-magnification TEM image. (b) High resolution image enlarged from rectangular area in (a). (c) Corresponding fast Fourier transformation (FFT) pattern, indicating the ZnSe shell is polycrystalline without epitaxial growth.

Figure 3.6. Transmission spectra of ZnO nanowires and corresponding ZnO/ZnSe core-shell nanowires. Two vertical lines indicate the excitonic bandgap of bulk ZnO and ZnSe, respectively.

Figure 3.7. (a) Photoluminescence and (b) Raman spectra of ZnO and ZnO/ZnSe nanowire arrays, compared with those of a bulk single crystal ZnO.

Figure 3.8. Photo-conductivity spectra for a single ZnO/ZnSe nanowire measured under different biases and at different days. The inset shows the SEM picture of the single-nanowire device for photo-response measurements.

Figure 3.9 (a) Low-magnification SEM image of a well-aligned ZnO nanowire array grown on TCO substrate by chemical vapor deposition. The average length of the nanowires is about 7 μm and the diameters are about 50~120 nm. (b) and (c) Magnified SEM images of bare ZnO and ZnO/ZnS Core-shell nanowire arrays, respectively. (d) XRD patterns of ZnO and ZnO/ZnS nanowire arrays.

Figure 3.10 Structural characterization of ZnO/ZnS core-shell nanowire array. (a) Low-magnification TEM micrograph of a ZnO/ZnS core-shell nanowire, showing a thin layer of ZnS coated on the ZnO nanowire. (b) High-resolution TEM image of the interface of the Core-shell heterostructure, enlarged from the rectangular area in (a), showing the epitaxial growth relationship of ZnO wurtzite core and ZnS zinc-blende shell. (c) and (d) Atomic resolution

and (d) Low magnification TEM images of ZnTe nanowires, implying two different microstructures. (e) and (f) HRTEM images of ZnTe nanowire, corresponds to the frame marked in (c) and (e), respectively. The native oxide layer was highlighted by dash line.

Figure 5.2 Structure analysis of ZnTe/CdSe nanowires.(a) Low magnification TEM images of ZnTe/CdSe nanowires.(b) and(c) HRTEM images of CdSe nanocrystals epitaxially grown over ZnTe nanowires. (c) Interface of ZnTe/CdSe nanowire exhibiting epitaxial relationship. (e)A low magnification TEM images of ZnTe/CdSe nanowires showing the inhomogeneous coating because of non-alignment. (f) Nanoprobe EDS result recorded along the dash line marked in (e).

Figure 5.3 Structure analysis of CdSe nanowires synthesized at 450^{o}C. (a) and (b) SEM images of CdSe nanowires collected after 5 min and 10 min laser ablation. (b) Low magnification TEM image of CdSe nanowires collected after 5mins laser ablation. (d) High magnification TEM image from the frame labeled in (c), showing both stacking sequence of zinc blende and wurtzite structure.

Figure 5.4 (a) and (b) low and high magnification SEM images of CdSe nanostructures synthesized by laser ablation with a higher energy flux. (c) Low magnification TEM image of CdSe nanostructures, showing nanowires, nanobelts and branched structures. (d)~(f) Representative TEM images of CdSe nanowires with growth directions, [0002], [$01\bar{1}0$] and [$\bar{1}010$], respectively.(g)~(i) SEAD patterns recorded from the CdSe nanowires labeled the growth direction in (d)~(f),respectively.

Figure 5.5 (a) SEM image of low density rigid CdSe nanowires synthesized by thermal evaporation. Inset is the high magnification image showing the catalysts on the tip of nanowires. (b)cross-section of CdSe nanowires directly grown on a thick CdSe oriented layer.(c) TEM image of an individual CdSe nanowire with a catalyst on the tip.(d) HRTEM of CdSe nanowire taken from the frame in (c). Inset displays the corresponding FFT of the high magnification image.

Figure 5.6 XRD pattern of CdSe nanowires collected on silicon substrate.

Figure 5.7 SEM images of CdSe/ZnTe core-shell nanowires (a) top-view and (b) cross-section.

Figure 5.8 (a) Low magnification TEM image of CdSe/ZnTe core-shell nanowires.(b) A representative TEM image of an individual CdSe/ZnTe core-shell nanowire, clearly showing the smooth surface and core-shell geometry.(c) HRTEM images of a typical core-shell interface manifesting the epitaxial growth relationship of $CdSe_{WZ}$ and ZnTe $_{WZ}$; Inset shows the FFT of the area marked as dashed frame ; (c) Ball and stick model of the relaxed CdSe (WZ) /ZnTe (WZ) structure. (d) Nanoprobe EDS scanning along the line marked in(b), suggesting the conformal shelling and absence of interfacial diffusion.

Figure 5.9 (a) and (d) AFM images of an individual CdSe and CdSe/ZnTe core-shell nanowire. (b) PL image of a single CdSe nanowire. (c) A spectrum of CdSe nanowire collected from the area marked by circle in (b). (e) Band diagram of CdSe/ZnTe core-shell nanowires, displaying the charge separation and possible interfacial transition.

Figure 5.10 Schematics of the procedures for fabricating a PV device based on an individual core-shell nanowire.

Figure 5.11 (a) SEM image of an individual CdSe/ZnTe core-shell nanowire solar cell. (b) Current-Voltage (*I-V*) characteristics for efficiency extraction. (c) Photoresponse of nanowire device at 0V bias.

Figure 5.12 (a) 30^{o} tilted view and (b) top-view of SEM images of CdSe nanowire array. (c) High magnification SEM image showing gold catalyst on tips of nanowires. (d)~(f) CdSe nanowire array harvested on different area of mica substrate.

Fig.5.13 XRD patterns of muscovite mica, mica with CdSe seed layer and mica with CdSe nanowire array, clearly showing that both CdSe seed layer and CdSe nanowire array have a preferential growth direction along (002).

Figure 5.14 Raman spectra from muscovite mica, mica with CdSe seed layer and mica with CdSe nanowire array, respectively. Inset shows large magnification section to highlight the LO mode of nanowire located at 206 cm^{-1}.

Figure 5.15 (a) and (b)SEM images of CdSe nanostructures collected on muscovite mica without any seed layer and catalysts.(c)and(d) low and higher magnification SEM images of CdSe nanowires obtained on mica substrate with 150 nm CdSe seed layer.

Figure 5.16 SEM images of (a) 200nm gold colloids dispersed on CdSe seed layer coated mica substrate. (b) CdSe nanostructures catalyzed by gold colloids. (c)and(d) low and higher magnification SEM images of CdSe nanowires with patterned catalysts via a TEM copper grid.

List of Tables

Table of Contents

Abstract

The emergence of semiconducting nanowires as the new building blocks for photovoltaic (PV) devices has drawn considerable attention because of the great potential of achieving high efficiency and low cost. In special, nanowires with a coaxial structure, namely, core-shell structures have demonstrated significant advantages over other device configurations in terms of radial charge collection and cost reduction. In this dissertation, several core-shell nanowire structures, including ZnO/ZnSe, ZnO/ZnS, and CdSe/ZnTe, have been synthesized and the photovoltaic devices processed from a ZnO/ZnS core-shell nanowire array and a single CdSe/ZnTe core-shell nanowire have been demonstrated.

By combining the chemical vapor deposition and pulsed laser deposition (PLD) techniques, type-II heterojunction ZnO/ZnSe and ZnO/ZnS core-shell nanowire array were synthesized on indium-tin-oxide substrates. Their structures and optical properties have been investigated in detail, which revealed that, despite highly mismatched interfaces between the core and shell, both systems exhibited an epitaxial growth relationship. The quenching in photoluminescence but enhancement in photocurrent with faster response upon coating the core with the shell provides the evidence that the charge separation and collection in the type II core-shell nanowire is greatly improved. This demonstration brings much greater flexibility in designing next generation PV devices in terms of material selection and device operation mechanisms for achieving their maximum energy conversion efficiencies at a low cost and in an environmentally friendly manner.

In order to achieve a high quality interface in the core-shell nanowire, CdSe and ZnTe, which have close lattice parameters and thermal expansion coefficients, were chosen to fabricate nanowire solar cells. ZnTe and CdSe nanowires were first synthesized by thermal evaporation and the shells were subsequently deposited by PLD. ZnTe/CdSe nanowires represented an inhomogeneous coating while the CdSe/ZnTe core-shell exhibited a conformal coating with obvious ZnTe eptilayer. The final PV device based on an individual CdSe/ZnTe nanowire demonstrated an efficiency of ~1.7%. In addition, a controllable synthesis of CdSe nanowire array on muscovite mica substrate was presented, providing the possibility to harvest hybrid energies in an all-inorganic nanowire array.

Keywords: Solar Cells, Nanowires, Type-II heterojunction, Epitaxial growth, Three-dimensional

Chapter 1 Introduction and Background

1.1 Energy demand and solar energy

One can never underrate the importance of the energy issue, because, to some extent, the history of the human race is a history of energy exploration. In 2010, about 15 terawatts (TW) of energy was consumed to sustain the lifestyle of 6.15 billion people worldwide and 86% of the energy was supplied by the fossil fuels in the form of coal, oil and natural gas[1,2]. The world energy consumption rate can be roughly calculated as the product of world populations, world per capita gross domestic product (GDP), and world energy density. Assuming a global growth rate of about 0.9% per year, total energy demand in primary energy consuming countries will be doubled by 2050 and tripled by 2100 to maintain the current lifestyle[2]. Note that the urbanization in the developing countries, another important factor contributing to the energy demand, is not even taken into consideration. On the contrary, the finite reservoir of fossil fuels is depleting as the production of oil has recently peaked to the saturation point. Though the advance of technology may maximize the production of oil, an increase in the cost would certainly be startling. This also holds true to the production of coal and natural gas, according to the well-known Hubbert's prediction[3-5]. In other words, the fossil fuels used today will not be affordable in the near future. One major consequence of the reliance on fossil fuels is the global warming caused by the greenhouse effect. Carbon dioxide is released as a byproduct of the combustion of fossil fuels and around half of them remain in the atmosphere, which absorb the radiation from the earth and in turn lead to the increase of global temperature. Recently, reports have proven that the temperature of the earth has risen about 0.8^{o}C in the past century and this is believed to be accelerated in the coming decades[6]. The exponential demand of energy and the limitations in the usage of current fossil fuels force us to seek more alternative resources, such as nuclear and renewable energy (hydroelectricity, geothermal, wind power, ocean and tide current and solar energy). Nuclear power can generate a high amount of electricity in a single plant, but it is neither environmentally friendly nor sustainable. The Chernobyl and Fukushima Daiichi nuclear disasters have aroused the dispute over the development of nuclear power reactors. Solar power stands out above all available renewable energy resources primarily because of its abundance

and universal availability. The sun provides more energy to the earth in an hour than the world consumes in one year (2002).

1.2 The basics of solar cells

Currently, three approaches have been explored to harvest the solar energy and they are solar electricity, solar fuels and solar thermal. Solar cells, namely, photovoltaic (PV) cells, are optoelectronic devices which convert light to electricity. Energy conversion in solar cells is shown to consist of four steps, i.e., light (photon) absorption, exciton creation, exciton separation to free carriers, and carrier collection by electrodes. The first two steps take place in every semiconductor but the latter two steps require structure and force to directionally drive the electrons and holes as current[7]. A solar cell structure can be depicted as a *p*-*n* homojunction, as shown in Figure 1.1(a).

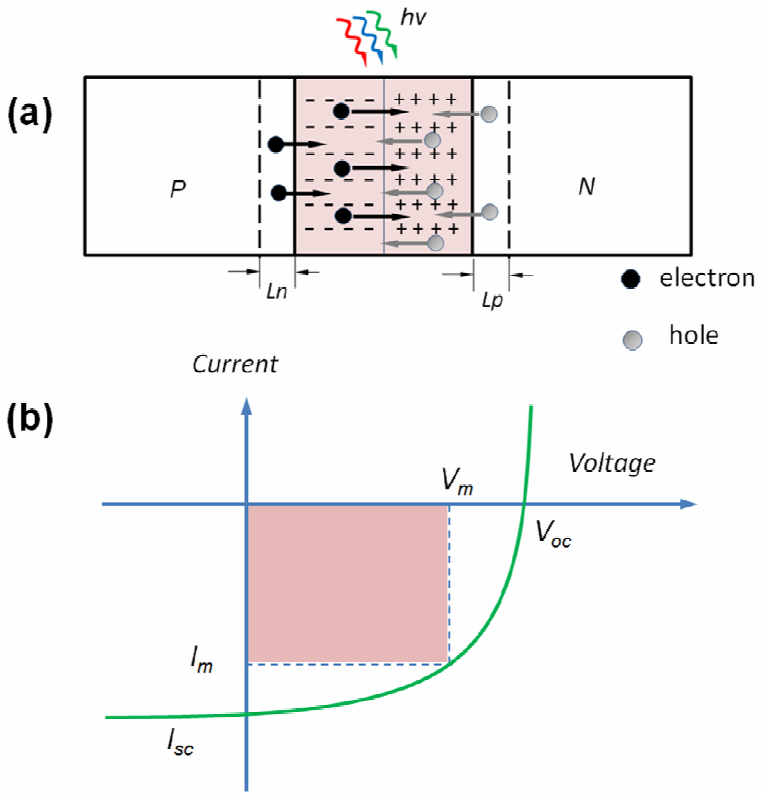

Figure 1.1 (a) Schematic illustration of carrier dynamics in a *p*-*n* junction illuminated by light. (b) A typical current-voltage (*I*-*V*) characteristics of a solar cell under illumination. The maximum-power of the solar cell is indicated by the dashed lines.

Once the *p-n* junction is irradiated by the sun light, electron-hole pairs (namely, the excitons) are created by the photons with energy greater than the bandgap, and the number of excitons is proportional to the light intensity. Owing to the presence of the built-in field in the depletion region, the electrons and holes tend to drift towards *n*- and *p*-side, respectively, which is, in fact, charge separation. This results in current flow from *n*- to *p*-side when an external wire is short-circuited and generation of voltage when the *p-n* junction is open-circuited. Because the excess carriers can diffuse up to the space charge region, the electron-hole pairs created within a distance of diffusion length from the edge of the depletion region also contribute to the photo current. From the *I-V* characteristics of a solar cell under illumination in the forth quadrant, as displayed in Figure 1.1(b), the efficiency of the solar cell, η, can be extracted as $\eta = (V_{oc} \times I_{sc} \times FF) / P_{in}$, where fill factor $FF = (V_m \times I_m) / (V_{oc} \times I_{sc})$. The short-circuit current (I_{sc}) is a direct measure of the conversion efficiency from incident photons to electrical current. The open-circuit voltage (V*oc*) is determined by the balance between the corresponding photogeneration rate and the net rate of radiative recombination within the cell.

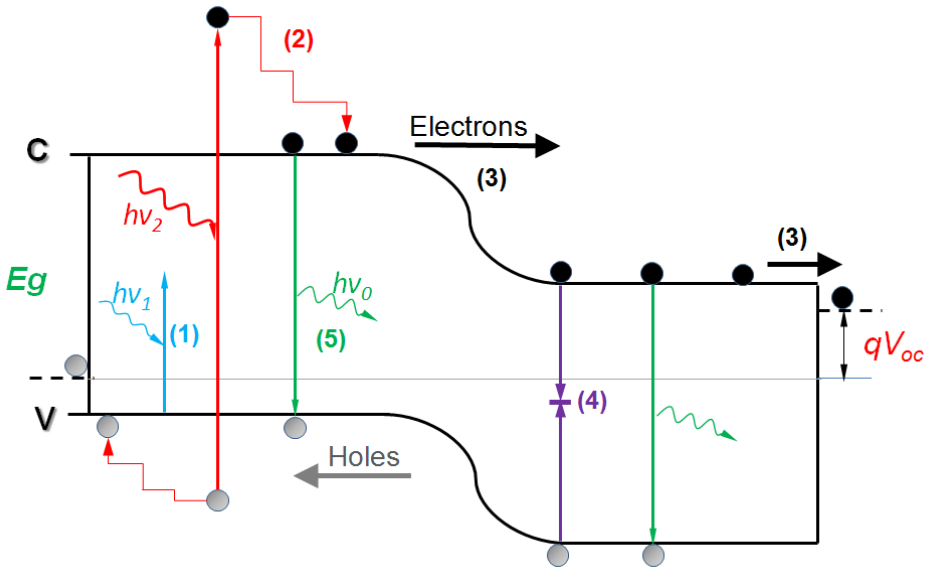

Figure 1.2 Energy band diagram of a *p-n* homojunction solar cell showing the major loss mechanisms. (After reference[8].)

The energy conversion efficiency of a solar cell is limited because of the energy loss occurring in all of the energy-conversion steps. Taking a single *p-n* homojunction solar cell for example, the origin of most energy loss, upon light illumination, is displayed in Figure 1.2. First, incoming photons with energies below the bandgap of the device, $hv_1<E_g$, are not absorbed, which was represented as (1). Second, incoming photons with energy above the bandgap are absorbed, however, the excess energy, hv_2-Eg, is wasted as heat, as shown as (2). Additional energy loss (3) occurs as the photoexcited carriers cross the junction and contact regions. Process (4) represents electronic states within the bandgap, such as defects or impurity atoms, which act as active centers where electrons and holes recombine. Process (5) represents the radiative recombination of the electrons and holes. Note that, in the ideal case, this is not considered as energy loss because the emitted photons could be reabsorbed elsewhere in the cell. However, in practical solar cells, photons emitted from the front of the cell back towards the incoming sunlight are lost forever, which ultimately limit the maximum efficiency of the cells[8,9].

The aforementioned energy losses are depicted based on the assumption that all the photons that strike solar cells are absorbed. In real solar cells, part of the photons is reflected. For instance, as shown in Figure 1.3(a), only 70% of solar energy can be collected for the energy conversion, given the fact that bare silicon wafer has a reflectivity of ~30%. Several strategies have been developed to suppress these losses. Because sun light is polychromatic, fixing the bandgap gives a tradeoff between energy losses (1) and (2)[9]. In these regards, it is well-known to use multiple-junction, intermediate band and spectrum conversion approaches to maximize the light absorption in a wide range of light profiles. With respect to energy loss (2), a novel concept to harvest the hot carriers has been developed and will be discussed in Section 1.3.1. In order to reduce the energy loss (4), high purity materials are generally required to minimize the boundaries and other defects. Surface texturing or depositing an antireflection layer on bare silicon allows for reducing of the overall reflection down to several percent. Figure 1.3 (b) shows the light trapping effect of the textured surface of silicon. Other than being reflected backward, light incident on the side of a pyramid will be reflected onto another pyramid [10].

In a planar *p-n* junction solar cell, as shown in Figure 1.3 (c), the thickness of the absorber, L, must be larger than the optical thickness of the absorbers, ($1/\alpha$), to absorb most of the light. The minority carrier diffusion length, L_n or L_p, (Here is L_n in the schematic) must be also larger than $1/\alpha$. in order to efficiently collect the photogenerated carrier. In general, low quality materials

have a low minority carrier diffusion length because of the presence of high density of defects or high level of impurities. New concepts have been proposed to optimize the device design to reduce the stringent material purity and quality requirements. Of great interest is decoupling the requirements for light absorption and carrier extraction into orthogonal spatial directions. A good example is the design of parallel multi-(*p*-*n*)-junction solar cell, where the *n* and *p* type material is assembled as "interdigital electrodes". This architecture offers more junction areas, and the merit lies in the fact that photogenerated minority carriers have a high possibility of reaching the junction before recombination, thus enhancing the charge collection[11].

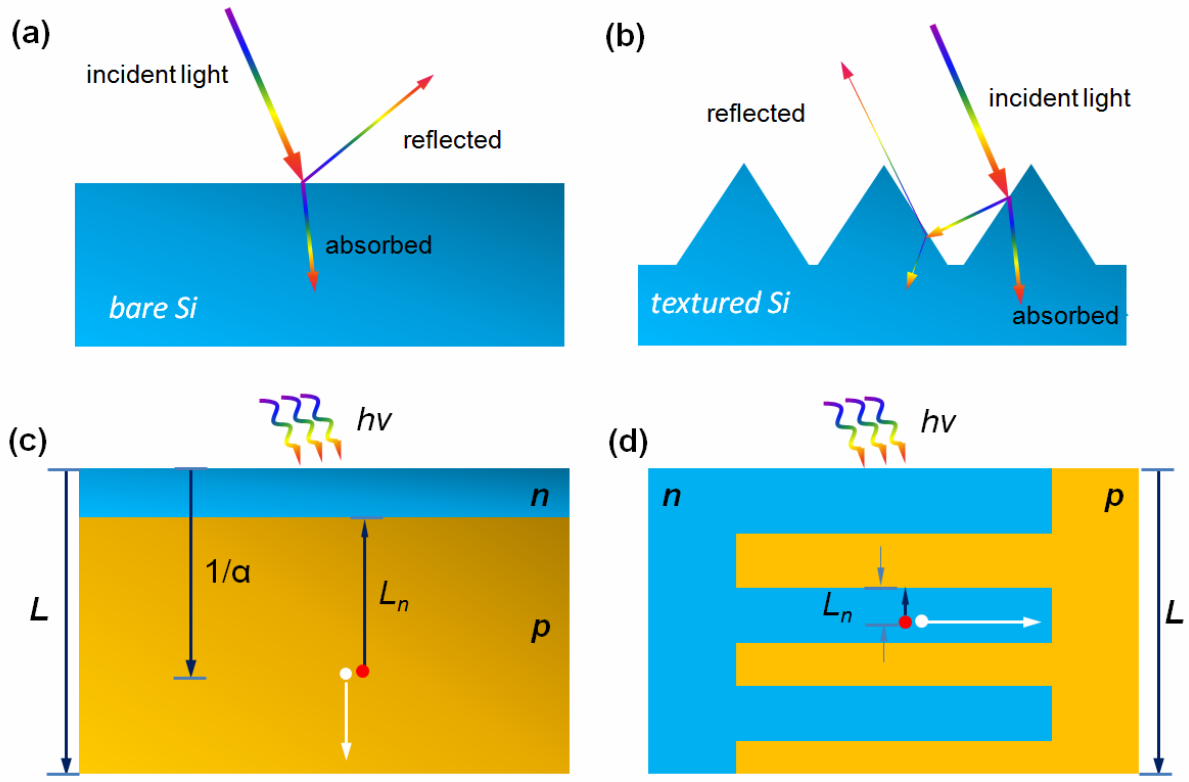

Figure 1.3 (a) Schematic of light illuminates on bare silicon, showing ~30% of light is reflected. (b) Schematic of light illuminates on textured silicon, showing light trapping. (c) Schematic of a planar *p*-*n* junction solar cell architecture, indicating the thickness of the absorber, *L*, and the minority carrier diffusion length in this case, L_n, must be larger than the penetration depth of the photons, $1/\alpha$. (d) Schematic of the parallel multi-(*p*-*n*)-junction solar cell architecture. *L* is still required to be larger than $1/\alpha$, but L_n can be tolerated. After references[7,10,11].

So far, the PV technologies can be assorted into three generations. *First generation* solar cells are based on crystalline silicon (*c*-Si), which dominates the marketplace currently and holds a champion record of conversion efficiency (~22.3%) in single junction solar cells. Unfortunately, due to its relatively low absorption coefficient, the *c*-Si solar cells require hundreds of micrometers thick layer to absorb all the incident photon. Moreover, high purity silicon is also demanded to decrease the recombination rate, which further add up to the cost of the final device. The high cost of manufacturing and installation of c-Si solar cells prevent the widespread use of first generation solar cells.

Thin film solar cells (TFSCs) are generally considered as *second generation* solar cells, which include amorphous silicon (a-Si) and other chalcogenide-based polycrystalline thin films of cadmium telluride (CdTe), copper indium diselenide (CIS) and copper indium gallium diselenide (CIGS)[12-14]. Controversially, epilayer of indium gallium phosphide (InGaP) and gallium arsenide (GaAs) are also regarded as second generation solar cells. Owning to the availability in large scale production and less expensive raw materials, TFSC significantly bring down the cost. More importantly, TFSCs hold a shorter payback period (1 year) as compared to the c-Si solar cells. These advantages, together with the flexibility, low space usage, and light weight greatly extend the application of second generation solar cells. Despite the low cost of raw materials and manufacturing processes, TFSCs have some inherent drawbacks. Except from multiple junction solar cells based on InGaP and GaAs, most of the TFSCs exhibit relatively low energy conversion efficiency in the range of 10~18%[15,16]. Additionally, the stability of TFSC is another concern because some of the materials degenerate over time when exposed to sunlight[17,18]. Nonetheless, second generation solar cells have been gaining market share since 2008.

Third generation solar cells mostly involve cutting edge technology, aiming to deliver high efficiency at an economically viable cost[9,19,20]. Alternatively, third generation solar cells can be roughly defined as the solar technologies attempt to overcome the Schockley-Queisser efficiency limit. In this regard, a wide range of potential solar innovations, such as organic photovoltaic cells (OPV), dye-sensitized solar cells (DSSCs), quantum dots sensitized solar cells (QDSSC), intermediate band cells, and other nanostructured solar cells can be considered as third generation solar cells.

1.3 Nanomaterials in solar cells

As the physical dimensions of the materials reduce to nanometer scales, quantization and surface effect begin to dominate the physical properties and drastic changes are expected to be observed in terms of light-mater interaction, charge carriers generation and transport dynamics. In this regard, the advent of nanomaterials opens the avenue to develop next generation solar cells that can deliver high efficiency at a relatively low cost. According to the confined dimensionality, nanomaterials can be classified as zero dimensional (0D), one dimensional (1D), and two dimensional (2D) nanomaterials, and all of them could be employed to increase the efficiency of solar cells. In this section, the benefit that can be taken from 0D and 2D nanomaterials are discussed. The application of 1D nanomaterials, focusing on nanowires, in solar energy harvesting will be reviewed in section 1.4.

1.3.1 Quantum Dots in solar cells

Quantum dots, also known as semiconductor nanocrystals, are the crystals having sizes similar to or less than that of the Bohr radius of an exciton in the corresponding bulk materials. As a consequence of quantum confinement, several unique optical and electrical properties arise that can substantially contribute to the light harvesting in solar cells.

Size dependant bandgap

The amazing property of quantum dots in light absorption is size-dependant band gap. Due to the quantum confinement, the energy levels in a quantum dots are discrete and the band gap of a quantum dot as shown in Figure1.4, and can be mathematically described as:

$$E_g(QD) = E_g(bulk) + \frac{h^2}{2m^* d^2} - \frac{1.8e^2}{2\pi\varepsilon\varepsilon_0} \quad (1)$$

$$\frac{1}{m^*} = \frac{1}{m_e} + \frac{1}{m_h} \quad (2)$$

Here, E_g (QD) is the energy band gap of a nanocrystal quantum dot, Eg (bulk) is the energy band gap of a bulk semiconductor, h is the Planck constant, m^* is the reduced mass of exciton, m_e is the effective mass of an electron, m_h is the effective mass of a hole, d is the diameter of a

nanocrystal, *e* is the electron charge, ε is the relative dielectric constant, and ε_0 is the space dielectric constant. As shown in Equations, the bandgap of QD is highly dependent on its diameter. In detail, when the size decreases, the lowest conduction band level and highest valence band level significantly change with the diameter of the quantum dots, resulting in a blue shift of the band gap. This tunability of band gap makes quantum dots fascinating for light absorption and inspired a number of groups to fabricate QDSSCs[21-23]. In principle, narrow bandgap QDs are coupled with wide bandgap semiconductor nanostructures, such as TiO_2, ZnO and SnO_2, in QDSSCs; and upon light illumination, electrons are injected into wide band gap semiconductor while the holes are transported by the electrolyte. The whole process is similar to that occurred in DSSCs, except the absorbers are replaced by QDs. An optimized configuration of QDSSC, termed as rainbow solar cell, has been demonstrated by anchoring CdSe QDs with different sizes on TiO_2 nanotubes array, in an attempt to effectively couple the faster electron injection rate of small dots and greater absorption range of large dots[24].

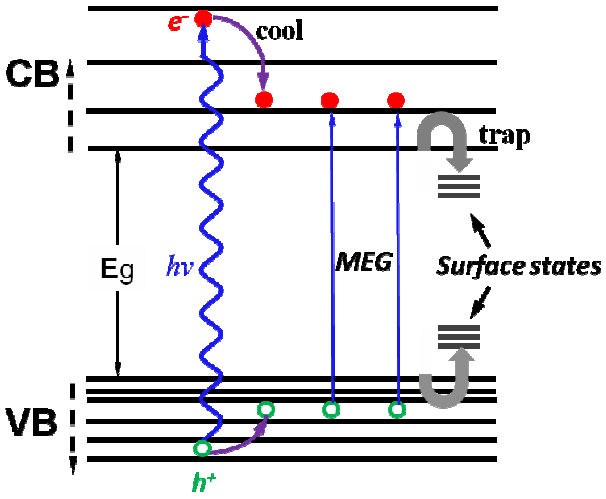

Figure1.4. Schematic drawing of discrete energy levels and possible carrier dynamical processes upon illumination in quantum dots. The trend of increasing bandgap with decreasing nanocrystal size *is* denoted by the dashed line. The processes of a photon with $hv > 3Eg$ generates three electron-hole pairs is also depicted, as well as the surface states.

Multiple exciton generation (MEG)

Generally, one incoming photon with energy in excess of the bandgap, $hv > Eg$, absorbed by semiconductor produces an electron-hole pair (EHP) and the excess energy, $\Delta = hv - Eg$, will be transferred into the kinetic energy of the EHP. The charge carrier then has an effective temperature much higher than that of the crystal lattice; and therefore, the carrier is referred to as *hot carrier*. In practical bulk solar cells, the hot carrier is rapidly cooled to the band edge, and the excess energy is depleted in the form of lattice vibrations, i.e., phonons, resulting in the theoretical limit. One may imagine that the photocurrent in solar cells can be significantly enhanced if the hot carrier can generate one or more EHP, which is, in fact, multiple exciton generation[25,26]. In order to gain the excess energy, a straightforward approach is to slow down the cooling process of the hot carries. However, owing to the rapid thermalization process (less than 0.5 picoseconds), it is rarely observed in bulk semiconductors. In a quantum dot, the carriers are confined in all three dimensions and the conduction band and the valence band separate into a set of discrete energy levels. If the spacing between energy levels is larger than the optical phonon energy, the relaxation rate of hot carrier will be slower than the recombination rate, leading to so-called "phonon bottleneck" effects[9]. In this case, the hot electron must have the energy of at least two times the bandgap to create one additional EHP. Figure 1.4 shows the presumable dynamical process in a quantum dot that absorbs a photon and generates three electron-hole pairs. Nonetheless, up to now, there is no practical PV device that has been able to demonstrate the harvesting of MEG and, in fact, there has been considerable debate about the artifacts and reproducibility in the measurement and interpretation[27].

Surface effects

Because of the high aspect ratio, the surface states of QDs play an important role in determining the charge transport dynamics. It is well accepted that the presence of the surface states is detrimental to the charge collection because the photogenerated carrier can be trapped in these states, as depicted in Figure1.4. However, some research suggested that the surface states presumably contribute to the prolonged lifetime of hot carrier due to the physical separation of electron and hole. The high surface-to-volume ratio of quantum dots facilitates the anchoring of absorber molecules. For instance, despite numerous works on replacing nanoparticles with

nanowires and nanotubes, the highest energy conversion efficiency of DSSC is still based on TiO_2 nanoparticles.

Other potential advantages of employing quantum dots in solar cells rely on the synthesis techniques and related possible cost reductions. For some quaternary solar cell materials, the stoichiometry of the elements is crucial to determining the bandgap and electrical properties, which in turn limit the device performance[28,29]. However, nonstoichiometric materials are often obtained by tradition processing methods[30,31]. New approaches developed to synthesize quantum dots provide the possibility to accurately control the stoichiometry at nanometer scale[32-34]. In addition, small size quantum dots can be stabilized in solution and adapted to ink-inject technique, suggesting the feasibility to fabricate low cost thin film solar cells by greatly reducing the raw material wastage[35-37].

1.3.2 2D nanomaterials in solar cells

Graphene, the thinnest 2D nanomaterial, holds great promise for its potential application in PV because of the unique properties, such as the excellent conductance, good transparency in both the visible and near infrared regions, ultra-smooth surface with tunable wettability, high chemical and mechanical stabilities, and low cost in fabrications[38]. So far, graphene has been adapted in silicon solar cells, organic solar cells, DSSCs and QDSSCs as transparent electrode, counter electrode, and carrier transport.

Today, the major transparent electrodes used in PV industry are indium tin oxides (ITO) and fluorine doped tin oxide (FTO). Despite the satisfying transparency and good conductance, ITO still have some inherent disadvantages, such as not abundant in earth's crust, possible ion diffusion, poor transparency in the near infrared region, and brittleness[39]. These disadvantages limit ITO as an ideal transparent conductive layer in the next generation solar cells. Many efforts have been dedicated to seek alternative transparent conductive materials[40-43], and the advent of graphene offers the prospect because it exhibits transparency in both visible and near infrared region by atomic layer thickness, good flexibility and easy accessibility. To make a graphene based transparent electrode, graphene oxide (GO) solution is generally spin-coated on quartz substrate and then reduced chemically followed by high temperature annealing[44]. Despite

the low cost and flexibility, the graphene derived from GO has a high density of defects that limit the application in transparent electrodes. An Alternative strategy is to directly grow a large area graphene on nickel coated copper foil or thermal oxidation on silicon substrate by CVD technique, and transfer graphene to a glass substrate by the well-known etch-peel process[45]. In contrast to the reduced graphene thin film, CVD grown graphene exhibits a lower sheet resistance but still higher than that of ITO. So far, apart from the superior chemical and mechanical stability, solar cells using graphene as a transparent electrode show an inferior efficiency than that of taking ITO as the transparent electrode, which awaits further modification or improvement of the transmittance and conductance.

Owning to its high mobility at room temperature, graphene plays an important role in carrier transport and therefore can enhance the conversion efficiency by suppressing the competing recombination. A CdS QDs /graphene layered structure was reported with a high PCE value of 16%, while the same hybrid structure consisting of multiwall carbon nanotubes exhibited a PCE value of 9%. The carrier transport effect of graphene is more important in OPV, because the existence of problems associated with the phase separation process, such as the isolated domains and structural traps, which is inevitable in making the heterojunction.

Very recently, a new family of 2D nanomaterials, widely known as layered transition-metal dichalcogenides (LTMDs), has been intensively investigated[46,47]. Similar to graphene, MoS_2, can be fabricated by exfoliation[48] and CVD, exhibiting unique electrical and optical properties. Although the transmittance and sheet resistance are far from ITO, further improvement in sheet sizes and suppressed formation of semiconducting phase could potentially extend their performance[48].

1.4 Nanowire solar cells

1.4.1 Individual nanowire solar cells

In the past decades, much attention has been attracted on the tiny solar cells processed from individual nanowires, i.e., single nanowire solar cells, because of a series of unique properties induced by the reduced dimensionality. First, these portable solar cells, upon light illumination, can serve as robust power source to drive nanodevices working at lower energy consumption and

can be easily incorporated into the existing microelectromechanical systems (MEMS) or future nanoelectromechanical systems (NEMS). Second, as compared to conventional solar cells, individual nanowire solar cells hold great potential to achieve higher energy-conversion, owing to its mostly single crystalline nature, strain relaxation effects, and tunablity of bandgap when size goes down to nanoscale. More importantly, the solar cells based on individual nanowires offer an ideal platform to probe the photovoltaic effects, i.e., light absorption, charge separation, and collection, in reduced dimensionality and thus facilitate the fundamental understanding of light-matter interaction and carries dynamics, in pursuit of efficient ways in designing macroscopic solar cells comprised of nanowire array or improving the efficiency of conventional planar solar cells. In principle, single nanowire solar cells are processed by bottom-up approaches, which enable us to investigate different parameters, such as doping level, contacts, junctions, and etc.

In this section, the light absorption enhancement in an individual nanowire will be first reviewed, along with the dependence of charge dynamics, including surface recombination and bulk recombination, on the size and morphologies of the nanowire. The current research status of single nanowire solar cells, categorized by material junctions will be discussed. Finally, the survey for the current efficiency of single nanowire solar cells will also be presented.

1.4.1.1 Light absorption in a single nanowire

When a single nanowire lying flat on a substrate is illuminated by photons, considerable amount of energy will be transmitted, owing to the insufficient thickness or light trapping to quench all the photons. However, the nanowire itself possesses the ability to collect and trap the light into a sub-wavelength volume; this energy loss in terms of light absorption can be minimized or compensated for by the resonant effect and optical cross-section effect induced by the nanowire morphology. The resonant optical mode was originally predicted in the case of spherical particle and then developed for micrometer-scale resonators. Cao *et al*. use the framework of leaky mode resonances (LMR) to probe the resonant field enhancement in nanoscale structures. Nanowire in these studies was considered as a sub-wavelength resonator in which light can be trapped in circulating orbits by multiple total internal reflections from the boundaries[49]. Given an infinitely long cylinder and by solving Maxwell's equations with

boundary condition, the excitation of the leaky modes can be obtained as a function of the dielectric constant and wire diameters. Taking germanium nanowire as an example, they found that the light absorption in single nanowire is highly related to the size, geometry, and orientation of the nanowires. In other words, one could engineer the light absorption in a single nanowire by tuning the morphologies and geometry of the nanostructures. Moreover, LMR also holds true in coated nanowire which further enables the engineering of light absorption. For example, the photocurrents in Si/a-Si coaxial nanowire could be enhanced by a factor of 5.6 with respect to the bare silicon nanowire, and which could be further improved by introducing another non-absorption dielectric coating[50]. Additionally, the use of metal nanoparticles decoration on a single nanowire to enhance and suppress the absorption, by harnessing the excitation of surface plasmons, offers an additional degree of freedom to engineering the light absorption in a single nanowire. For instance, the photocurrent of a silicon core-shell nanowire decorated with a silver nanocrystal was observed to increase or decrease depending on the wavelength with respect to the nanocrystal's surface plasmon resonance or nanowire's optical resonance, which is in a good agreement with the finite-difference frequency-domain (FTDT) simulation[51].

In practical single nanowire solar cells, the nanowire itself is generally horizontally lying on a silicon substrate with a SiO_2 layer of considerable thickness, and the interfaces, with the high-refractive-index silicon substrate, can be viewed as a low-quality factor Fabry-Perot cavity. In this case, the whole light absorption in the nanowire is therefore further enhanced by the Fabry-Perot resonance, which is usually taken into consideration in the form of thin film. Computed by full-filed FTDT simulation, the absorption in the nanowire oscillates as a function of the SiO_2 layer thickness, concluding that the resonance was related to the substrate[52].

1.4.1.2 Carrier dynamics in a single nanowire

Single nanowire solar cells offer an ideal platform to investigate the fundamental carrier dynamics including the charge transport, surface recombination and minority carrier diffusion. In order to understand these carrier dynamics processes, it is of great importance to extract the carrier density, mobility, surface states density, effect life time and minor carrier diffusion length[53,54]. Due to their resolution limit with respect to the low dimensionality, facilities commonly used in bulk thin films, such as Hall Effect measurement and secondary ion mass spectrometry (SIMS), cannot be applied to measure these parameters in single nanowire device.

On the contrary, field effect transistor (FET), electron beam induced current (EBIC), photoconductance, and scanning photocurrent microscope (SPCM) are the popular approaches deployed to characterize the electrical properties of nanowires.

Single nanowire FET can be configured by drop casting a nanowire on an insulating substrate, and making source and drain electrodes contacts by electron beam lithography at the nanowire ends. The carrier density, mobility and resistivity of the nanowire can then be extracted. However, special concerns about the accuracy of the data arose because of the interferential factors, such as gate capacitance, surface depletion effect and inhomogeneous dopant distribution. It is also worth mentioning that there are very few papers studying the influence of these electrical parameters on the performances of the nanowire solar cells, which could be attributed to the challenging works in doping controllability. The minority carrier transport, primarily manifested by the minority carrier diffusion length (L_D), plays a key role in determining performance of solar cells. For a semiconducting nanowire, it is generally measured on a two terminal nanowire device with Schottky junctions via EBIC and SPCM techniques.

1.4.1.3 Device geometries of single nanowire solar cells

Up to now, different prototypes of single nanowire solar cells have been proposed and demonstrated, which can be classified as radial, axial, and wire-on-thin film from viewpoint of device geometry. Alternatively, these solar cells can be divided, in view of the junction comprising of different materials, such as Shockley junctions, homojunction or heterojunction, and hybrid junctions. These junctions induce a chemical potential difference, permitting the charge separation.

The solar cell is basically a diode with rectifying characteristics, and the simple way to obtain such behavior is by forming a Shockley junction using a metal with large/small work function in contact with n/p-type semiconductor. The first type of single nanowire solar cell is, therefore, called Shockley junction solar cells. In this kind of solar cells, two asymmetric contacts, including one Ohmic contact and one Shockley contact, are generally required to extract the opposite carries. An illustrative sample of a Shockley cell has been demonstrated in silicon nanowire with an Al-Si Shockley junction, showing an efficiency of around 0.46%[55]. It should be noted that the photovoltaic effect observed in the Shockley junction cells is still under debate,

because of doping contribution while making the contacts and axially inhomogeneous distribution of the defects or other surface-related states.

Undoubtedly, most of the research activities in single nanowire solar cells are focused on homojunction or heterojunction solar cells. Generally, there are two device prototypes, axial and coaxial, in these sorts of nanowire solar cells. The latter one is also referred as core-shell structures. In 2008, the first nanoscale solar cell was demonstrated on coaxial *p-i-n* silicon nanowires, showing an efficiency of 3.4%[56]. If the single nanowire solar cells are interconnected in series or in parallel, a higher power can be extracted and used to drive practical nanodevices like PH-sensor and nanowire FET. In contrast, an axial *p-i-n* junction silicon solar cell was also developed but exhibited an efficiency of 0.5%, which indicated that, with the same *p-i-n* junction, the coaxial nanowire outperformed the axial nanowire in terms of charge collection. When illuminated by photons, the coaxial prototype structure facilitates the charge generation and separation more efficiently than the axial structure, owing to the built-in field formed across the *p-i-n* junction[56]. A series of work on coaxial structures, such as GaAs and *n*-GaN/*i*-$In_xGa_{1-x}N$/*p*-GaN[57,58], have also been reported. Note that all the above-mentioned nanowires are homojunctions, where the lattice mismatch is negligible if both the core and shell are well crystallized. However, it would be a great difference in the case of heterojunctions, where the interfacial properties should be taken into account. A CuO/C_{60} core-shell PV device presented efficiency as low as less than 0.02%, suggesting that crystallinity of the shell should be improved[59]. Excitingly, a single nanowire solar cell processed from CdS/Cu_2S core-shell nanowire demonstrated a remarkable efficiency of ~5.4%, which rivals the equivalent planar cells[60]. The superior preference can be attributed to the excellent lattice matching between the core and the shell, which greatly reduced the interfacial recombination, and the device fabrication technique benefited from the novel materials synthesis approach.

The third device geometry, to my knowledge, nanowire-thin film homojunction or heterojunction solar cells, is barely mentioned in review literatures, offering a new way to develop single nanowire solar cells. Bie *et.al* transferred an n-type ZnO nanowire to a p-type GaN thin film to fabricate a UV-photovoltaic device[61], demonstrating a high short-circuit current density of ~4250 mA/cm^2 under a 355 laser illumination with a power density of $100\mu W\mu m^{-2}$. However, it may not be suitable to calculate the final efficiency using the junction area, because of the large-area thin film compared to nanowire.

The last type of single nanowire solar cells, hybrid single solar cells, defined as the solar cells comprising of both organic and inorganic semiconductors as the active materials, are scarcely studied. However, the macroscopic hybrid solar cells comprising of nanowire array have been dedicated vast efforts, despite the lower/comparable power conversion efficiency in comparison with the organic bilayered/ bulk solar cells. The purpose of this research is mainly centered around the insightful understanding of the organic/inorganic interface, in attempt to enhance the efficiency of macroscopic hybrid solar cells. Structurally, they also have two kinds of device geometries, axial and coaxial. AAO assisted electrochemical deposition have demonstrated an efficient way to fabricate inorganic nanowire with axial heterojunction. Single nanowire solar cells based on axial CdS/polypyrrole (PPY) nanowires was demonstrated in a two step electrochemical technique involving CdS nanowire deposition, molecular absorption, and polymerization[62]. Bridged across two symmetrical gold electrodes, a low efficiency of 0.016% under an illumination of 6.05mW/cm^2 was achieved, possibly because of the poor interface between the amorphous PPY and low quality CdS crystal processed via chemical route. ZnO/organic hybrid nanowire solar cells with radial heterojunction were fabricated by grafting end functionalized oligo- and polythiophene on ZnO nanowire[63]. The device fabrication involved oxygen plasma etching the polymer, electron beam lithography (EBL) and metallization of electrodes. Notably, an efficiency of 0.036% was shown in ZnO/Poly(3-hexylthiophene) core-shell single nanowire device upon a standard efficiency test condition.

Table 1.1 PV performances of current single nanowire PV devices

Materials	Efficiency (%)	V_{oc} (V)	J_{sc} (mA/cm^2)	FF (%)	Description	References
Si	3.40	0.26	23.9	0.55	Coaxial *p-i-n*	[56]
Si	0.50	0.29	3.50	0.33	Axial *p-i-n*	[56]
Si		0.12			*p-n*	[51]
Si	0.46	0.19	5.00	0.40	Schottky junction	[55]
GaN		1.00		0.56	Coaxial *p-i-n* ,*i* layer is $In_xGa_{1-x}N$	[57]
GaAs	4.50	0.25	27.4	0.25	Coaxial *p-i-n*	[58]
CdS/Cu2S	5.40	0.60		0.81	Solution processed core-shell nanowire	[60]
CdS/PPY*	0.018	0.043	6.05	0.27	Axial hybrid junction	[62]
CuO/C_{60}	0.02				Coaxial *p-n*	[59]
ZnO/PH3T	0.05	0.15	1.43	0.25	Coaxial hybrid	[63]

* The device was tested under an illumination density of 6.05mW/cm^2.

Finally, a survey of current single nanowire solar cells is presented in Table 1.1. From the table, up to now, the highest efficiency of single nanowire solar cell is 5.4%, which was measured on a coaxial nanowire with high quality interface.

1.4.2 Nanowire array solar cells

1.4.2.1 Light absorption in nanowire array

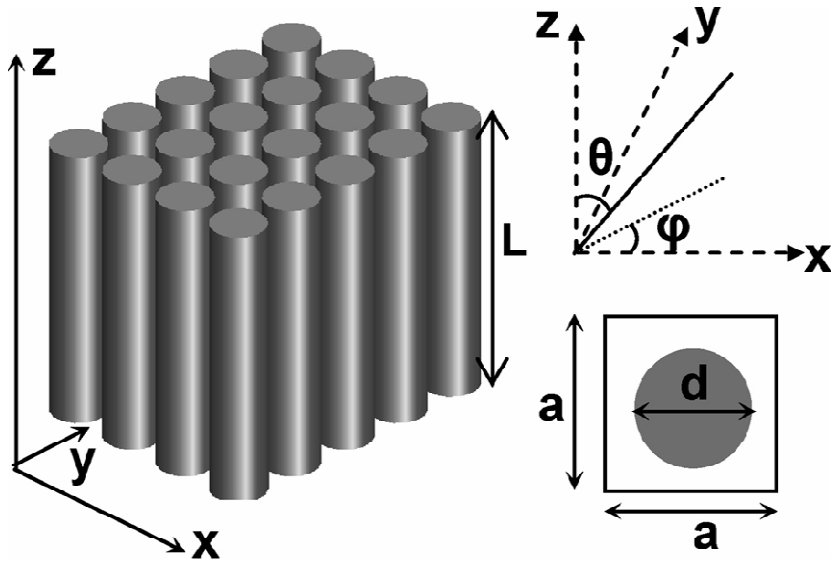

Figure 1.5. Schematics of the periodic silicon nanowire structure for simulation, where nanowire array is determined by the diameter, *d*, wire length, *L*, and the periodicity, *P*, while the direction of the incoming solar radiation is defined by the zenith, θ, and azimuthal angles, φ. Aadapted with permission from[64]. Copyright (2007) American Chemical Society.

Definitely, the resonance effects observed in single nanowire still function effectively in the nanowire array[65]. However, an array of nanowires, resembling a natural form of light harvesting structures, such as forests, give more prospects to engineer the light absorption through manipulating the reflectance and light trapping. In the past decades, enormous efforts, both theoretical and experimental, have been dedicated to understand the light-nanowire array interaction. Because of the easy accessibility of silicon nanostructure, most of the theoretical works were focused on arrays of silicon nanostructure, aiming to gain intuitive guidance in designing high-efficiency silicon solar cells. Various approaches were used to simulate the

nanowire array illuminated by sun light and the typical mode is depicted in Figure1.5, which was first proposed by Chen *et al*[64]. Using transfer matrix method, the effects of wire diameter, length, and filling ratio on the absorbtance of nanowire arrays were investigated. The simulation indicated that the nanowires, with diameter of 50~80 nm in a fixed periodicity (*P*=100nm), exhibited small reflection in a wide spectrum range, which can significantly improve the light absorption of silicon nanowire in the high-frequency regime. Owing to the small extinction coefficient of silicon, however, longer nanowires or other light trapping techniques were still required to enhance the light absorption in the low-frequency regime. The latter observation, i.e., poor light absorption in low-frequency regime, was argued by Li *et al*, who attributed it to the lower periodicity[66]. They further claimed the periodicity and the ratio of diameter/periodicity, (*d/P*), need to be taken into account in evaluating the light absorption. Furthermore, a periodicity of 250~1200nm of silicon nanowire array was projected to obtain comparable light absorption with the silicon thin film with the same thickness, while the optimal *d/P* to maximize light absorption is predicted as 0.8. Furthermore, simulation works were conducted on silicon nanohole array and nanopillar array. In particular, in contrast to nanorod array, silicon nanohole array presented a better absorption over the entire range of the investigated filling fraction, which can be ascribed to the effective light coupling and the large density of waveguide modes[67].

In addition to bare silicon nanowire array, the light absorption property of silicon core-shell nanowire arrays was also theoretically calculated. For a radial *p-n* junction silicon nanowire array, rigorous coupled wave analysis indicated that one can gain near unity absorption by a square array of 20μm long wire with radii of 200 nm and a filling fraction of 30%[68]. Using the same approach, Shen *et al* studied the light absorption of the *c*-Si/*a*-Si:H core-shell nanowire arrays and predicted substantial enhancement in photocurrent by factors of 14% and 345% per volume materials, in comparison to *c*-Si NW arrays and *a*-Si films, respectively[69].

The strong geometrical dependence of the light absorption in arrays of semiconductor nanowires has been intensively demonstrated by numerous experiments[70-73]. Normally, given other geometrical parameters are fixed, longer nanowires can absorb more photons, because of the sufficient optical path length and possibility of induced multiple scattering. On the other hand, increasing the length of nanowire will increase the chances of surface recombination. Studies have proven that there was a competition between the light absorption enhancement and surface recombination, offering the instructive principle in fabrication of nanowire array solar cells[74].

Many investigations have shown that the diameter of nanowire array is crucial for tuning its transmittance and reflectance. A dual diameter germanium nanowire array showed a striking absorbance near unity in a wavelength range of 300~900 nm. In this structure, the small diameter tips were designed to minimize the reflectance and the large diameter base can facilitate the maximal light absorption, further demonstrating the significance of diameters in tuning the absorption of the nanowire array[75]. Very recently, InAs nanowire array has been synthesized by chemical beam epitaxy and the absorption of the nanowire was found highly dependent on the morphology of the InAs nanowire. The product of the length and fill ratio (*Lf*), was revealed as a critical factor in tuning the absorption. All the observations are consistent with the theoretical simulations in the same paper[76].

Compared to uniform diameter nanowires/nanorods array, tapered nanostructure arrays usually show a superior absorption[70,77-80], which can be explained by the graded refractive index (GRI) effects[81,82]. In this regard, the nanowire array, acting as a buffer layer, intervene the difference in refractive indexes between air and the substrates.

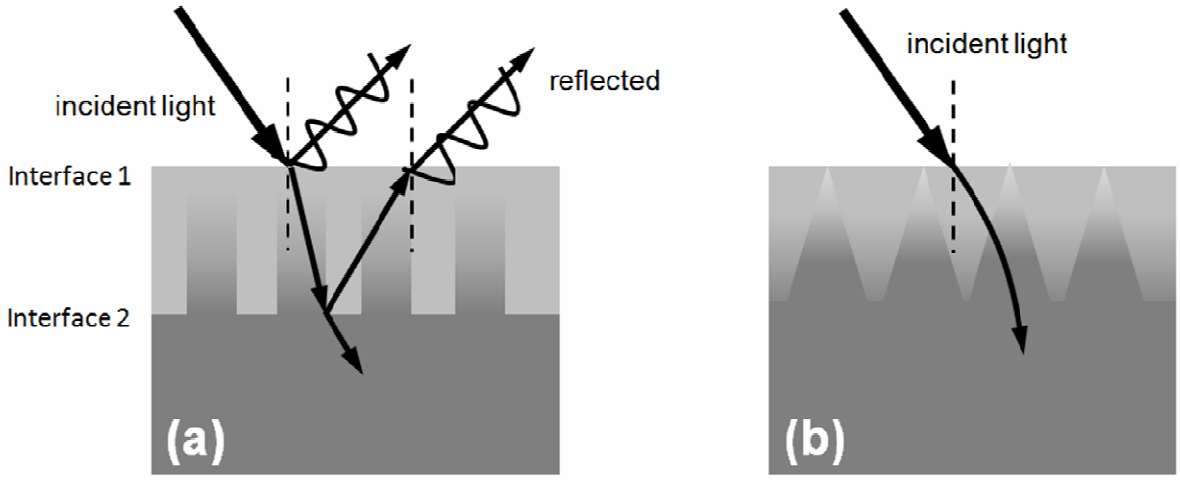

Figure 1.6. Schematics of the reflections of a substrate with (a) a homogeneous and (b) a graded-refractive-index (GRI) coating. After Ref[82]. The uniform nanowire array and conical nanowire array can be considered as homogeneous and GRI coating, respectively.

In the case of uniform diameters nanowire array, the nanowire array act only as one intermediate index layer and the reflection is partly suppressed due to interference of light reflected at the air/coating layer and at the coating layer/substrate interfaces (Figure 1.6 (a)). This large impendence mismatch effective refractive indexes between air and substrate can be

significantly compensated when a conical (i.e., tapered) structure is involved, leading to a remarkable reduction in reflectance, as shown in Figure 1.6 (b). In other words, the light absorption is greatly enhanced. Interestingly, a very recent light absorption study on InP nanowire array revealed that conical nanowire array present a higher absolute light absorption but demand a larger volume fraction of materials[83]. Thus, an intermediate geometry, i.e., cylindrical at the top and conical at the base, was proposed to balance the material cost and light absorption.

In order to standardize the fill ratio and verify the simulations, nanowires arrays are generally synthesized in periodic arrangements assisted by *e*-beam lithography. However, it was believed that the periodic structure would show anisotropic angular absorption profile, resulting in some so-called dead spots in the solar cells[84]. In fact, the randomly assembled nanowire array also exhibit noticeably increased light absorption, which has brought up the debate about the necessity of periodic nanostructure in light trapping[85,86]. To verify this, Battaglia *et al* compared the efficiencies of two *a*-Si:H solar cells processed on periodic nanocavity and random pyramidal texture substrates, finally clarifying that periodic structures rival random textures[87].

To further enhance the light absorption in nanowire array, transitional approaches that are used in silicon or thin film solar cells can also be implemented. A layer of SiN_x or Al_2O_3, acting as antireflective coating, was deposited on a silicon wire array, demonstrating a remarkable improvement in light absorption with respect to the bare wire array[84]. In addition, similar to that in single nanowire, the light absorption of nanowire array can also be efficiently enhanced by introducing plasmonic structure.

1.4.2.2 Carrier collection in nanowire array

The morphologies of nanowire array offer at least two advantages in carrier collection. On one hand, because of its single-crystalline nature in most of the cases, it plays as an ideal carrier channels that directly connects to the electrodes. In a typical DSSCs or QDSSCs, the photoanodes are consisting of wide-bandgap semiconducting nanoparticles and the carrier transport in the nanoparticles obeys the trap limited diffusion mechanism, resulting in a slow transport velocity and a high chance of recombination[88-90]. By replacing the nanoparticles with ZnO nanowire array in a DSSC, the carrier collection efficiency was found to increase by ~100 times due to the band conduction transport[91]. The lateral sizes of nanowire generally fall below

the carrier diffusion length, which facilitate the carrier collection by reducing the non-radiative recombination and carrier scattering loss[92,93], through elimination of the unnecessary lateral transport and the resulting recombination loss. Nevertheless, the striking benefit of this characteristic is associated with the device configurations, which is circumstantiated in the next section.

1.4.2.3 Possible cost reduction

In addition to the superiority in light absorption and charge collection, nanowire array also holds huge promise in reducing cost of production. First of all, because of the enhanced properties, fewer materials are needed to gain the comparable properties[65,94]. For instance, just from the point view of light absorption, it was predicted that wire array with antireflective coating can enable an increase of the efficiency by a factor of 20 but only use 1% of the materials required in a traditional wafer based device[84]. Secondly, the radial carrier collection characteristics increases materials defect tolerance[94]. Moreover, new charge generation/separation phenomena only existing in low dimensionality permit the use of inexpensive materials in solar cells. Some wide bandgap materials, which used to act as window layer or charge transporter, can function as active absorbers, extending the list of available materials[95,96]. Additionally, without relying on any expensive substrates, some nanowire arrays with high crystalline quality can be directly grown on glass[97-100], stainless steel[101], fiber[102], and alumina foil at a relatively low temperature[103]. Notably, the nanowire array in some scenarios can be fully removed, and the substrates are recyclable[104]. The nanowire array can aid the cost reduction in current solar technology. As mentioned in Section 1.2, nanowire array, solely acting as antireflective layer, can compensate the light absorption loss in a thinned *c*-Si wafer[105].

1.4.2.4 Device configuration in nanowire array solar cells

In this section, we will primarily focus on the development of all-inorganic three-dimensional PV devices based on the vertically aligned nanowire array. The achievements, challenges and prospects of DSSCs, QDSSCs and other electrochemical (PEC) solar cells processed from nanowire array, which could be referred in related reviews[2,106-108], are not covered. Depending on the device configurations, subtopics will be addressed by three different

types of PV devices, (i) nanowire array integrated with the substrate, (ii) nanowire array embedded in thin film and (iii) core-shell nanowire array.

Photovoltaic Devices Based on Nanowire Array Integrated with the Substrate

Apart from the enhanced light absorption, the integration of a vertically aligned nanowire array on the heteroepitaxial-growth substrate could benefit from the single-crystal nature and aligned geometry of nanowire array, which facilitates a fast and direct conduction of the photogenerated carrier. Recently, the realization of direct heteroepitaxial growth of vertically-aligned III-V nanowire arrays, such as GaN, InP, GaAs and InAs[110-112], on silicon substrate paves the way to succeed in integrating the nanowires and the substrate for PV devices fabrication. Tang *et al.* have fabricated *p-n* heterojunction PV cells by integrating an array of vertically aligned Mg-doped GaN nanorods on *n*-type Si substrate[113]. Single-crystalline GaN nanorod array was found to act effectively as an antireflection coating to reduce the reflection in visible spectral region and a window layer to enhance spectral response at the short-wavelength region. The device exhibited well-defined rectifying behavior in the dark with low reverse leakage current and presented a high open-circuit voltage (V*oc*) of □0.95Vand a short-circuit current density (*Jsc*) of □7.6 mA/cm^2. The fill factor (FF) and the conversion efficiency (η) were calculated to be □0.38 and □2.73%, respectively, under AM 1.5G condition. The conversion efficiency is expected to be further improved by optimizing the electrode thickness because only half of the light would transmit the top electrodes.

P-n heterojunction PV devices processed from vertically *p*-type InAs nanowire array grown heteroepitaxially on *n*-type silicon substrate was also demonstrated, showing a broad spectral response from the visible to the infrared region. The energy conversion efficiency of the typical device was achieved as 2.5% at 110K, and the open circuit voltage showed temperature-dependent characteristic[114]. In addition, direct integration of *p*-type GaAs nanowire array on *n*-type GaAs substrate as PV device was also reported[115]. The device performance was highly dependent on the morphology and doping profile of the nanowire array, which were influenced by the molecular beam epitaxy (MBE) growth temperature. The maximum conversion efficiency was determined as 1.65%, and it was anticipated to be further enhanced by manipulating the beryllium (Be) doping level.

In general, integration of the III-V semiconductor nanowire array with the Si substrate, forming semiconducting heterojunctions, can absorb a different wavelength of the solar spectrum[116]. Significantly, one distinguished feature of this device configuration is that it can easily be incorporated into the existing MEMS based on the well-developed silicon technology without complicated procedures. However, before being collected by the electrodes, the photo-excited carrier still travels a long distance. In other words, the recombination in this device configuration cannot be substantially suppressed, similar to the planar junction solar cells.

Photovoltaic devices based on nanowire array embedded in thin film

Nanowire arrays embedded in a thin film of the material having a matching energy band give rise to an architecture where light absorption and charge carrier separation can be achieved in an orthogonal direction. P. D. Yang's group developed an all-oxide solar cell composed of a vertically aligned *n*-type ZnO nanowire array covered by *p*-type Cu_2O nanoparticles, aiming at low-cost, environmentally benign, and stable PV devices[117]. The device performance was found highly dependent on the thickness, morphology and phase of the nanoparticles, which was originally determined by the process condition. The charge transport through the Cu_2O film could be improved by increasing the grain size in the film. More significantly, it was observed that introducing an immediate insulating layer (i.e. blocking layer) between the absorber and the electrodes directly contacted with the nanowires could greatly improve the overall conversion efficiency. With the atomic layer deposition (ALD) of ~10 nm TiO_2 between Cu_2O and transparent electrode, the device showed an efficiency of 0.053%, which is 50 times higher than that of the device without the blocking layer. In general, filling the nanowire array by absorbing material to contract the nanowire based PV device will result in a shunt pathway. The device performance, therefore, will be degraded, especially in the case that the absorber possesses a relatively low resistivity. These observations offer a crucial hint for designing and optimizing the configurations of PV device processed from nanowires directly assembled on the electrode.

Single crystalline compound semiconductor nanowire arrays have the potential in fabrication of next generation PV devices, but the requirement of the epitaxial match with substrate is not cost effective when it comes to practical solar modules. Nonetheless, non-epitaxial catalytic growth of randomly oriented nanowires by the vapor-liquid-solid (*VLS*) method limits the realization of the novel 3D device structures and the consequent improved

performances. Template assisted *VLS* growth of highly ordered single crystalline compound semiconductor nanowires have been proven to be an efficient way to overcome the above mentioned limitations[118]. Specifically, an efficiency of ~ 6% is obtained under AM1.5G illumination. To date, this efficiency value is higher than the previously reported values of the devices fabricated to utilize the same concepts of orthogonal architecture for light absorption and charge carrier separation. Moreover, this efficiency value can, in principle, be further improved by optimizing several synthetic and device fabrication processes. This can be achieved by increasing the transparency of the top electrode, decreasing the inter-pillar spacing of the CdS nanopillar array, coating with antireflection layer and reducing the parasitic resistances of the contacts. Additionally, the stable PV devices can be achieved by embedding the semiconductor nanopillar array in a layer of polydimethylsiloxane (PDMS).

In nanowire array embedded in thin film structures, the film quality affects the cell efficiency severely and a proper adjustment of conductivity and thickness is rather crucial to achieve novel PV devices. The parasitic resistances generated by contact electrodes and the increased reflectivity due to contact material may limit the efficiency. Further optimization of these factors remains a challenge. However, a PV device based on nanowire array embedded in a thin film has the potency for future practical solar cell modules.

Photovoltaic Devices Based on Nanowire Array with Core-Shell Structure

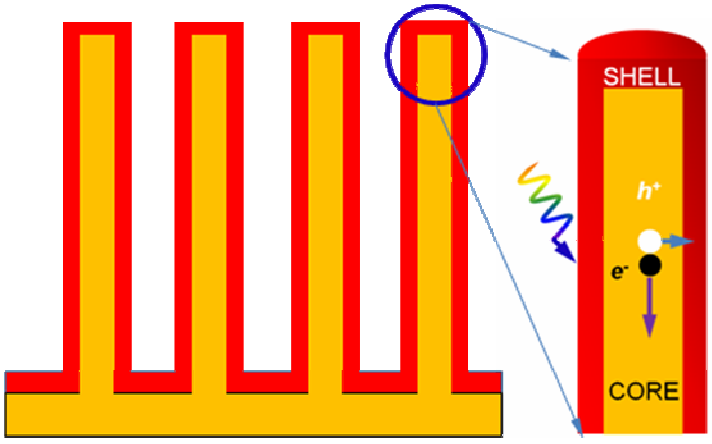

Figure 1.7 Schematic of the radial *p-n* junction, nanowire array solar cell design, which combines two advantages of enhanced light absorption by multiple scattering and improved carrier collection by suppressing the non-radiative recombination. After reference[11].

Unlike the abovementioned device configurations, a device composed of core-shell nanowire array is believed to be an optimal nanowire solar structure, by taking full advantage of morphologies in terms of light absorption and radial charge collection. Apart from reducing the stringent requirement for material purity, this unique structure enables the use of less amount of material while maintaining the same/comparable power extraction. Figure 1.7 shows the schematics of a core-shell nanowire array with *n*-type core and *p*-type shell.

Single crystalline silicon nanowire array have emerged as a promising candidate for solar PV applications[110,111,119,120]. The physical model of the device using a vertically aligned Si nanowire array with core-shell structure for *p-n* junction solar cells was first developed in 2005, and the corresponding simulated conversion efficiency was 14.5%[94]. The first Si nanowire array PV device with core-shell structure was demonstrated on stainless steel foil, exhibiting a low efficiency of ~0.1%[120]. The *p-n* junctions incorporated in the array were formed by depositing a thin amorphous *n*-type silicon layer on the quasi-aligned *p*-type silicon nanowire array. The factors affecting the performance, for instance, the impurities and junction qualities, were discussed, which should be taken into account for improving the performance of *p-n* junction nanowire array PV devices. Garnett and Yang reported a low-temperature wafer-scale etching and thin film deposition method for fabricating silicon *n-p* core-shell nanowire array PV device[121]. The core-shell Si array was obtained by a two-step procedure. Large area n-type Silicon nanowire array was first obtained by chemically etching the Si substrate, followed by chemical vapor deposition of a *p*-type Si layer. The devices were fabricated after annealing the core-shell nanowire array at an elevated temperature. The typical cell had a *Voc* of 0.29V, a *Jsc* of 4.28 mA/cm^2, and a *FF* of 0.33 for an overall efficiency of 0.46%. The reasons for the relatively low efficiency lie in severe interfacial recombination and the higher series resistance, which can be overcome by surface passivation and conductance improvement.

As compared to silicon, III-V semiconductors in solar applications have more advantages including broader spectral response, higher absorption coefficient, and higher irradiation impedance, which, therefore, could offer more possibilities to achieve higher energy conversion efficiency PV devices. GaAs, with a bandgap of 1.45eV, is the III-V semiconductor whose absorption is best matched with the solar spectrum. J. Czaban *et al*. reported the synthesis of core-shell GaAs nanowire arrays, and the influence of the doping process on the operating characteristic of the devices[122]. Vertically aligned GaAs nanowires were grown on GaAs(111)B

substrates by the VLS method in a gas source molecular beam epitaxy (MBE) system. Te and Be were used for *n* and p doping, respectively. Te doping was found to promote radial growth at the expense of axial growth. Cell parameters of the GaAs nanowire device exhibited an I*sc* of 201 μA, a V*oc* of 0.2V, and a fill factor of 0.27. The conversion efficiency of the device was measured as 0.83% and it degraded with increasing the duration of the Te-doping processes, suggesting that the morphologies and dopants distribution impact significantly on the device performances. In addition to the GaAs core-shell nanowire array, a periodic arrangement of InP core-shell nanowire array was also investigated as a *p-n* homojunction solar cell[123]. The arrangement of the dense nanowire, i.e. the directions and locations, was controlled by a catalyst-free selective-area metalorganic vapor-phase epitaxy method, while Zn and Si were chosen as the dopant to form *p* type core and *n* type shell. The nanowires are mainly perpendicular to the *p*-type InP (111) A substrate and the average internal diameter of the nanowire was 135nm and thickness of the shell was 74 nm. The device exhibited open circuit voltage, short circuit current and fill factor levels of 0.43 V,13.72 mA/cm^2 and 0.57, respectively, under AM 1.5G illumination. The solar power conversion efficiency was calculated as 3.37%, which is higher than that of Si core-shell nanowire array possibly because of the uniformity of the array, absence of the impurities (catalysts), as well as the differences in the optical absorption coefficient and bandgap between InP and Si.

Table 1.2 PV performances of current nanowire array PV devices

Classification	Efficiency (%)	V_{oc} (V)	J_{sc} (mA/cm^2)	FF (%)	Description	References
Si	0.10	0.13	1.67	0.28	quasi-aligned core-shell nanowire array on metal foil	[121]
Si	0.46	0.29	4.28	0.33	core-shell nanowire array	[122]
GaAs	1.65	0.25	27.4	0.25	directly integrated with the GaAs substrate	[114]
GaAs	0.83	0.20	0.20	0.27	core-shell nanowire array	[123]
InP	3.37	0.43	13.7	0.57	core-shell nanowire array	[124]
GaN/Si	2.73	0.95	7.60	0.38	GaN nanowire array integrated with Si substrate	[113]
CdS/CdTe	0.60	0.62	21.0	0.43	CdS nanowire embedded in CdTe thin film	[119]
ZnO/Cu_2O	0.05	0.15	1.43	0.25	ZnO nanowire embedded in Cu_2O thin film	[117]

Table 1.2 summarizes the device performances of current nanowire array PV devices measured under AM 1.5G condition. Despite tremendous works dedicated to this field, nanowire array PV devices have, to date, exhibited poor performance mostly due to the severe

surface and interface recombination arising from the large aspect ratio of nanowire array. Moreover, poor controllability of morphologies, inefficient device prototype for carrier collection and challenging manipulation in the electrical properties further deteriorate the expected conversion efficiency improvement. Additionally, the potential quantum effect, especially the size quantization property, in this system was not fully exploited because, currently, the diameters of the nanowires are far bigger than their corresponding Bohr radii.

1.5 Motivation and overview of this dissertation

According to the above review, nanowires hold a great potential to facilitate the deep fundamental understanding of photon-electricity conversion process in nanoscale, to improve the energy conversion efficiency by enhancing the light absorption and carrier collection, and to significantly reduce the cost through expanding the materials choices and relaxing the stringent criterion for material quality. In particular, nanowire with core-shell geometry stands out of all the device configurations, largely because of the radial carrier collection characteristic. However, current studies about core-shell nanowire in solar cells are mostly focused on the *p-n*/*p-i-n* homojunction constructed by narrow bandgap semiconductors, and most nanowire solar cells exhibited an inferior efficiency to their planar counterparts owning to the notorious surface/interface recombination. There have been theoretical calculations which predicted that large bandgap semiconductors could be actively involved in light absorption and charge separation in a form of coaxial nanowire with type-II band alignment[95,96]. On the other hand, the influence of interfacial quality on the properties in core-shell nanowire solar cells has not been much studied to date[60].

In view of these circumstances, this dissertation will be dedicated to address two issues: i) experimentally demonstrate new charge separation and absorption profile concept in a type-II heterojunction consisting of two wide bandgap semiconductors, and ii) probe the influence of interfacial properties on the PV performance of the core-shell nanowire by selecting a lattice matching combination. Chapter 2 will present the growth of ZnO nanostructures via different approach including CVD, hydrothermal and pulsed laser deposition (PLD). The electrical and optical properties will also be discussed. The synthesis and structural analysis of two II-VI wide bandgap semiconductor combinations, ZnO/ZnSe and ZnO/ZnS core-shell nanowire array, will

be discussed in Chapter 3, together with their optical properties and photovoltaic performance. In Chapter 4, the structural analysis of ZnO/CuO core-shell nanowire array will be presented. A new method to fabricate single core-shell nanowire device will be also introduced in this chapter. The synthesis of ZnTe, CdSe, ZnTe/CdSe, CdSe/ZnTe core-shell nanowire will be presented in Chapter 5. A photovoltaic device will be demonstrated based on an individual CdSe/ZnTe core-shell nanowire. Moreover, a controllable synthesis of CdSe nanowire array on muscovite mica will also be introduced in this chapter. In the final chapter (Chapter 6), I will give brief concluding remarks of my work and future prospects of nanowire solar cells.

Reference

1 J. F. Bookout, Episodes **12**, 257 (1989)
2 P. V. Kamat, Journal of Physical Chemistry C **112**, 18737 (2008)
3 M. Al-Husseini, Geoarabia **11**, 181 (2006)
4 E. Hemmingsen, Geoforum **41**, 531 (2010)
5 A. Valero, Energy **36**, 1848 (2011)
6 S. Roedelsperger, M. Kuhn, O. Makarynskyy, and C. Gerstenecker, Pure and Applied Geophysics **165**, 1131 (2008)
7 Jenny Nelson. (Wiley-VCH Verlag GmbH & Co. KGaA, weinheim, 2005)
8 M. A. Green, Materials Science and Engineering B-Solid State Materials for Advanced Technology **74**, 118 (2000)
9 G. F. Brown and J. Q. Wu, Laser & Photonics Reviews **3**, 394 (2009)
10 S. M. Sze and Kwok K. Ng. (John Wiley & Sons, Inc, Hoboken, New Jersey, 2007), Third ed
11 Brendan Melville Kayes, California Institute of Technology, 2009.
12 M. A. Green, Journal of Materials Science-Materials in Electronics **18**, S15 (2007)
13 A. M. Hermann, Solar Energy Materials and Solar Cells **55**, 75 (1998)
14 A. V. Shah, R. Platz, and H. Keppner, Solar Energy Materials and Solar Cells **38**, 501 (1995)
15 A. Chirila, S. Buecheler, F. Pianezzi, P. Bloesch, C. Gretener, A. R. Uhl, C. Fella, L. Kranz, J. Perrenoud, S. Seyrling, R. Verma, S. Nishiwaki, Y. E. Romanyuk, G. Bilger, and A. N. Tiwari, Nature Materials **10**, 857 (2011)
16 I. Repins, M. A. Contreras, B. Egaas, C. DeHart, J. Scharf, C. L. Perkins, B. To, and R. Noufi, Progress in Photovoltaics **16**, 235 (2008)
17 S. Kawakita, M. Imaizumi, K. Kibe, T. Ohshima, H. Itoh, S. Yoda, and O. Odawara, Japanese Journal of Applied Physics Part 2-Letters & Express Letters **46**, L670 (2007)
18 S. Kijima and T. Nakada, Applied Physics Express **1**, (2008)
19 G. Conibeer, Materials Today **10**, 42 (2007)
20 M. A. Green, Progress in Photovoltaics **9**, 123 (2001)
21 S. Gimenez, I. Mora-Sero, L. Macor, N. Guijarro, T. Lana-Villarreal, R. Gomez, L. J. Diguna, Q. Shen, T. Toyoda, and J. Bisquert, Nanotechnology **20**, (2009)
22 M. Shalom, S. Ruhle, I. Hod, S. Yahav, and A. Zaban, J. Am. Chem. Soc. **131**, 9876 (2009)
23 J. H. Bang and P. V. Kamat, Acs Nano **3**, 1467 (2009)
24 A. Kongkanand, K. Tvrdy, K. Takechi, M. Kuno, and P. V. Kamat, J. Am. Chem. Soc. **130**, 4007 (2008)
25 M. C. Beard, Journal of Physical Chemistry Letters **2**, 1282 (2011)
26 A. J. Nozik, Chemical Physics Letters **457**, 3 (2008)
27 J. B. Sambur, T. Novet, and B. A. Parkinson, Science **330**, 63 (2010)
28 S. Y. Chen, J. H. Yang, X. G. Gong, A. Walsh, and S. H. Wei, Physical Review B **81**, (2010)
29 H. X. Wang, International Journal of Photoenergy (2011)
30 H. Katagiri, K. Jimbo, W. S. Maw, K. Oishi, M. Yamazaki, H. Araki, and A. Takeuchi, Thin Solid Films **517**, 2455 (2009)
31 B. A. Schubert, B. Marsen, S. Cinque, T. Unold, R. Klenk, S. Schorr, and H. W. Schock, Progress in Photovoltaics **19**, 93 (2011)
32 Q. Guo, G. M. Ford, W. C. Yang, B. C. Walker, E. A. Stach, H. W. Hillhouse, and R. Agrawal, J. Am. Chem. Soc. **132**, 17384 (2010)

33 C. Yan, C. Huang, J. Yang, F. Y. Liu, J. Liu, Y. Q. Lai, J. Li, and Y. X. Liu, Chem. Commun. **48**, 2603 (2012)
34 S. C. Riha, B. A. Parkinson, and A. L. Prieto, J. Am. Chem. Soc. **131**, 12054 (2009)
35 G. M. Ford, Q. J. Guo, R. Agrawal, and H. W. Hillhouse, Thin Solid Films **520**, 523 (2011)
36 Q. Guo, S. J. Kim, M. Kar, W. N. Shafarman, R. W. Birkmire, E. A. Stach, R. Agrawal, and H. W. Hillhouse, Nano Lett. **8**, 2982 (2008)
37 Q. J. Guo, H. W. Hillhouse, and R. Agrawal, J. Am. Chem. Soc. **131**, 11672 (2009)
38 K. S. Novoselov, A. K. Geim, S. V. Morozov, D. Jiang, Y. Zhang, S. V. Dubonos, I. V. Grigorieva, and A. A. Firsov, Science **306**, 666 (2004)
39 Y. H. Hu, H. Wang, and B. Hu, Chemsuschem **3**, 782 (2010)
40 A. R. Madaria, A. Kumar, F. N. Ishikawa, and C. W. Zhou, Nano Research **3**, 564 (2010)
41 L. Hu, D. S. Hecht, and G. Gruner, Nano Lett. **4**, 2513 (2004)
42 S. De, C. S. Boland, P. J. King, S. Sorel, M. Lotya, U. Patel, Z. L. Xiao, and J. N. Coleman, Nanotechnology **22**, (2011)
43 V. Scardaci, R. Coull, P. E. Lyons, D. Rickard, and J. N. Coleman, Small **7**, 2621 (2011)
44 X. Wang, L. J. Zhi, and K. Mullen, Nano Lett. **8**, 323 (2008)
45 X. S. Li, W. W. Cai, J. H. An, S. Kim, J. Nah, D. X. Yang, R. Piner, A. Velamakanni, I. Jung, E. Tutuc, S. K. Banerjee, L. Colombo, and R. S. Ruoff, Science **324**, 1312 (2009)
46 J. N. Coleman, M. Lotya, A. O'Neill, S. D. Bergin, P. J. King, U. Khan, K. Young, A. Gaucher, S. De, R. J. Smith, I. V. Shvets, S. K. Arora, G. Stanton, H. Y. Kim, K. Lee, G. T. Kim, G. S. Duesberg, T. Hallam, J. J. Boland, J. J. Wang, J. F. Donegan, J. C. Grunlan, G. Moriarty, A. Shmeliov, R. J. Nicholls, J. M. Perkins, E. M. Grieveson, K. Theuwissen, D. W. McComb, P. D. Nellist, and V. Nicolosi, Science **331**, 568 (2011)
47 Z. Y. Zeng, Z. Y. Yin, X. Huang, H. Li, Q. Y. He, G. Lu, F. Boey, and H. Zhang, Angewandte Chemie-International Edition **50**, 11093 (2011)
48 G. Eda, H. Yamaguchi, D. Voiry, T. Fujita, M. W. Chen, and M. Chhowalla, Nano Lett. **11**, 5111 (2011)
49 L. Y. Cao, J. S. White, J. S. Park, J. A. Schuller, B. M. Clemens, and M. L. Brongersma, Nature Materials **8**, 643 (2009)
50 W. F. Liu, J. I. Oh, and W. Z. Shen, Nanotechnology **22**, (2011)
51 S. Brittman, H. W. Gao, E. C. Garnett, and P. D. Yang, Nano Lett. **11**, 5189 (2011)
52 C. Colombo, P. Krogstrup, J. Nygard, M. L. Brongersma, and A. F. I. Morral, New Journal of Physics **13**, (2011)
53 B. Tian, T. J. Kempa, and C. M. Lieber, Chemical Society Reviews **38**, 16 (2009)
54 E. C. Garnett, M. L. Brongersma, Y. Cui, and M. D. McGehee, "Nanowire Solar Cells", in *Annual Review of Materials Research, Vol 41*, edited by D. R. Clarke and P. Fratzl (2011), Vol. 41, pp. 269.
55 M. D. Kelzenberg, D. B. Turner-Evans, B. M. Kayes, M. A. Filler, M. C. Putnam, N. S. Lewis, and H. A. Atwater, Nano Lett. **8**, 710 (2008)
56 B. Z. Tian, X. L. Zheng, T. J. Kempa, Y. Fang, N. F. Yu, G. H. Yu, J. L. Huang, and C. M. Lieber, Nature **449**, 885 (2007)
57 C. Colombo, M. Heiss, M. Gratzel, and A. F. I. Morral, Appl. Phys. Lett. **94**, (2009)
58 Y. J. Dong, B. Z. Tian, T. J. Kempa, and C. M. Lieber, Nano Lett. **9**, 2183 (2009)
59 Q. L. Bao, C. M. Li, L. Liao, H. B. Yang, W. Wang, C. Ke, Q. L. Song, H. F. Bao, T. Yu, K. P. Loh, and J. Guo, Nanotechnology **20**, (2009)
60 J. Y. Tang, Z. Y. Huo, S. Brittman, H. W. Gao, and P. D. Yang, Nat. Nanotechnol. **6**, 568 (2011)
61 Y. Q. Bie, Z. M. Liao, P. W. Wang, Y. B. Zhou, X. B. Han, Y. Ye, Q. Zhao, X. S. Wu, L. Dai, J. Xu, L. W. Sang, J. J. Deng, K. Laurent, Y. Leprince-Wang, and D. P. Yu, Advanced Materials **22**, 4284 (2010)
62 Y. B. Guo, Y. J. Zhang, H. B. Liu, S. W. Lai, Y. L. Li, Y. J. Li, W. P. Hu, S. Wang, C. M. Che, and D. B. Zhu, Journal of Physical Chemistry Letters **1**, 327 (2010)

63 A. L. Briseno, T. W. Holcombe, A. I. Boukai, E. C. Garnett, S. W. Shelton, J. J. M. Frechet, and P. D. Yang, Nano Lett. **10**, 334 (2010)
64 L. Hu and G. Chen, Nano Lett. **7**, 3249 (2007)
65 L. Y. Cao, P. Y. Fan, A. P. Vasudev, J. S. White, Z. F. Yu, W. S. Cai, J. A. Schuller, S. H. Fan, and M. L. Brongersma, Nano Lett. **10**, 439 (2010)
66 J. S. Li, H. Y. Yu, S. M. Wong, X. C. Li, G. Zhang, P. G. Q. Lo, and D. L. Kwong, Appl. Phys. Lett. **95**, (2009)
67 S. E. Han and G. Chen, Nano Lett. **10**, 1012 (2010)
68 H. Alaeian, A. C. Atre, and J. A. Dionne, Journal of Optics **14**, (2012)
69 W. Q. Xie, W. F. Liu, J. I. Oh, and W. Z. Shen, Appl. Phys. Lett. **99**, (2011)
70 Y. R. Lu and A. Lal, Nano Lett. **10**, 4651 (2010)
71 Y. L. Chueh, Z. Y. Fan, K. Takei, H. Ko, R. Kapadia, A. A. Rathore, N. Miller, K. Yu, M. Wu, E. E. Haller, and A. Javey, Nano Lett. **10**, 520 (2010)
72 Y. F. Li, J. H. Zhang, and B. Yang, Nano Today **5**, 117 (2010)
73 H. P. Wang, K. T. Tsai, K. Y. Lai, T. C. Wei, Y. L. Wang, and J. H. He, Optics Express **20**, A94 (2012)
74 E. Garnett and P. D. Yang, Nano Lett. **10**, 1082 (2010)
75 Z. Y. Fan, R. Kapadia, P. W. Leu, X. B. Zhang, Y. L. Chueh, K. Takei, K. Yu, A. Jamshidi, A. A. Rathore, D. J. Ruebusch, M. Wu, and A. Javey, Nano Lett. **10**, 3823 (2010)
76 Phillip M. Wu, Nicklas Anttu, H. Q. Xu, Lars Samuelson, and Mats-Erik Pistol, Nano Lett. **12**, 5 (2012)
77 J. Zhu, C. M. Hsu, Z. F. Yu, S. H. Fan, and Y. Cui, Nano Lett. **10**, 1979 (2010)
78 R. Yu, K. L. Ching, Q. F. Lin, S. F. Leung, D. Arcrossito, and Z. Y. Fan, Acs Nano **5**, 9291 (2011)
79 R. Y. Zhang, B. Shao, J. R. Dong, J. C. Zhang, and H. Yang, Journal of Applied Physics **110**, (2011)
80 J. Y. Jung, Z. Guo, S. W. Jee, H. D. Um, K. T. Park, and J. H. Lee, Optics Express **18**, A286 (2010)
81 Y. J. Lee, D. S. Ruby, D. W. Peters, B. B. McKenzie, and J. W. P. Hsu, Nano Lett. **8**, 1501 (2008)
82 S. L. Diedenhofen, G. Vecchi, R. E. Algra, A. Hartsuiker, O. L. Muskens, G. Immink, Epam Bakkers, W. L. Vos, and J. G. Rivas, Advanced Materials **21**, 973 (2009)
83 S. L. Diedenhofen, O. T. A. Janssen, G. Grzela, Epam Bakkers, and J. G. Rivas, ACSNano **5**, 2316 (2011)
84 M. D. Kelzenberg, S. W. Boettcher, J. A. Petykiewicz, D. B. Turner-Evans, M. C. Putnam, E. L. Warren, J. M. Spurgeon, R. M. Briggs, N. S. Lewis, and H. A. Atwater, Nature Materials **9**, 239 (2010)
85 O. L. Muskens, J. G. Rivas, R. E. Algra, Epam Bakkers, and A. Lagendijk, Nano Lett. **8**, 2638 (2008)
86 L. Tsakalakos, J. Balch, J. Fronheiser, B. A. Korevaar, O. Sulima, and J. Rand, Appl. Phys. Lett. **91**, (2007)
87 Corsin Battaglia, Ching-Mei Hsu, Karin Söderström, Jordi Escarré, Franz-Josef Haug, Mathieu Charrière, Mathieu Boccard, Matthieu Despeisse, Duncan T. L. Alexander, Marco Cantoni, Yi Cui, and Christophe Ballif, Acs Nano **6**, 2790 (2012)
88 G. P. Kalaignan and Y. S. Kang, J. Photochem. Photobiol. C-Photochem. Rev. **7**, 17 (2006)
89 E. M. Barea, M. Shalom, S. Gimenez, I. Hod, I. Mora-Sero, A. Zaban, and J. Bisquert, J. Am. Chem. Soc. **132**, 6834 (2010)
90 I. Mora-Sero, S. Gimenez, F. Fabregat-Santiago, R. Gomez, Q. Shen, T. Toyoda, and J. Bisquert, Accounts of Chemical Research **42**, 1848 (2009)
91 M. Law, L. E. Greene, J. C. Johnson, R. Saykally, and P. D. Yang, Nature Materials **4**, 455 (2005)
92 Yong Zhang, M. D. Sturge, K. Kash, B. P. van der Gaag, A. S. Gozdz, L. T. Florez, and J. P. Harbison, Phys. Rev. B **51**, 13303 (1995)
93 Y. Li, F. Qian, J. Xiang, and C. M. Lieber, Materials Today **9**, 18 (2006)

94 B. M. Kayes, H. A. Atwater, and N. S. Lewis, Journal of Applied Physics **97**, (2005)
95 J. Schrier, D. O. Demchenko, and L. W. Wang, Nano Lett. **7**, 2377 (2007)
96 Y. Zhang, L. W. Wang, and A. Mascarenhas, Nano Lett. **7**, 1264 (2007)
97 X. J. Feng, K. Shankar, O. K. Varghese, M. Paulose, T. J. Latempa, and C. A. Grimes, Nano Lett. **8**, 3781 (2008)
98 B. Liu and E. S. Aydil, J. Am. Chem. Soc. **131**, 3985 (2009)
99 M. J. Zhou, H. J. Zhu, Y. Jiao, Y. Y. Rao, S. Hark, Y. Liu, L. M. Peng, and Q. Li, Journal of Physical Chemistry C **113**, 8945 (2009)
100 V. Sivakov, G. Andra, A. Gawlik, A. Berger, J. Plentz, F. Falk, and S. H. Christiansen, Nano Lett. **9**, 1549 (2009)
101 M. H. Kim, Y. H. Park, I. Kim, T. E. Park, Y. M. Sung, and H. J. Choi, Mater. Lett. **64**, 2306 (2010)
102 J. M. Liu, W. W. Wu, S. Bai, and Y. Qin, Acs Applied Materials & Interfaces **3**, 4197 (2011)
103 L. E. Greene, M. Law, J. Goldberger, F. Kim, J. C. Johnson, Y. F. Zhang, R. J. Saykally, and P. D. Yang, Angewandte Chemie-International Edition **42**, 3031 (2003)
104 J. M. Spurgeon, S. W. Boettcher, M. D. Kelzenberg, B. S. Brunschwig, H. A. Atwater, and N. S. Lewis, Advanced Materials **22**, 3277 (2010)
105 Y. Liu, A. Das, S. Xu, Z. Y. Lin, C. Xu, Z. L. Wang, A. Rohatgi, and C. P. Wong, Adv. Energy Mater. **2**, 47 (2012)
106 B. Li, L. D. Wang, B. N. Kang, P. Wang, and Y. Qiu, Sol. Energy Mater. Sol. Cells **90**, 549 (2006)
107 M. Toivola, J. Halme, K. Miettunen, K. Aitola, and P. D. Lund, International Journal of Energy Research **33**, 1145 (2009)
108 S. Anandan, Sol. Energy Mater. Sol. Cells **91**, 843 (2007)
109 Y. B. Tang, Z. H. Chen, H. S. Song, C. S. Lee, H. T. Cong, H. M. Cheng, W. J. Zhang, I. Bello, and S. T. Lee, Nano Lett. **8**, 4191 (2008)
110 A. L. Roest, M. A. Verheijen, O. Wunnicke, S. Serafin, H. Wondergem, and Epam Bakkers, Nanotechnology **17**, S271 (2006)
111 B. Mandl, J. Stangl, T. Martensson, A. Mikkelsen, J. Eriksson, L. S. Karlsson, G. Bauer, L. Samuelson, and W. Seifert, Nano Letters **6**, 1817 (2006)
112 S. G. Ihn, J. I. Song, T. W. Kim, D. S. Leem, T. Lee, S. G. Lee, E. K. Koh, and K. Song, Nano Letters **7**, 39 (2007)
113 Y. B. Tang, Z. H. Chen, H. S. Song, C. S. Lee, H. T. Cong, H. M. Cheng, W. J. Zhang, I. Bello, and S. T. Lee, Nano Lett. **8**, 4191 (2008)
114 W. Wei, X. Y. Bao, C. Soci, Y. Ding, Z. L. Wang, and D. Wang, Nano Letters **9**, 2926 (2009)
115 G. E. Cirlin, A. D. Bouravleuv, I. P. Soshnikov, Y. B. Samsonenko, V. G. Dubrovskii, E. M. Arakcheeva, E. M. Tanklevskaya, and P. Werner, Nanoscale Research Letters **5**, 360 (2010)
116 Y. J. Hwang, A. Boukai, and P. D. Yang, Nano Letters **9**, 410 (2009)
117 B. D. Yuhas and P. D. Yang, J. Am. Chem. Soc. **131**, 3756 (2009)
118 Z. Y. Fan, H. Razavi, J. W. Do, A. Moriwaki, O. Ergen, Y. L. Chueh, P. W. Leu, J. C. Ho, T. Takahashi, L. A. Reichertz, S. Neale, K. Yu, M. Wu, J. W. Ager, and A. Javey, Nature Materials **8**, 648 (2009)
119 T. Stelzner, M. Pietsch, G. Andra, F. Falk, E. Ose, and S. Christiansen, Nanotechnology **19**, 295203 (2008)
120 L. Tsakalakos, J. Balch, J. Fronheiser, B. A. Korevaar, O. Sulima, and J. Rand, Appl. Phys. Lett. **91**, 233117 (2007)
121 E. C. Garnett and P. D. Yang, Journal of the American Chemical Society **130**, 9224 (2008)
122 J. A. Czaban, D. A. Thompson, and R. R. LaPierre, Nano Lett. **9**, 148 (2009)
123 H. Goto, K. Nosaki, K. Tomioka, S. Hara, K. Hiruma, J. Motohisa, and T. Fukui, Appl.Phys. Express **2**, (2009)

Chapter 2 Growth of Zinc Oxide Nanowires

2.1 Background

Zinc oxide, a multiple functional II-VI semiconductor, has a wide range of properties, including wide-bandgap semiconductivity, symmetric doping, piezoelectricity, pyroelectricity, high-transparency, room-temperature ferromagnetism and surface sensitivity to the environment, giving rise to versatile applications in facial powders, ointments, sunscreens, catalysts, lubricant additives, paint pigmentations, piezoelectric transducers, light emitting diodes, scintillators, spintronics devices, transistors, gas/biosensors, and transparent conducting electrodes, etc[1-5]. Notably, in comparison with GaN, ZnO has a large exciton binding energy (~60meV), higher radiation hardness and relatively low cost, which make it interesting as a laser material in the optoelectronics industry[6-8].

ZnO naturally crystallizes in wurtzite structure, in which a number of alternating planes composed of tetrahedrally coordinated O^{2-} and Zn^{2+} ions, stacked alternately along the *c*-axis, exhibiting spontaneous polarization along the *c*-axis and divergent surface energy[9]. The {0001} polar surface in ZnO, together with the three fastest growth directions, <0001>,<01-10>, and <2-1-10>, facilitate the growth of the various ZnO nanostructures[10,11]. These nanostructures, including nanowires, nanobelts, nanorods, nanorings, nanotubes, nanocombs, nanosaw, nanobowls and nanotrees, etc., open the opportunity to understand the size and morphologyrelated physical phenomena and develop novel nanodevices with superior performance[5,9,11,12]. For instance, nanolaser[13,14], nanosensor[15,16], nanocantilevers[17] and nanogenerators[18,19] have been demonstrated in ZnO nanowires or nanobelts.

Due to its high visible light transparency, ZnO is generally not considered as light absorption material in solar cells and is commonly used as the window layer or conducting electrode. However, ascribed to the development of nanotechnology, nanostructured ZnO, especially ZnO nanowire, plays an important role in light absorption and carrier collections, holding great promise for next-generation photovoltaic device fabrication. First, ZnO nanowire array can be

used as an efficient antireflective layer because of the light trapping effects in the nanowire array. Especially, the light absorption in ZnO nanowire array can be further tailored by adjusting the length, density and geometry of the nanowires[20]. Increased efficiencies have been demonstrated in ZnO nanowire array coated CIGS and silicon solar cells[21,22]. Second, an array of ZnO nanowire usually possesses single crystalline nature, which can act as good carrier transport channels and therefore significantly enhance the charges collections. So far, there have been a number of reports using ZnO nanowire array as photoanodes in DSSCs, QDSCCs and other photochemical devices[23-26]. Moreover, the absorption spectrum of ZnO nanowire can be tuned by coupling ZnO with another semiconductor to construct a coaxial nanocable[27, 28]. Additionally, several investigations have demonstrated that doping ZnO nanostructure is an efficient way to tailor the light absorption in ZnO nanomaterials[29,30].

Many methods have been developed to grow ZnO nanostructures, and generally they can be classified as gas phase and liquid phase approaches. The former includes CVD, thermal evaporation, metalorganic chemical vapor deposition (MOCVD), PLD, and etc. Depending on whether the catalyst is involved or not, the gas phase growth of ZnO is either governed by vapor-liquid-solid (*VLS*) or vapor-solid (*VS*) mechanism. Hydrothermal and solvothermal are generally recognized as representative liquid phase approaches. Different approach has its own advantages and drawbacks. Generally, traditional gas phase routes require economically prohibitive temperatures (800 ^{o}C~1300 ^{o}C) and expensive and/or insulating substrates (for instance, sapphire or GaN coated sapphire) for oriented nanowire growth, substantially hindering the commercial potential of gas-phase-growth ZnO nanowire array in optoelectronic applications. On the other hand, hydrothermal growth of ZnO nanowire array is appealing because of the low growth temperature (70^{o}C~95^{o}C), potential to scale-up and no clear substrate preference. However, solar cells consisting of hydrothermally grown ZnO nanowire array always suffer from the high series resistance originating from the rather low conductivity and the possible surface contamination of ZnO nanowires[31]. Therefore, it is highly desired to obtain high quality ZnO nanowire array on transparent conductive substrates.

In this chapter, large-area ZnO nanowire arrays synthesized by CVD on ITO substrates were demonstrated. For comparison, well-aligned ZnO nanowire arrays were also synthesized on sapphire substrates. The electrical properties and optical properties of the ZnO nanowires were investigated by measuring the *I-V* characteristics of a single nanowire and room temperature

photoluminescence spectroscopy. Finally, two interesting morphologies of ZnO nanostructures are introduced and discussed.

2.2 ZnO nanowire array grown on ITO by CVD

Synthesis

The synthesis was carried out in a horizontal tube furnace. Briefly, one piece of zinc foil (Alfa Aesar, 0.01 inch thick, 99.9%. metals basis) with an area of ~1 cm ×1 cm was first placed on a silicon substrate and then loaded at the center of the quartz tube which was inserted in the furnace. An ITO substrate (Delta Technologies, R_S=15~25 Ω) was cleaned using a standard wafer cleaning procedure and set to a fixed distance (1.0 inch) away from the zinc foil in the downstream. Prior to elevating the temperature, the tube was pumped down to 10^{-3} Torr by a rotary pump to eliminate the oxygen residue in the system. An argon flow of 50 SCCM argon was then introduced into the tube until the temperature ramped to 420 ^{o}C at the rate of 27 ^{o}C/min.

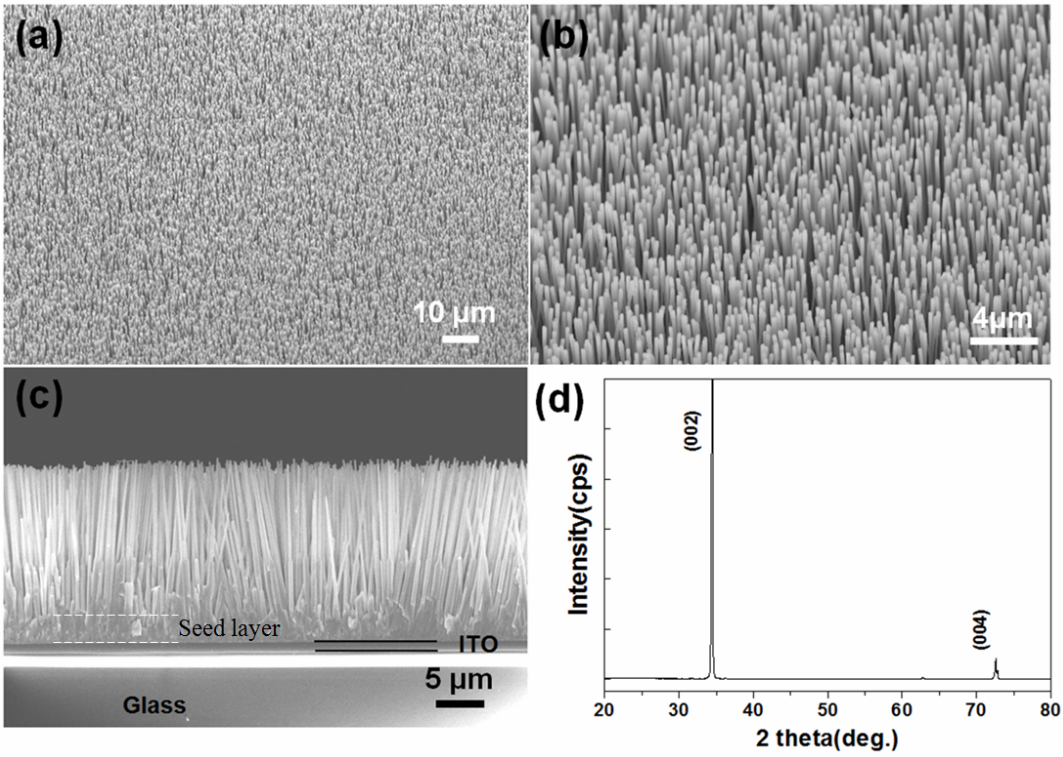

Figure 2.1 SEM images of ZnO nanowire array on ITO substrate. (a) and (b) low magnification SEM image taken by 45 ^{o}C tilted view, showing large-area uniform nanowire array vertically aligned on ITO substrate. (c) Cross-section view SEM image of ZnO nanowire array with an average length of 15 μm.(d) XRD pattern of ZnO nanowire directly grown on ITO.

Subsequently, a mixture of argon and oxygen (5:1) with a total flow of 60 SCCM was used to oxidize and transport the zinc vapor to the downstream. The temperature of the furnace was then raised to 600 ^{o}C and maintained for 30 minutes. The pressure inside the tubes was maintained at 8 Torr. After cooling to room temperature, the white yellow products on ITO and zinc foil residue on silicon substrate were taken out from the tubes for characterization.

The morphology and crystal structures of product harvested on ITO substrate were examined by SEM and XRD. Large-area vertically- aligned ZnO nanowire array was found to on the ITO substrate, as shown in a lower magnification SEM image (Figure 2.1 (a)). A large 45^{o} titled SEM image of the nanowire array in Figure 2.1 (b) revealed that the average diameter of nanowires is around 150 nm. The lengths of ZnO nanowires were measured to be around 15 μm from the cross-section SEM images in Figure 2.1(c). XRD was employed to determine the crystal structure of the ZnO nanowire array. One dominant peak and one relatively weak peak, which respectively corresponds to (002) and (004) planes of ZnO, were observed, suggesting that the ZnO product has strong preferential growth direction along the *c*-axis. In fact, we have been able to obtained well-aligned ZnO nanowire array with an area of 1 inch×1 inch on ITO substrate. For comparison, zinc power was also used to grow nanowire array under the same condition. However, nanowires were barely observed on the ITO substrate. Hence, we believe that the source material, i.e., zinc foil, has a crucial contribution to this uniform, well-aligned and large area ZnO nanowire array growth. In the initial stage, zinc foil is heated to a certain temperature, which is generally higher than 420 ^{o}C, and generates a uniform, high density zinc vapor due to the thin and large surface area. This dense vapor is then transferred and condensed on the ITO substrate in the near downstream and instantly oxidized, leading to a *c*-axis oriented ZnO seed layer because of the polarity of the wurtzite structure[11]. The nutrition is then continuously supplied by the evaporation of zinc foil, and the oriented ZnO, acting as the seed layer, favors the subsequent ZnO nanowire array growth following the VS mechanism. This seed layer can be identified from the cross-section SEM image in Figure 2.1(c), which is heighted by the dash line.

We also examined the products on the zinc foil residue on the silicon substrate by SEM and XRD. Lower magnification SEM image, as shown in Figure 2.2 (a), revealed that high density nanowires were obtained on the residue. At some location, nanowires are well aligned but most of them are radially distributed. This observation is consistent with previous work from our group[32]Higher magnification SEM images of the aligned and radially distributed nanowire are shown in Figure 2.2 (b) and (c), respectively. This growth process can be understood by the zinc foil evaporation and *in situ* oxidization, where the zinc foil acts as both template and source material. Figure 2.2 (d) displays a typical XRD pattern of the ZnO nanowires. The diffraction peaks can be indexed to a hexagonal structure of bulk ZnO with cell constants of a = 3.24 and c = 5.19. No diffraction peaks from Zn were found in the sample, which suggested that the zinc foil was totally oxidized into ZnO.

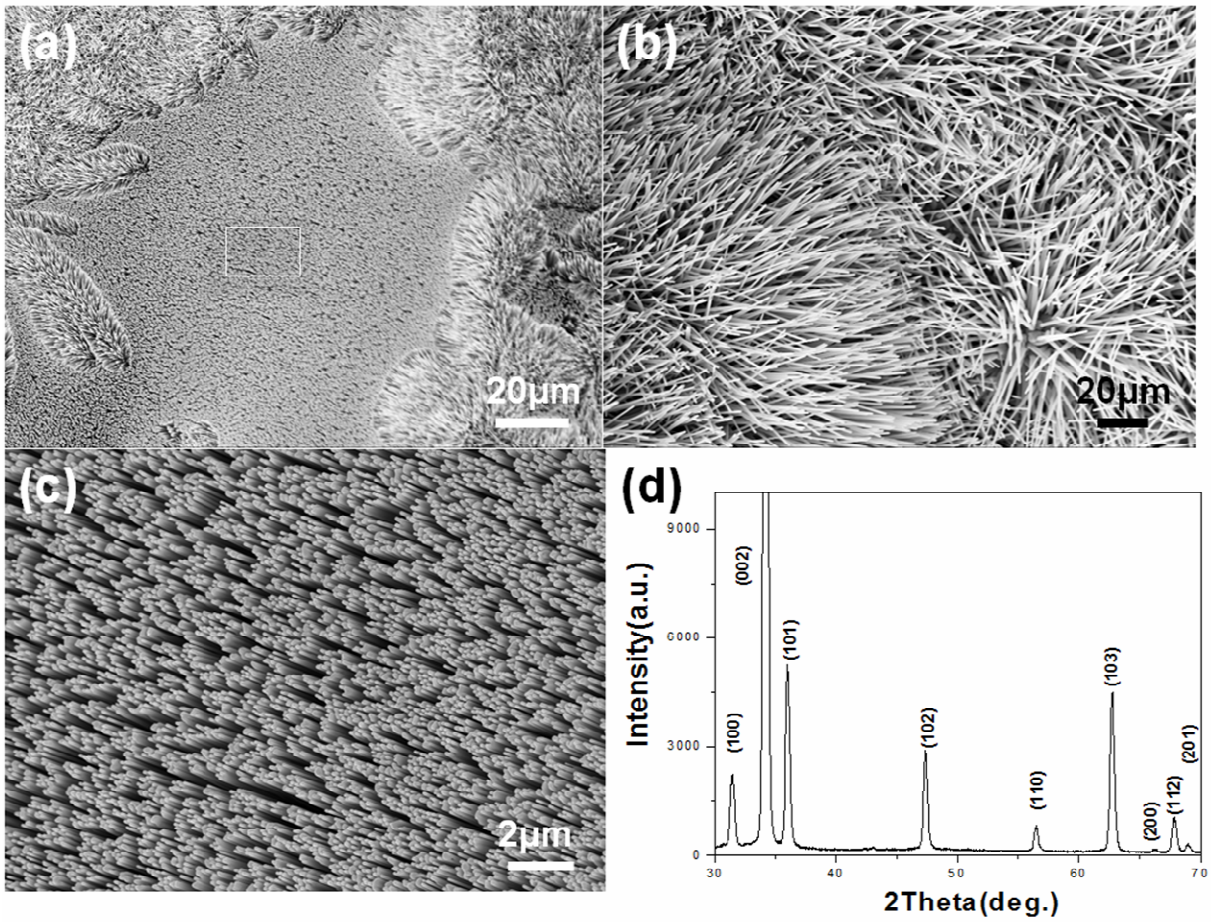

Figure 2.2 SEM images of ZnO nanowire on zinc foil residue. (a) Low magnification SEM image of the nanowires, showing high dense nanowires collected on the residue. (b) and (c) Larger magnification SEM images of ZnO nanowires, indicating both aligned and non-aligned nanowire were obtained on the reisdu. (d) XRD pattern of ZnO nanowires directly grown on zinc foil.

Room temperature photoluminescence of ZnO nanowire array synthesized from zinc foil and nanowire harvested on the ITO substrate was shown in Figure 2.3. The PL spectrum of the as-grown sample on the zinc foil residue shows a weak UV emission peaking at □389 nm and a dominant, broad, visible emission centered at 520 nm. In contrast, a very strong UV emission and relatively weak visible emission was observed in the PL spectrum of the ZnO nanowire array collected on the ITO substrate. The UV emission is understood as near-band-edge (NBE) emission, namely the recombination of free excitons through an exciton-exciton collision process. The visible emission, i.e., deep level emission (DLE), is generally attributed to a variety of deep level defects, e.g. vacancies and both oxygen and zinc interstitials, despite numerous debates.

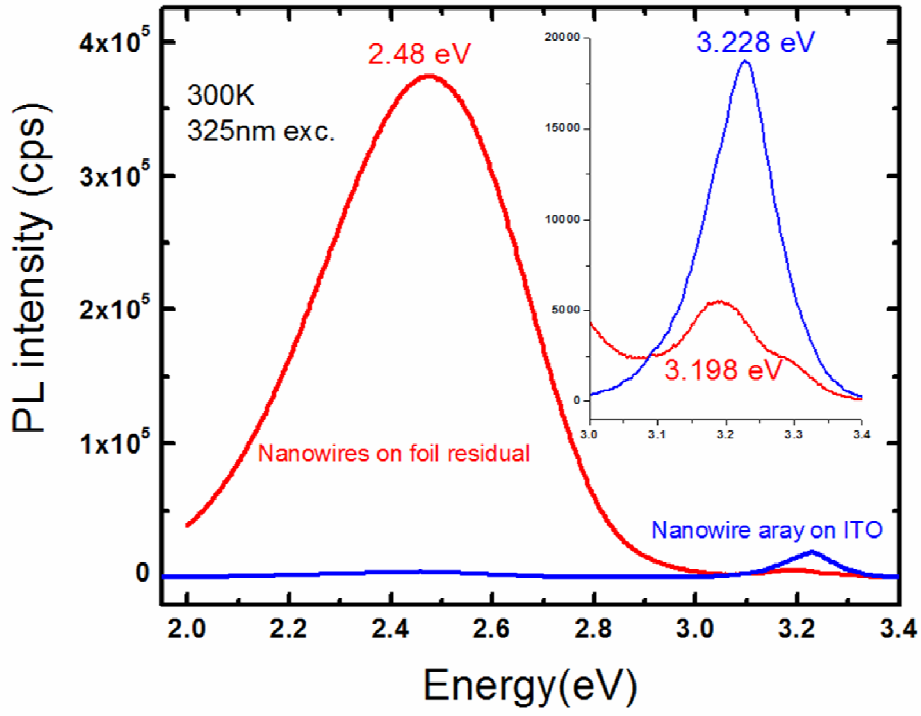

Figure 2.3 Room-temperature photoluminescence spectra of ZnO nanowires obtained on ITO and zinc foil residue.

For the ZnO nanowire on the residue, the zinc foil was gradually evaporated and oxidized, resulting in a zinc-rich atmosphere around the zinc foil. This oxygen deficiency is exacerbated when the introduced oxygen was partially consumed to grow ZnO nanowire array on ITO. The observation of a thick layer of ZnO, oxidizing from the residue of zinc foil, underneath ZnO nanowire array also confirmed this assumption[32]. Therefore, we ascribe the green emission in

the ZnO nanowire mainly to the oxygen vacancies. In the case of the ZnO nanowire array obtained on the ITO substrate, the sharp excitonic emission and very weak green emission indicates that the ZnO nanowires have a low defect concentration.

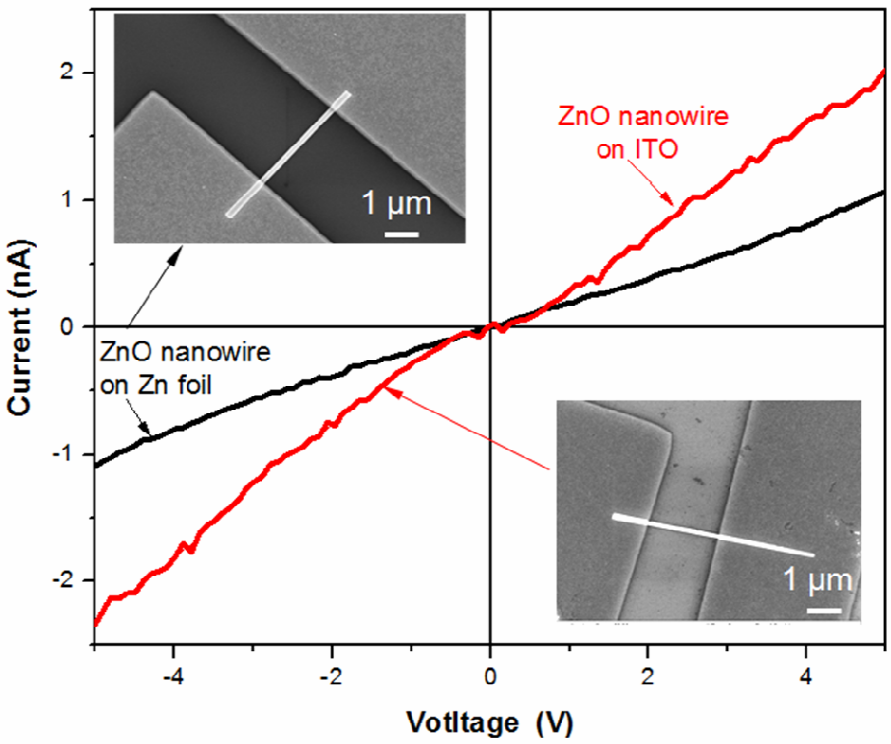

Figure 2.4 Electrical measurements of ZnO nanowires. The inset SEM images show the devices bridging across a pair of Ti/Au electrodes.

The electrical properties of the nanowires were investigated by *I-V* curve measurement. The corresponding devices are shown in Figure 2.4. Both *I-V* curves show nearly linear behavior, suggesting Ohmic contact between the nanowire and the Ti/Au electrode. Both samples have resistances on the order of 10^9 Ω. The resistivity, ρ, is an important parameter to evaluate the electrical properties of materials because it is inversely proportion to the charge carrier concentration, *n,* and to the mobility, μ. Therefore, we have also deduced the resistivity (ρ) of the nanowire from the *I-V* curve by using the formula

$$\rho = R\pi r^2/L$$

where *R* is the resistance obtained from *I-V* curve, *r* is the radius and *L* is the length of the measured nanowire, respectively. Both samples exhibit resistivities on the order of 10^2 Ωcm. It is well-known that many factors influence the resistance measurement of a single nanowire

device, such as contact resistances, measurement techniques (two probes or four probes), crystallinity, structure/morphologies difference and ambient condition. Herein, we used a two-probe measurement technique and the same electrode materials in the same ambient to obtain the resistivity. Without any doping, the general resistivity of ZnO nanowire synthesized by gas transport method was reported to range from 10^{-3} to 10^{5} Ωcm[33]. Our measurement here indicates that ZnO nanowire synthesized on ITO substrate have a rational resistivity for device fabrication. Moreover, both nanowires have the same order in resistivity, implying that the high-intensity green emission of ZnO nanowires on the residue might originate from the oxygen-deficient layer underneath.

2.3 ZnO nanowire array on sapphire substrate by CVD

Synthesis

The well-aligned ZnO nanowire array on the sapphire substrate was synthesized by CVD in a 2-inch horizontal tube furnace. In brief, a mixture of equal amounts (by weight) of ZnO powder (Alfa Aesar, 99.99%, metal basis) and graphite powder (Alfa Aesar, -100 mesh, 99.9%, metal basis) were used as the evaporationsource. The *a*-plane sapphire substrate was cleaned by a piranha solution at 80^{o}C for 30min and rinsed thoroughly with water. A layer of gold (3 nm in thickness) was sputtered on the cleaned substrate to initialize the nanowire growth. A crucial factor in obtaining a highly oriented ZnO nanowire array is the location of the source material and substrate. 0.5 g source materials were loaded in the two ends of the crucible while the substrate was loaded in the center of the crucible. Subsequently, the crucible was inserted into the quartz tube and placed at the center of the furnace. Prior to the growth, the tube was pumped down to 30m Torr and a gas flow of argon at 50 SCCM was introduced into the tube. The temperature was increased to 950 ^{o}C at a ramping rate of 30 ^{o}C/min and the temperature was held at the peak temperature for 30min under a pressure of 200 Torr. SEM, XRD and PL spectroscopy were employed to investigate the morphology, structure and optical properties of the as-synthesized nanowire array. The electrical properties and UV response were studied in a single nanowire device.

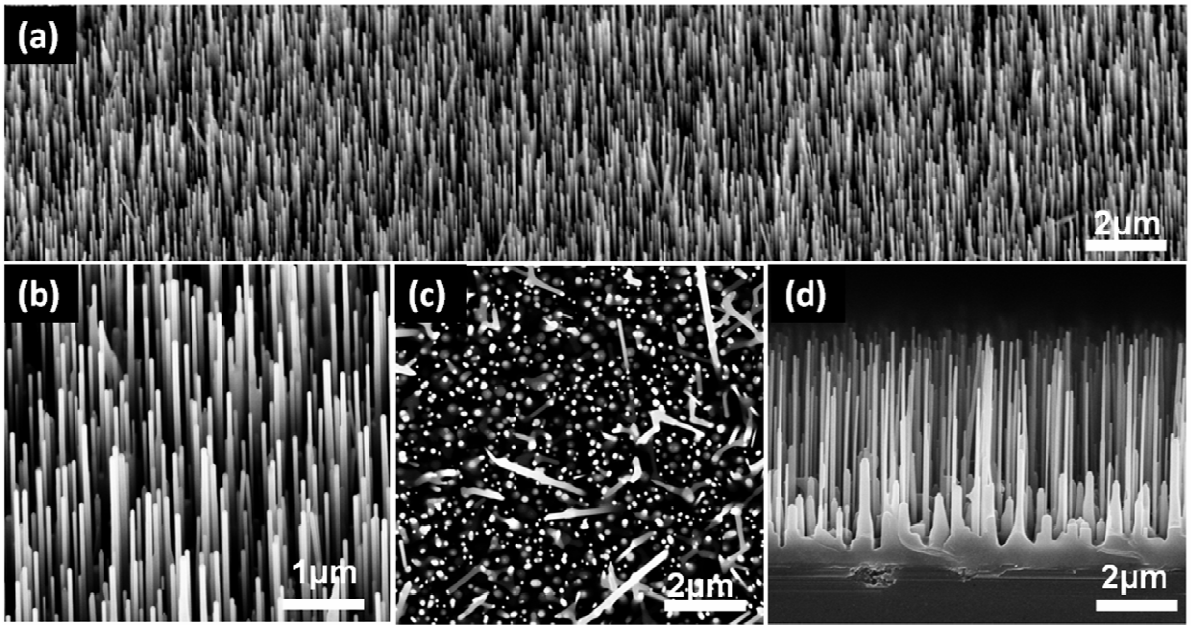

Figure 2.5 (a) 30°C tilted low-magnification SEM images, showing a large area uniform ZnO nanowire vertically aligned on the substrate. (b) ~ (d) large magnification SEM images taken by 30°C tilted, top view, and the cross-section view.

Figure 2.5 shows the morphologies of the ZnO nanowire array directly assembled on *a*-plane sapphire substrate. Low magnification SEM images of the nanowire array, as shown in Figure 2.5(a), indicate the nanowires are perpendicular to the substrate and are varied in length. In fact, our observation found that the entire sapphire substrate (1cm×1cm) was covered with nanowire array, with the exception of quasi-alignment on the edge of the substrate. The top-view SEM images confirmed that most of the nanowires were normal to the substrate. Some titled nanowires with thicker diameters were also observed and could be attributed to the defects of the recycled substrate. Interestingly, we also observed a continuous ZnO seed layer between the sapphire substrate and the nanowires, as shown in the cross-section SEM image (Figure 2.5(d)). In most cases, ZnO nanowire arrays synthesized by gas phase routes are directly grown on the sapphire substrate without the assistance of the seed layer, owing to the small lattice mismatching between sapphire and ZnO[13,34]. Nonetheless, if the cost of sapphire is admissable, the continuous ZnO layer, acting as a buffer, can be used to block/collect the carriers in optoelectronics and piezoelectronics. Herein, we also attributed the large area growth and buffer layer to our experimental design. In a traditional configuration, the collective substrates are

placed in the downstream, favoring the source species transport and condensation at low temperature. However, the condensation of the gas vapor prefers to occur at the location with the largest temperature gradient, leading to a variation in length, diameter, density and the resulting properties of nanowires. In our specific layout, the substrate is kept at the center of the tube, ensuring only a negligible temperature gradient along the substrate. The equal amount of source materials was located at both ends of the crucible, providing a uniform distribution of gas vapor density because of the asymmetric diffusion area. Two kinds of nanowires with different morphologies can be identified. The longer and thinner ones show no catalyst on the tip while the shorter and thicker ones exhibit catalysts at the tip. This is direct evidence proving that both VLS and VS growth mechanism are involved in the nanowire growth. The difference in the lengths of the nanowires implies that the growth rate governed by VS is faster than that governed by VLS at least during the initial growth period, given the possibility that the longer nanowires will block the accesses of ZnO species supplies to the short ones in the following stages.

As shown in Figure 2.6 (a), the XRD pattern of the ZnO nanowire array on the sapphire

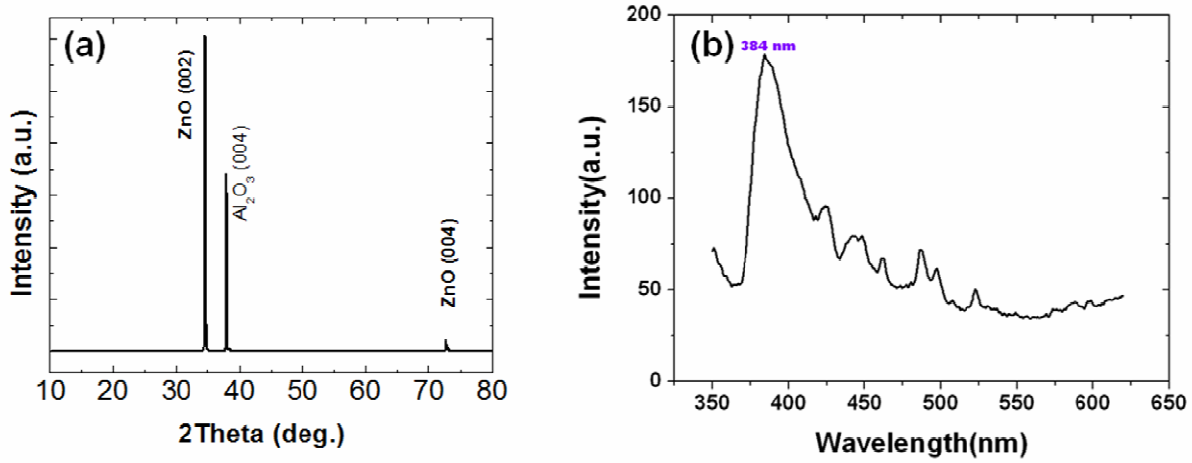

Figure 2.6 (a) XRD pattern of well-aligned ZnO nanowire on sapphiresubstrate.(b)Photoluminescence spectrum of ZnO nanowire array.

substrate exhibits a very sharp (002) diffraction peak at 34.52^{o} and a small (004) one at 72.62^{o}, illustrating the texture effect of the anisotropic morphology and the highly preferential orientation of the ZnO nanowires along the *c* -axis (normal to the substrate surface). An additional peak can be assigned to the (110) planes of the sapphire substrate. We also examine the optical quality of the ZnO nanowire array by PL spectroscopy. Figure 2.6 (b) was shown PL spectrum which consists of intense NBE UV emission with a wavelength maximum at 384 nm.

However, because the nanowire array and the epilayer underneath were measured together, the contribution of the ZnO epilayer to both the XRD and PL spectrum cannot be ruled out. In this regard, we fabricated the single nanowire device and investigate its *I-V* characteristics and photoresponse.

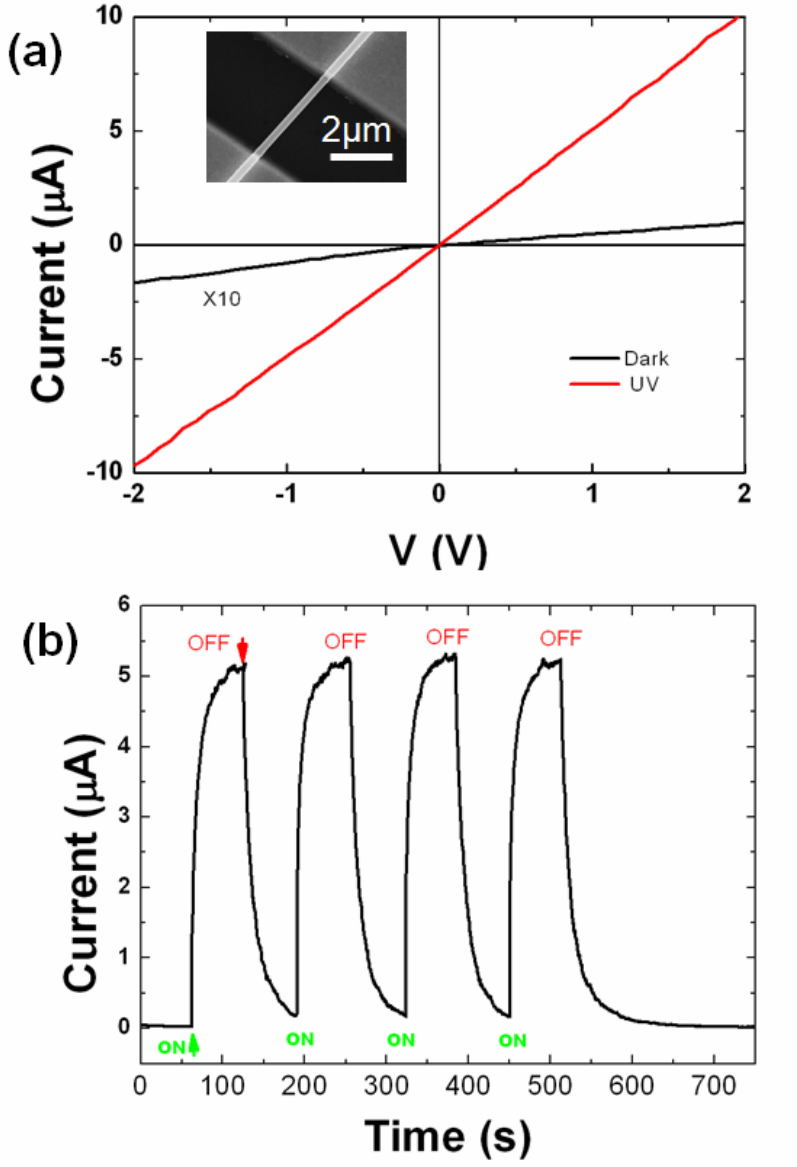

Figure 2.7 Electrical and photoresponse measurements of an individual nanowire. (a) *I-V* characteristics of the ZnO nanowire under dark and UV illuminated. Inset shows the device morphology. (b) Time-dependent measurements of photoresponse by switching on and off UV light.

We carried out the *I-V* characteristics in dark and under UV illumination based on a device consisting of a nanowire bridged across two Ti/Au electrodes. Both *I-V* curves exhibit linear behavior, indicating the Ohmic contact between the electrode and nanowires. Comparing to the curve in dark, the photocurrent increased by a factor of 50, under a UV density of 8.9 mW/cm^2 and a bias of 1V. Owning to the linearity of the *I-V* curve, the resistance of the nanowire can be roughly estimated as $10^7\ \Omega$. Correspondingly, we also deduced the resistivity of the nanowire on the order of $10^0\ \Omega cm$. Figure 2.7 shows the time-dependant photoresponse measurement by monitoring the change of the photocurrent upon switching the UV illumination ON and OFF. With a bias of 1 V, it was found that the photocurrent increased/decreased instantly while the UV illumination was ON/OFF, respectively. The relatively low resistance and large photocurrent gain, together with the fast recover/response rate, implied that the ZnO nanowires array grown on sapphire substrate had good electrical and optical properties, which can be mainly attributed to the high temperature (950^oC) synthesis approach.

2.4 Other ZnO nanostructures

2.4.1 ZnO nanourchins

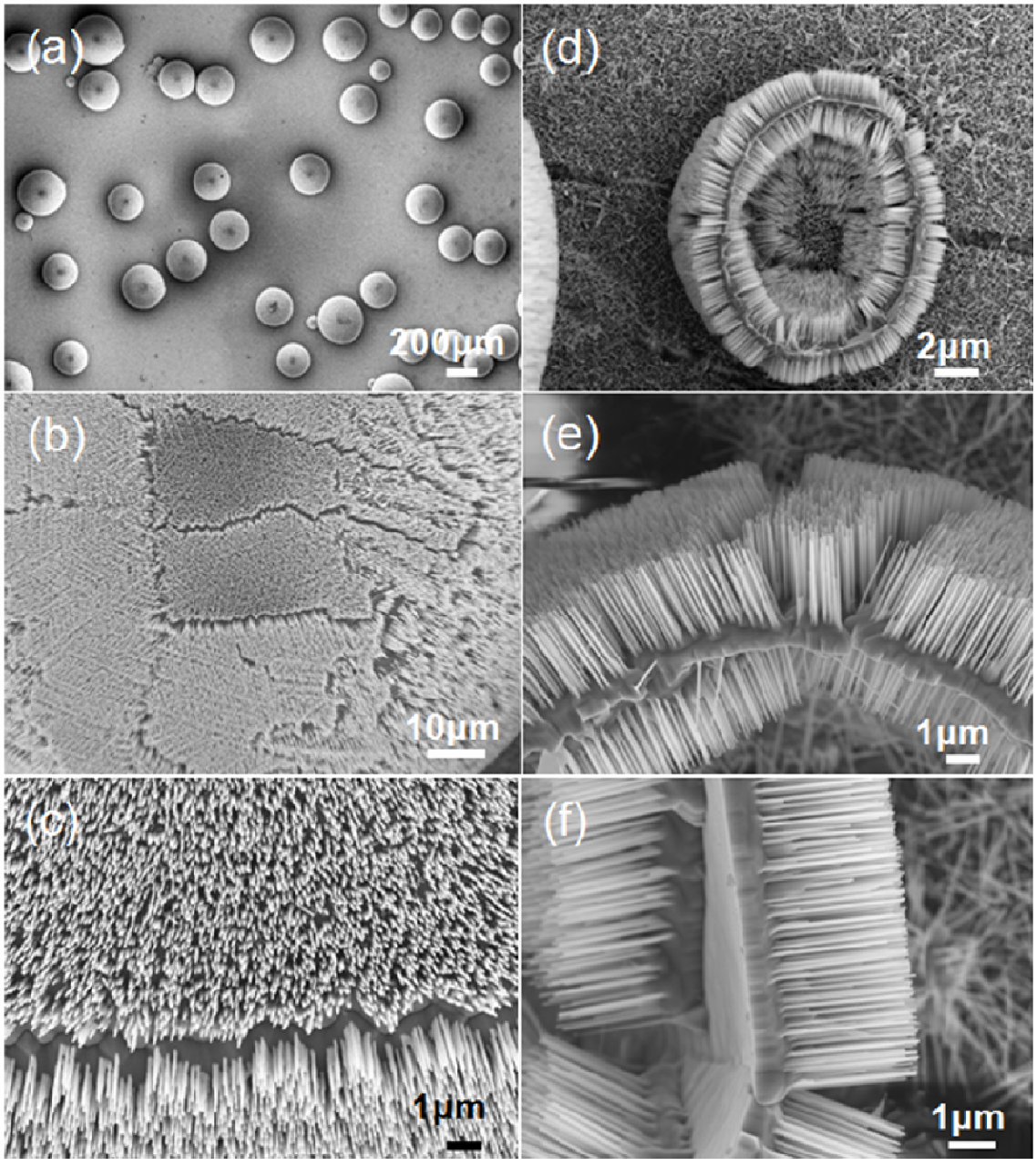

Figure.2.8 SEM images of nanourchins collected underneath zinc foil residue on silicon substrate. (a) Lower magnification SEM image shows nanourchins with different diameters. (b)~(c) enlarged SEM images of one urchin showing high density nanowire array directly assembled on the surface. (d) A low magnification SEM image of hemispheric nanourchin structures, well-aligned nanowire array are observed at both outer and inner surface. (e) and (f) Enlarged SEM images of the nanowire arrays on the urchin structure.

In the experiment to synthesize the ZnO nanowire array on the ITO substrate, we also checked the product underneath the residual zinc foil. Interestingly, some urchin-like structures were observed on the silicon substrate. The diameters of these urchin-like structures ranged from tens to hundreds of micrometers, as shown in Figure 2.8(a). Enlarged SEM images of the nanourchin revealed that high dense nanowires were aligned radially over the entire surface of the nanourchin. The nanowires exhibited uniform diameters and lengths of around 100 nm and 4 μm, respectively. Figure 2.8 (b) shows several boundaries without nanowires between adjacent nanowire arrays. Hemispheric nanourchin structures were also observed in some locations. A typical SEM image of such a structure was displayed in Figure 2.8(d), showing that both the external and internal surfaces are covered by well-aligned ZnO nanowire array. Higher magnification SEM images in Figure 2.8(e) and (f) clearly present that nanowire array were directly assembled on a 500nm ZnO layer. By analyzing the morphologies of the nanourchins and referring to the ZnO nanobowls and nanocages previously reported by our group[35], one general mechanism could be concluded. The zinc foil used in our case actually acts as both source and protecting cell. Firstly, once the temperature rises to 420 ^{o}C, zinc foil curves spontaneously to release the strain originating from different oxidization rate between the top and bottom surfaces, leading to a dome-like structure. Meanwhile, the bottom layer, now referred as internal wall, generates high density zinc vapor, which condenses on the silicon substrate and tends to incubate to micrometer sphere for reducing the surface energy. Because of the dome-like structure, the environment inside of the dome is more stable and has less oxygen than the outside of the dome. Secondly, while the temperature is increased, the surfaces of the micrometer Zn spheres are oxidized to ZnO and the cores are sublimed, leaving hollow structure on the silicon substrate. In fact, similar Zn/ZnO core-shell and ZnO hollow structures have been reported in nanowire and nanotubes by Kong *et al*[36]. It was also demonstrated in their work that the ZnO layer was epitaxially grown over zinc core before the zinc completely sublime. This could also explain the boundaries formation between adjacent nanowire arrays. Finally, supplied by the vapor from inner wall of the dome, highly aligned ZnO nanowire arrays are grown on the well crystallized ZnO layer. Overall, we attribute the growth of the unique morphology to the undisturbed state offered by the curved Zn foil and the well-crystallized ZnO layer after oxidization. However, to optimize the large-amount of nanourchins growth, several influential factors, including the partial oxygen pressure, temperature ramping rate, and gas flows, need to

be further investigated. Nanourchin structures have demonstrated potential applications in lithium-ion battery, supercopacitors[37] and solar cells[38]. However, most of these urchin structures were synthesized by solution phase routes[39-41]. ZnO nanourchin synthesized by CVD in this work can be used as a novel 3D nanoarchitecture for nanodevice assembly and integration in the future.

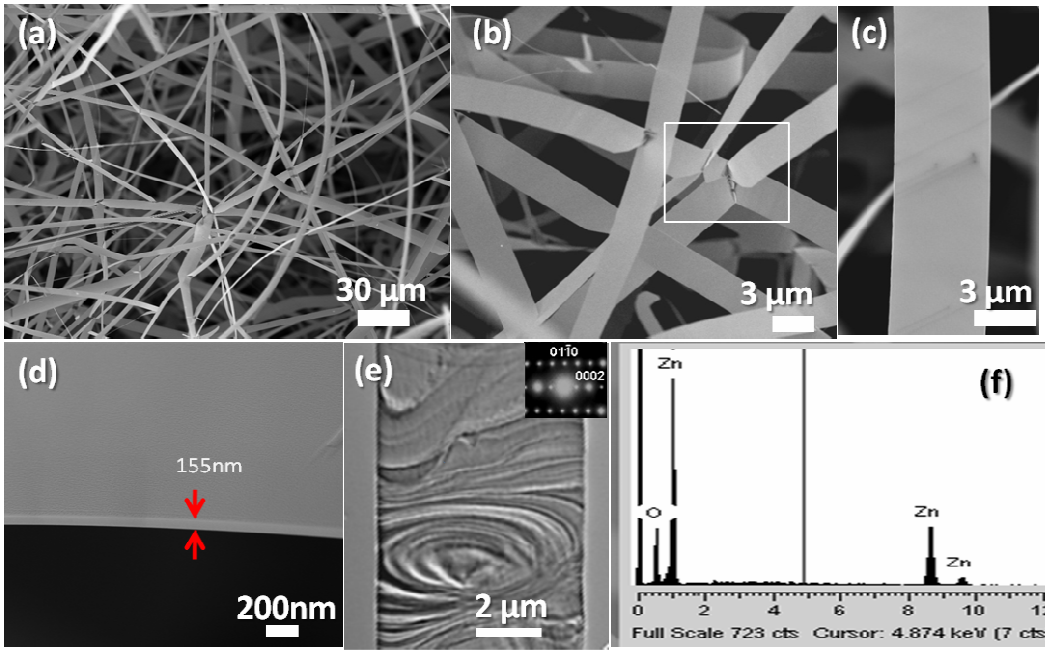

Figure.2.9 Morphology and structure analysis of ultra-wide nanobelts. (a)~(d) SEM images of ZnO nanobelt, showing the length, width and thickness, respectively.(e) TEM image of an individual ZnO nanobelt and corresponding SAED.(f) EDS data collected form white frame in (b), confirming no catalyst in the knot section of the nanobelts.

2.4.2 Ultra-wide ZnO nanobelts

Ultra wide ZnO nanobelts were also obtained by CVD techniques. The morphology and crystalline structure was first examined by SEM and TEM. Figure 2.9 (a) shows a lower magnification SEM image of the nanobelts, revealing that the nanobelts have a length of tens of micrometers. A higher magnification SEM was shown in Figure 2.9(b) suggesting that all the nanobelts were knotted together. The typical nanobelt with a very smooth surface exhibited a width of ~5 µm and a thickness of ~150 nm, which was measured by SEM and shown in

Figure.2.9 (c) and (d). TEM image of a ZnO nanobelt is presented in Figure 2.9(e), as well as the corresponding SAED, indicating ZnO nanobelts have a preferential growth direction along [01-10]. As shown in Figure 2.9 (f), an EDS spectrum was recorded in the knot area of the ZnO nanobelts and only Zn and O peaks are identified, confirming no catalyst involved in the structure.

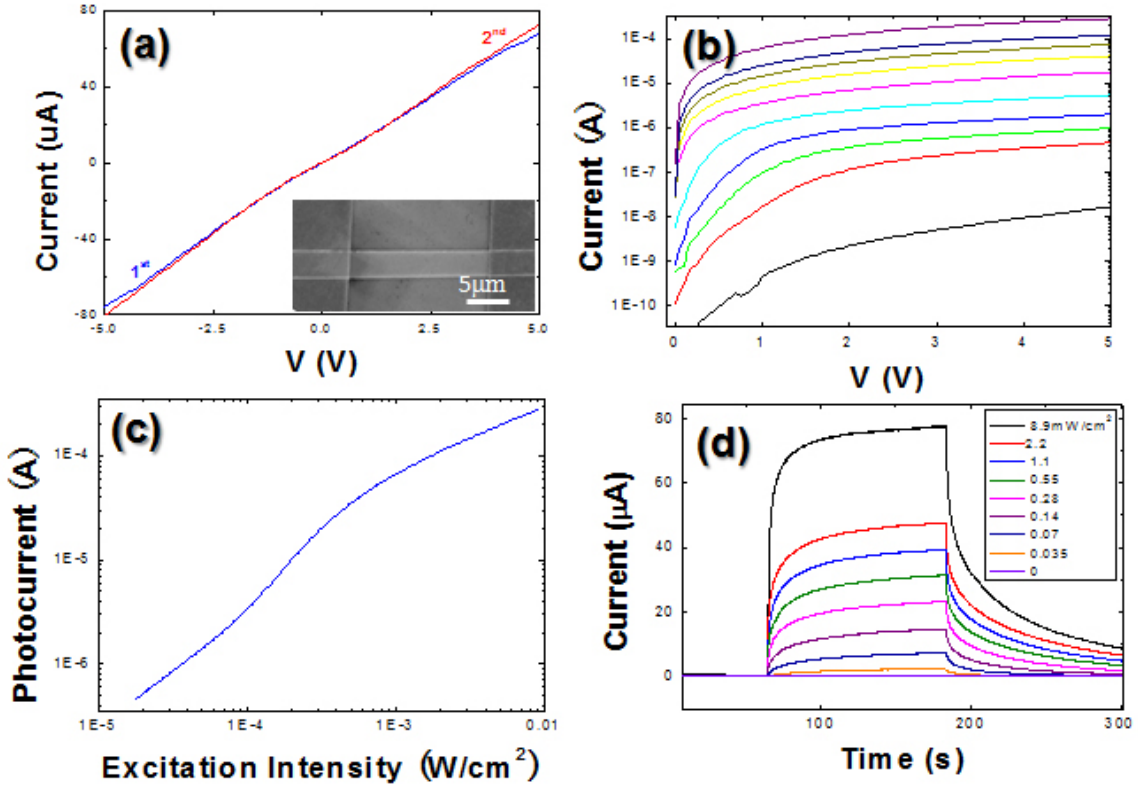

Figure 2.10 Electrical and photoresponse measurements of an individual nanobelt.(a) Two times electrical measurements. Inset shows the representative SEM image of the device.(b) I-V characteristics of the ZnO nanobelts under different irradiances on a logarithmic scale. (c) Photocurrent of a single ZnO NW device measured as a function of excitation intensity with +3 V applied bias.(d) Time-dependent measurements of photoresponse by switching on and off UV light with different irradiances.

The results of electrical and photoresponse measurements were conducted on an individual nanobelt bridging a pair of gold electrodes. The morphology of the device was presented in the inset of Figure 2.10 (a). We measured the *I-V* curves of the device several times in 30 days. The reproducibility and linearity of the *I-V* characteristics indicated that the Ohmic contact nature and stability between the electrodes and nanobelt. In order to investigate the photoresponse of the

nanobelt, we measured the *I-V* characteristics of the nanobelt under different densities of UV illumination and the data was plotted in logarithmic as shown in Figure 2.10 (b). Under a UV illumination intensity of 3.9 mW/cm^2, it was found that the current of the nanobelt increased by 5 orders in comparison to that in dark. The significant current increase can be explained by the absorption and desorption of oxygen molecules on the surface of ZnO nanobelts. Owing to its large surface aspect ratio and the resulting high density of dangling bonds, ZnO nanobelt absorb a large number of oxygen molecules, which extract the electrons from the conduct band of ZnO and form a depletion layer on the surface. As a consequence, ZnO nanobelt has a relatively lower carrier density and mobility. Illumined by photos with energy higher than the bandgap of ZnO, electron-hole pairs are generated and the holes will migrate to the surface because of the band bending[42]. The oxygen traps electrons then recombines with the migrated holes, leading to i) release of the oxygen molecules, ii) large number of unpaired electrons acting as majority carriers. When the UV light is turned off, the oxygen molecules are reabsorbed and the whole status is recovered in a short time period. The intensity dependence of the photocurrent measured at an applied bias of 3V is shown in Figure 2.10(c). The curve exhibits linearity at low intensity illumination and then becomes saturated when increasing the light intensity, which has a similar trend with the observation in ZnO nanowire[42]. The linearity can be easily explained by the fact that the carrier generation is proportional to the absorbed photon flux while the deviation from the linearity at high density illumination is believed to originate from the definite numbers of available hole-traps. The photoresponse rate and recover rate of a ZnO nanobelt, which is associated with the defects in the structures, is another indicator of the quality of the crystallinity. Therefore, we also studied the rise and decay time upon switching UV light on and off and the data is shown in Figure 2.10(d). Upon illumination with UV light, the photocurrent rise instantly and then gradually increases until the light is off, which clearly indicates two possible mechanisms behind. Delaunay *et al* assumed that there was a competing contribution of solid-state process and surface effect to the photocurrent increase[43]. The instantaneous rise of the current is supposed to be originated from the generation of electron-hole pairs and the gradual increase is associated with the surface effects. We also observed that the current decayed very fast in the beginning and then decreased at a very low rate, leading to a taile-shape curve. Considering the Ohmic contact between the electrode and nanobelt, we may rule out the possible contribution from the contact issue.

2.5 Conclusion

In summary, various ZnO nanostructures have been synthesized on different substrates via CVD approach and their morphologies, structures, electrical and optical properties have been investigated by comprehensive characterizations. Large-area and vertically-aligned ZnO nanowire array have been achieved on ITO/sapphire substrates by two different CVD approaches. ZnO nanowire array grown on ITO substrates exhibited a good alignment and the resistivity was estimated as 10^2 Ωcm, which was deduced from the *I-V* characteristics of a single nanowire device. In contrast, ZnO nanowire array grown on sapphire substrate at 950 ^oC have a resistivity of ~ 10^0 Ωcm. Considering the requirement of the solar light harvesting in a practical device, vertically aligned ZnO nanowire array synthesized on ITO by CVD at an intermediate temperature, have a great potential because it employs a transparent electrode material as the substrate while retaining a good optical and electrical properties. Nanourchins and ultra-wide nanobelts were obtained and their unique structures enrich the family of ZnO nanomaterials and offer the opportunity to design and fabricate novel optoelectronic device by taking advantage of the morphologies.

Reference

1 U. Ozgur, Y. I. Alivov, C. Liu, A. Teke, M. A. Reshchikov, S. Dogan, V. Avrutin, S. J. Cho, and H. Morkoc, Journal of Applied Physics **98**, (2005)
2 A. Janotti and C. G. Van de Walle, Rep. Prog. Phys. **72**, (2009)
3 P. A. Rodnyi and I. V. Khodyuk, Optics and Spectroscopy **111**, 776 (2011)
4 K. Schilling, B. Bradford, D. Castelli, E. Dufour, J. F. Nash, W. Pape, S. Schulte, I. Tooley, J. van den Bosch, and F. Schellauf, Photochemical & Photobiological Sciences **9**, 495 (2010)
5 L. Schmidt-Mende and J. L. MacManus-Driscoll, Materials Today **10**, 40 (2007)
6 M. T. Chen, M. P. Lu, Y. J. Wu, J. H. Song, C. Y. Lee, M. Y. Lu, Y. C. Chang, L. J. Chou, Z. L. Wang, and L. J. Chen, Nano Letters **10**, 4387 (2010)
7 Y. S. Choi, J. W. Kang, D. K. Hwang, and S. J. Park, Ieee Transactions on Electron Devices **57**, 26 (2010)
8 E. Fortunato, A. Goncalves, A. Pimentel, P. Barquinha, G. Goncalves, L. Pereira, I. Ferreira, and R. Martins, Applied Physics a-Materials Science & Processing **96**, 197 (2009)
9 Z. L. Wang, Journal of Physics-Condensed Matter **16**, R829 (2004)
10 Z. L. Wang, ACS Nano **2**, 1987 (2008)
11 Z. Y. Fan and J. G. Lu, Journal of Nanoscience and Nanotechnology **5**, 1561 (2005)
12 W. Gao and Z. W. Li, International Journal of Nanotechnology **6**, 245 (2009)
13 M. H. Huang, S. Mao, H. Feick, H. Q. Yan, Y. Y. Wu, H. Kind, E. Weber, R. Russo, and P. D. Yang, Science **292**, 1897 (2001)
14 J. C. Johnson, H. Q. Yan, R. D. Schaller, L. H. Haber, R. J. Saykally, and P. D. Yang, Journal of Physical Chemistry B **105**, 11387 (2001)
15 L. Liao, H. B. Lu, J. C. Li, C. Liu, D. J. Fu, and Y. L. Liu, Applied Physics Letters **91**, (2007)
16 M. J. S. Spencer, Progress in Materials Science **57**, 437 (2012)
17 Y. H. Huang, X. D. Bai, and Y. Zhang, Journal of Physics-Condensed Matter **18**, L179 (2006)
18 Z. L. Wang, Advanced Functional Materials **18**, 3553 (2008)
19 Z. L. Wang and J. H. Song, Science **312**, 242 (2006)
20 Y. H. Ko and J. S. Yu, Optics Express **19**, 297 (2011)
21 J. Y. Chen and K. W. Sun, Solar Energy Materials and Solar Cells **94**, 930 (2010)
22 L. Ae, D. Kieven, J. Chen, R. Klenk, T. Rissom, Y. Tang, and M. C. Lux-Steiner, Progress in Photovoltaics **18**, 209 (2010)
23 C. H. Ku and J. J. Wu, Applied Physics Letters **91**, (2007)
24 A. R. Rao and V. Dutta, Nanotechnology **19**, (2008)
25 R. S. Aga, D. Jowhar, A. Ueda, Z. Pan, W. E. Collins, R. Mu, K. D. Singer, and J. Shen, Applied Physics Letters **91**, (2007)
26 K. S. Leschkies, R. Divakar, J. Basu, E. Enache-Pommer, J. E. Boercker, C. B. Carter, U. R. Kortshagen, D. J. Norris, and E. S. Aydil, Nano Letters **7**, 1793 (2007)
27 Y. Zhang, L. W. Wang, and A. Mascarenhas, Nano Letters **7**, 1264 (2007)
28 J. Schrier, D. O. Demchenko, and L. W. Wang, Nano Letters **7**, 2377 (2007)
29 J. M. Wu, C. W. Fang, L. T. Lee, H. H. Yeh, Y. H. Lin, P. H. Yeh, L. N. Tsai, and L. J. Lin, Journal of the Electrochemical Society **158**, K6 (2011)
30 J. W. Lo, C. A. Lin, and J. H. He, Current Nanoscience **7**, 282 (2011)

31 B. D. Yuhas and P. D. Yang, Journal of the American Chemical Society **131**, 3756 (2009)
32 J. J. Liu, M. H. Yu, and W. L. Zhou, Applied Physics Letters **87**, (2005)
33 E. Schlenker, A. Bakin, T. Weimann, P. Hinze, D. H. Weber, A. Golzhauser, H. H. Wehmann, and A. Waag, Nanotechnology **19**, (2008)
34 G. D. Yuan, W. J. Zhang, J. S. Jie, X. Fan, J. A. Zapien, Y. H. Leung, L. B. Luo, P. F. Wang, C. S. Lee, and S. T. Lee, Nano Letters **8**, 2591 (2008)
35 J. J. Liu, M. H. Yu, and W. L. Zhou, Journal of Applied Physics **99**, (2006)
36 X. Y. Kong, Y. Ding, and Z. L. Wang, Journal of Physical Chemistry B **108**, 570 (2004)
37 S. D. Perera, B. Patel, J. Bonso, M. Grunewald, J. P. Ferraris, and K. J. Balkus, Acs Applied Materials & Interfaces **3**, 4512 (2011)
38 X. W. Lou, L. A. Archer, and Z. C. Yang, Advanced Materials **20**, 3987 (2008)
39 H. B. Lu, S. M. Wang, B. H. Dong, Z. X. Xu, L. Zhao, and J. C. Li, J. Phys. Soc. Jpn. 79, (2010)
40 S. Jeon and K. Yong, Chemical Communications7042 (2009)
41 O. M. Bakr, B. H. Wunsch, and F. Stellacci, Chemistry of Materials **18**, 3297 (2006)
42 C. Soci, A. Zhang, B. Xiang, S. A. Dayeh, D. P. R. Aplin, J. Park, X. Y. Bao, Y. H. Lo, and D. Wang, Nano Letters **7**, 1003 (2007)
43 Y. B. Li, F. Della Valle, M. Simonnet, I. Yamada, and J. J. Delaunay, Nanotechnology **20**, (2009)

Chapter 3 All Inorganic Core-Shell Nanowire Array with Type II Heterojunction for 3D Photovoltaic Device Fabrication*

3.1 Background

The charge separation of the electron and hole is a key step to generate solar power in a photovoltaic device. In a conventional solar cell, it is typically achieved by a planar *p-n* homojunction along the path of the current flow or longitudinally. In nano-architecture PV devices, however, the charge separation is often facilitated by a type II or staggered energy alignment of a heterojunction, constructed by two materials for which both the valance and conduction band of one component lie respectively lower in energy than those of the other component. Such heterojunctions have been intensively investigated for solar cell applications, including DSSCs[1], QDSSCs[2,3], nanocrystal-polymer hybrid[4], and bilayer nanocrystal films[5]. To improve the carrier transport within the type II scheme, semiconductor nanowires have already been used to serve as the electron transporter in the inorganic-organic hybrid approach,[6-9] and recently a Core-shell all-inorganic nanowire architecture has been proposed to improve the carrier transport for both the electron and hole and simultaneously the device stability, using the well-known II-VI and III-V binary semiconductors, such as ZnO/ZnSe, ZnO/ZnTe, CdSe/CdTe, and GaN/GaP, and GaN/GaAs[10,11]. Here the type II transverse heterojunction functions similarly as a radial *p-n* junction[12,13] but without having to deliberately dope the nanostructure. In addition, the type II Core-shell structure may extend the absorption profile to a wavelength longer than that defined by the bandgap of any of the components through a relatively weak interface transition, as illustrated by the band diagrams of two semiconductors with bandgap Eg1 and Eg2 in Figure 3.1.(a) [10,11,14]. For mesoscopic scale devices[15,16], combing two operation mechanisms,

---

* Adapted in part by permission from i) K. Wang *et al*. Advanced Materials, **2008**, 20, 3248. Copyrig2008 Wiley-VCH Verlag GmbH & Co. KGaA. ii) K.Wang *et al*. Applied Physics Letters, **2010**, 96,123105. Copyright 2010 American Institute of Physics. Please check Appendix.

p-n junction and type II junction, will allow a greater flexibility in optimizing the cell performance.

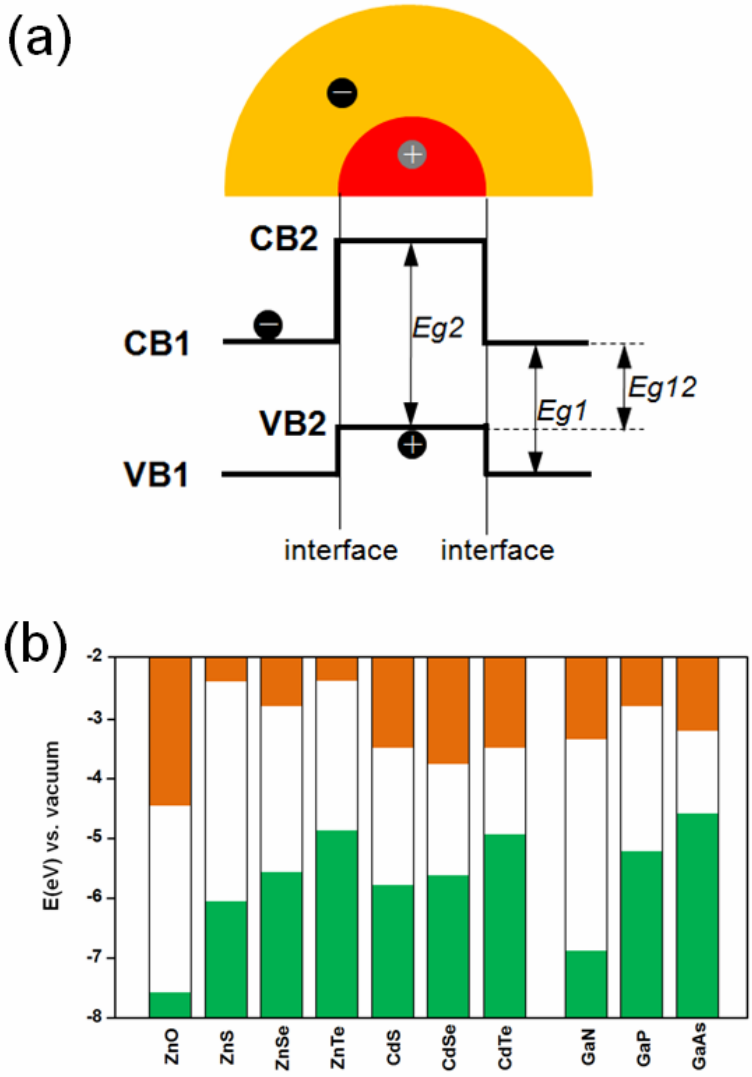

Figure 3.1 Schematics of (a) Type II band-edge alignment at the heterointerface between two semiconductors tends to spatially separate the electron and the holes on different sides of the heterointerface. The interfacial emission energy is determined by Eg12. (b) Electronic energy levels of selected II-VI and III-V semiconductors showing the materials selection to construct type II heterojunction.

Figure 3.1.(b) depicts the energy levels of common II-VI and III-VI semiconductors, providing several possible materials combinations with Type-II band alignments. Using highly

lattice-mismatched combinations such as ZnO/ZnSe, and ZnO/ZnS is more challenging in synthesis than less mismatched combinations such as CdSe/CdTe,but it offers more electronic structure tunability and better material stability. In special, ZnO and ZnS are direct wide-bandgap semiconductors with bandgaps of 3.37, and 3.60 eV, respectively, and are commonly used as efficient antireflection layers and/or carrier-transport media in dye- and quantum dot-sensitized solar cells[17-19]. However, the bandgap of the ZnO/ZnS Core-shell quantum wire has been predicted to reach as low as 2.07 eV, corresponding to a Shockley-Queisser efficiency limit of up to 23%[20]. Furthermore, ZnO and ZnS are environmental friendly, composed of abundant and chemically stable elements.

Vertically aligned nanowire array with the entire nanowire surface well-exposed, provides an ideal platform for further engineering. In order to fabricate core-shell nanowire structures, most of the vapor phase thin film fabrication techniques can be used for shell layer deposition. However, some techniques with strong directional particle trajectory, such as evaporation, have a severe shadow effect that will result in uneven coating. PLD is a versatile, effective and scalable technique in thin film deposition. During PLD, many experimental parameters including wavelength, pulse duration, repetition rate, target-to-substrate distance, substrate temperature, background gas and pressure, can be altered, which all influence the thin film growth.

In this chapter, we report a success in synthesizing ZnO/ZnSe and ZnO/ZnO core-shell nanowires on a large area transparent conducting substrate, using a relatively simple and low-cost approach of combining CVD and pulsed laser deposition PLD techniques. Their structural and optical properties are characterized by applying a set of comprehensive techniques. Although there have been many reports for the vertically aligned single-component nanowire array or type I Core-shell nanowire array on large substrates[21-24], and there is also a report on non-vertically aligned GaN/GaP Core-shell nanowires[25], there is little effort on the synthesis of the vertically aligned type II Core-shell nanowire array, in particular using highly mismatched binaries. The success of this effort is a key step toward the demonstration of a new viable nano solar cell technology.

3.2 ZnO/ZnSe core-shell nanowire array

3.2.1 Experimental

***Synthesis of ZnO nanowire array*:**

To synthesize large-area ZnO nanowire array, a piece of thin zinc foil was used to generate high pressure zinc vapor in a tube furnace. Briefly, the Zn foil and ITO substrate were sequentially laid down with a distance of 5 mm in a ceramic boat, which was then transferred to the center of a 2-in. diameter quartz tube furnace. The quartz tube was first evacuated to 10 mTorr, and a 40 SCCM argon was introduced into the tube, which was then heated to 600^{o}C at a rate of 30^{o}C/min. When the temperature exceeded 420^{o}C (the melting point of Zn), a 70 SCCM air flow was also introduced into the quartz tube. The reaction was kept for 30 min after the temperature reached 600^{o}C. By controlling the pumping rate, the pressure was kept at 8 Torr throughout the nanowire synthesis. The tube furnace was naturally cooled down to room temperature in three hours. A white-yellowish layer was then obtained on the ITO substrate.

Synthesis of ZnO/ZnSe nanowire array

The as-synthesized ZnO nanowire array taken as a template was then transferred to PLD chamber for ZnSe coating**.** The neodymium-doped yttrium aluminum garnet (Nd:YAG) laser was used to ablate the ZnSe disc target. The laser wavelength, energy density, and pulse frequency were 266 nm, 130 mJ/cm^{2}, and 2 Hz, respectively. The distance from the target to the TCO substrate with ZnO nanowire array was 5 cm. Before the deposition, the vacuum system was first evacuated to 1x 10^{-3} Torr. After the deposition performed at 400 ^{o}C for 20 min, the sample was annealed at 500 ^{o}C for 1 h. The room-temperature PLD for ZnSe shell coating was also performed in the same system at 27 ^{o}C for 20min without any further annealing.

Device fabrication

To fabricate the device for photo-response measurement, Au interdigital electrodes were first defined by e-beam lithography on n-type degenerately doped silicon substrates with 600 nm thermal oxide layer. The ZnO/ZnSe core-shell nanowires were scratched from the TCO substrate and spread into IPA by ultrasonic. The nanowire solution was dispensed onto silicon substrate by spin coating at 200 rpm. By using solution with proper nanowire concentration, we can identify individual nanowires lying across two interdigital electrodes. The leads are added to the electrodes at locations away from the nanowire/electrode contacts.

Characterization and Measurements

A Philips X'Pert-MPD X-ray diffractometer (XRD), a Carl Zeiss 1530 VP field emission scanning electron microscope (FESEM), and a FEI Tecnai F20-UT high-resolution transmission electron microscope equipped with a nanoprobe energy-disperse x-ray spectroscope (EDS) were used to characterize structure, morphologies, and compositions of the nanowires. The transmittance measurements were performed on a Gary 5G UV-VIS-NIR Spectrophotometer with an integrating sphere (Labsphere DRA-CA-50), and thus the reflection and scattering loss were corrected. The nanowires were scraped off the substrates carefully with a blade, dispersed in a diluted toluene solution of ethylene-vinyl acetate copolymer (Elvax 150 or EVX, DuPont), then pipetted onto a microslide and air-dried. A blank control was also prepared for reference. PL measurements were carried out at room temperature by using a setup consisting of a SPEX 1403 0.85m double-grating spectrometer, cooled RCA C31034 GaAs photomultiplier tube. The 325 nm line (~5 mW) of a He-Cd laser was used for excitation, 50 μm slits were used. Raman measurements were performed on the same setup but a 532 nm laser with ~ 100 mW power was used instead, and 300 μm slits were used. The photo-response measurement was performed on a general purpose broadband spectroscopy system consisting of a 100 W tungsten lamp, ISA Triax Series 320 spectrometer, Stanford Research Systems SR570 current-preamplifier and SR30DSP lock-in amplifier. The spectra have been calibrated against a reference Si solar cell with a known quantum efficiency curve and for the ratio of the light spot size (~2x4 mm^2) to the nanowire cross-section (~8 μm length × 110 nm diameter). The sensitivity of the measurement system is ~ 0.5 pA.

3.2.2 Structures analysis of ZnO/ZnSe core-shell nanowire

Two step synthetic procedures have been used to fabricate the ZnO/ZnSe core-shell nanowire array. First, a large area (10×20 mm) well aligned ZnO nanowire array, serving as the core for further deposition of the ZnSe shell, was synthesized directly on a TCO substrate using CVD. The experimental set-up is similar to that of our previous work[26]. Subsequently, the TCO substrate with ZnO nanowire array was transferred into the hot-wall PLD chamber to perform the pulsed laser deposition of ZnSe. In order to investigate the influence of deposition temperature on the crystallization of the ZnSe shell, a room temperature PLD for ZnSe shell coating was also performed. In the PLD process, the thickness of the shell could be controlled by the target-to-substrate distance, deposition duration, pulse repetition frequency, and laser energy density.

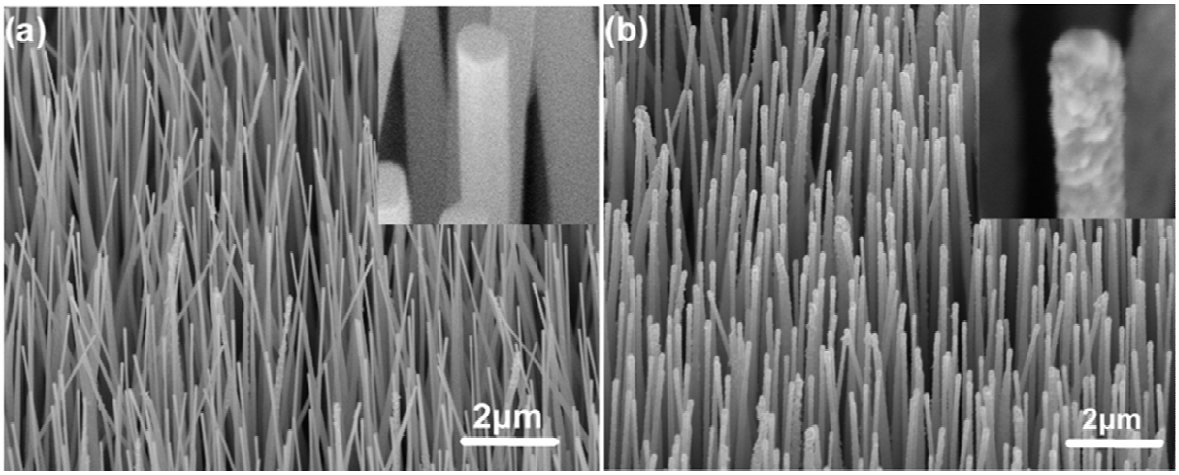

Figure 3.2 (a) SEM image of a well-aligned ZnO nanowire array grown on TCO substrate by CVD. The average length of the nanowires is about 10 μm and the diameters are about 100 nm. (b) SEM image of well-aligned ZnO/ZnSe Core-shell nanowire array prepared by PLD. The insets in (a) and (b) are enlarged images of ZnO nanowire and Core-shell nanowire tips, respectively.

Figure 3.2(a) shows a typical scanning electron microscopy (SEM) image of an as-synthesized ZnO nanowire array, presenting a uniform perpendicular growth of ZnO nanowires on the TCO substrate with an average length of 10 μm and diameters of 80 ~120 nm. After the PLD deposition and followed annealing, the final nanowires, as shown in Figure 2(b), exhibit

increased wire diameters and rough surfaces, indicating that ZnSe was successfully deposited on the ZnO nanowires. The insets in Figure 3.2 (a) and (b) are enlarged images of ZnO nanowire and core-shell nanowire tips, respectively.

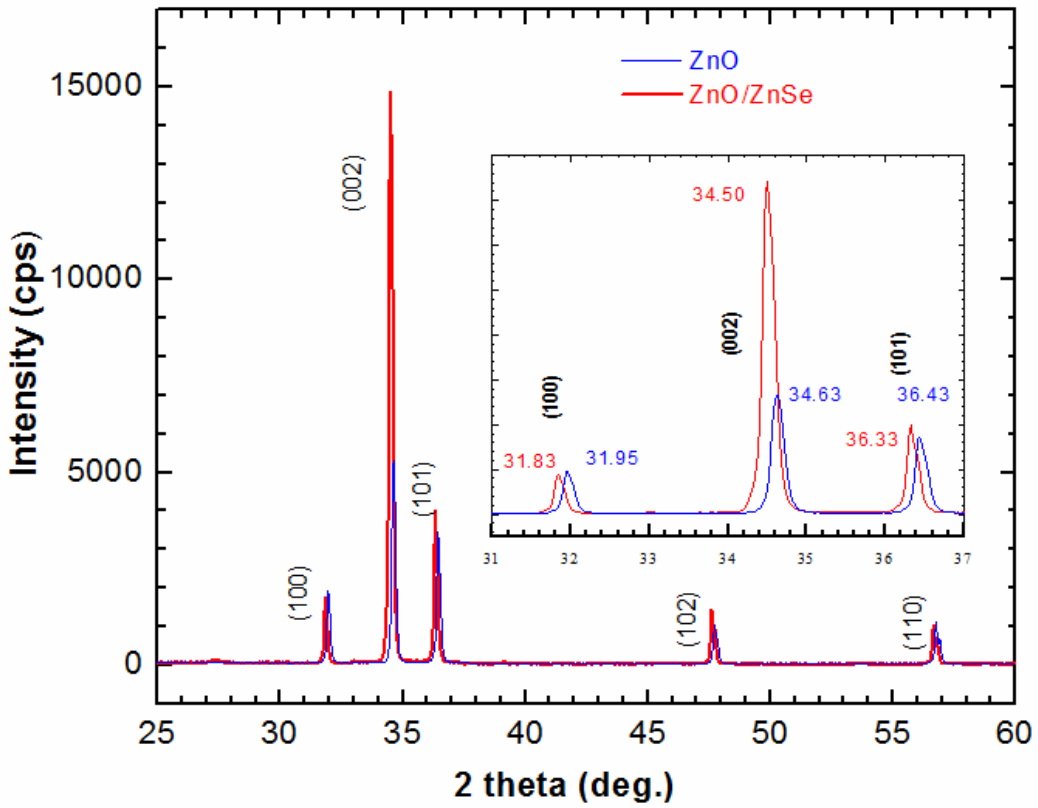

Figure 3.3 XRD patterns of ZnO and ZnO/ZnSe nanowire arrays. The inset shows clear peak shifting of ZnO/ZnSe to low angle region.

XRD pattern of ZnO nanowire array and ZnO/ZnSe nanowire array are shown in Figure 3.3. The predominant ZnO peak from (002) planes indicates that the ZnO nanowires were grown with a *c*-axis orientation normal to the substrate surface. No characteristic diffraction peak of ZnSe was observed in XRD pattern of ZnO/ZnSe nanowire array because of the thin ZnSe layer. By comparing the positions of three ZnO peaks (100), (002), and (101) of wurtzite phase, all peaks slightly shifted to low angle region after being coated with the ZnSe layer, which suggests that

the ZnO lattice was enlarged. The shift might be attributed to the lattice expansion because of the ZnSe shell growth, which will be elaborated later.

Detailed microstructures of the coated nanowires were further investigated using field emission transmission electron microscope (TEM) equipped with an X-ray energy dispersive spectroscopy (EDS). Figure 3.4(a) shows a low magnification TEM image of a ZnO/ZnSe core-shell nanowire with a rough external surface, but a sharp interface between the core and shell. The ZnSe shell grows directly in the radial direction from the surface of ZnO nanowire with a thickness of 5~8 nm. A high resolution TEM image taken from the interface region between the ZnO core and ZnSe shell (specified in rectangular area in Figure 3.4(a)), as shown in Figure 3.4(b), reveals that ZnO and ZnSe are of wurtzite (WZ) and zinc blende (ZB) crystal structures, respectively. At the interface, an epitaxial growth of ZnSe from ZnO core is observed. The interface is smooth and no transitional layer is found in between. The axis of the ZnO nanowire is identified to be the WZ *c*-axis. The epitaxial growth relationship of the WZ ZnO core and ZB ZnSe shell has been identified as $[0001]_{ZnO}$ // $[001]_{ZnSe}$ and $(2\bar{1}\bar{1}0)_{ZnO}$ // $(011)_{ZnSe.}$ Figure 3.4 (c) and (d) are the fast Fourier transform (FFT) patterns of ZnO core and ZnSe shell, indexed as WZ and ZB structure with zone axis of $[2\bar{1}\bar{1}0]$ and [011], respectively, which also confirms the above epitaxial growth relationship.

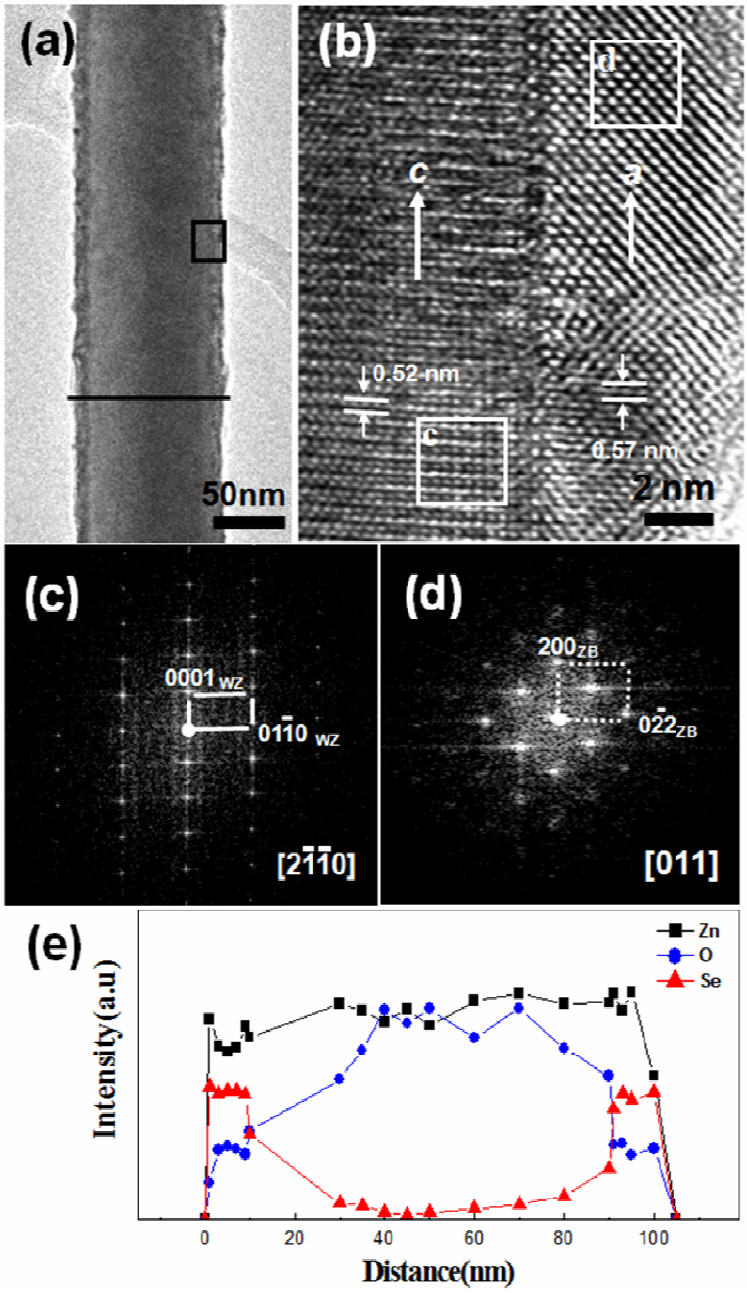

Figure.3.4 Low magnification TEM micrograph of a ZnO/ZnSe Core-shell nanowire. A thin layer of ZnSe was coated on the ZnO nanowire. b) High resolution TEM image of the interface of the Core-shell heterostructure, enlarged from the rectangular area in (a), showing the epitaxial growth relationship of ZnO wurtzite core and ZnSe zinc blende shell. c) and d) Fast Fourier transfer (FFT) patterns of rectangular areas in (b). e) EDS nanoprobe line-scan on elements Zn, Se, and O, across the ZnO/ZnSe Core-shell nanowire, indicated by a line shown in (a).

Defects were also observed in the interface along the *c*-axis of ZnO due to the large lattice mismatch, 8.8% along the nanowire axis between *c*=0.521nm for ZnO and *a*=0.567nm for ZnSe. Note that the lattice mismatch along the nanowire axis would be much larger (~ 25%) if ZnO and ZnSe were both in the WZ phase. The spatial distributions of the atomic composition across the ZnO/ZnSe core-shell nanowire were obtained by a nanoprobe EDS line-scan analysis (marked by a line in Figure 3.4(a)), showing the ZnO nanowire was homogeneously coated, as shown in Figure 3.4(e).

It is also found that epitaxial growth only occurred during high temperature deposition and

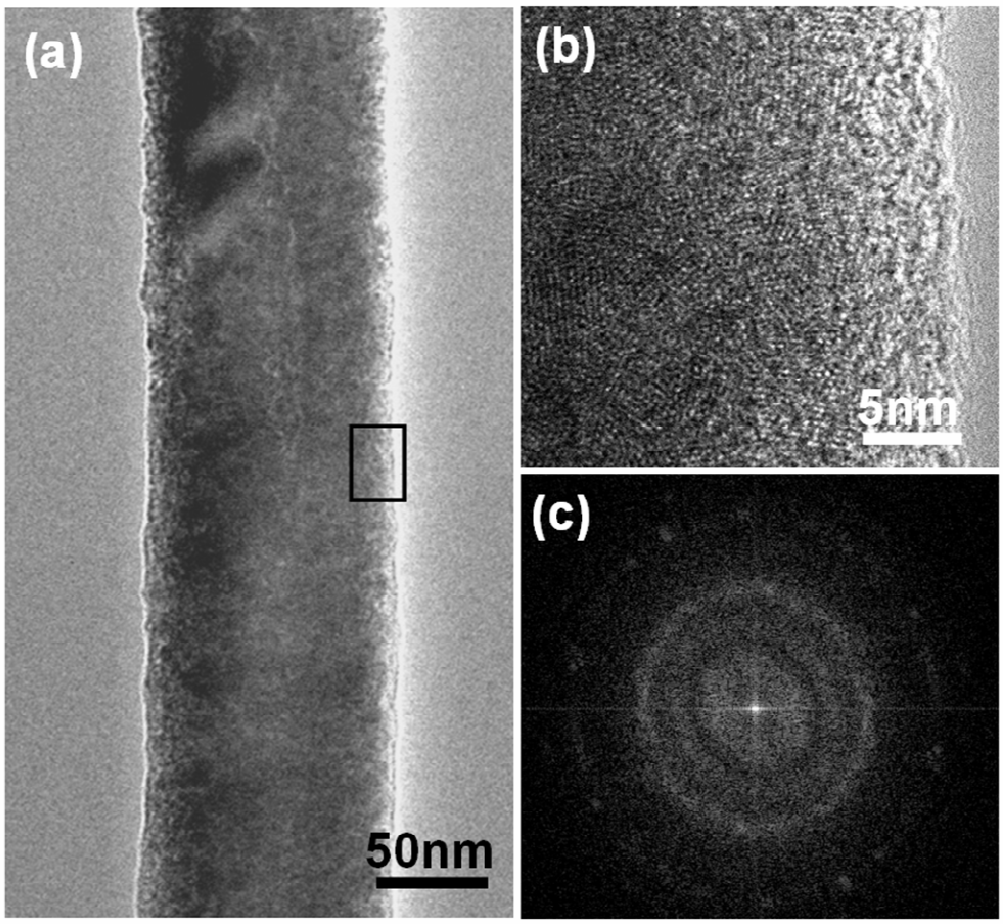

Figure.3.5 TEM images of room temperature PLD deposited ZnSe shell on ZnO nanowire. (a) Low-magnification TEM image. (b) High resolution image enlarged from rectangular area in (a). (c) Corresponding fast Fourier transformation (FFT) pattern, indicating the ZnSe shell is polycrystalline without epitaxial growth.

no epitaxial growth was found at room temperature deposition (shown in Figure 3.5), indicating the epitaxial growth between ZnO and ZnSe demands favorable thermodynamic as well as kinetic conditions. In the case of deposition performed at room temperature, the initial deposit atoms, without gaining enough migrating energy from the system, condense at the very site they arrive at the surface of ZnO and then aggregate with the following deposit atoms, forming a thick layer of polycrystalline ZnSe.

3.2.3 Optical properties of ZnO/ZnSe

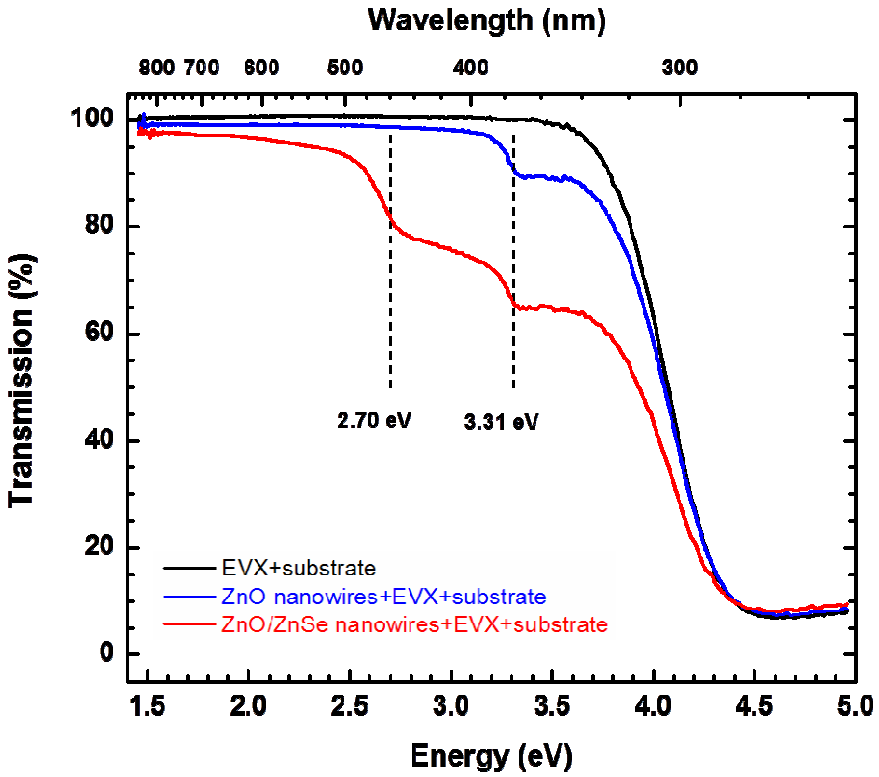

Figure 3.6. Transmission spectra of ZnO nanowires and corresponding ZnO/ZnSe core-shell nanowires. Two vertical lines indicate the excitonic bandgap of bulk ZnO and ZnSe, respectively.

The optical properties of the ZnO/ZnSe core-shell nanowire were investigated by transmission, photoluminescence, Raman, and photo-response measurements. Figure 3.6 shows the typical transmission spectra of bare ZnO nanowires and ZnO/ZnSe core-shell nanowires. For the latter, two excitonic absorption peaks are clearly observed at respective excitonic bandgaps (3.31 eV for WZ ZnO and 2.70 eV for ZB ZnSe), indicating good crystallinity of both core and

shell. Similar to the cases of type II core-shell nanocrystals,[27,28] and additional absorption is found extending below the ZnSe bandgap into near infrared. The component below the ZnSe bandgap could arise from spatially indirect or interfacial transition coupling a hole state in the ZnSe shell with an electron state in the ZnO core.

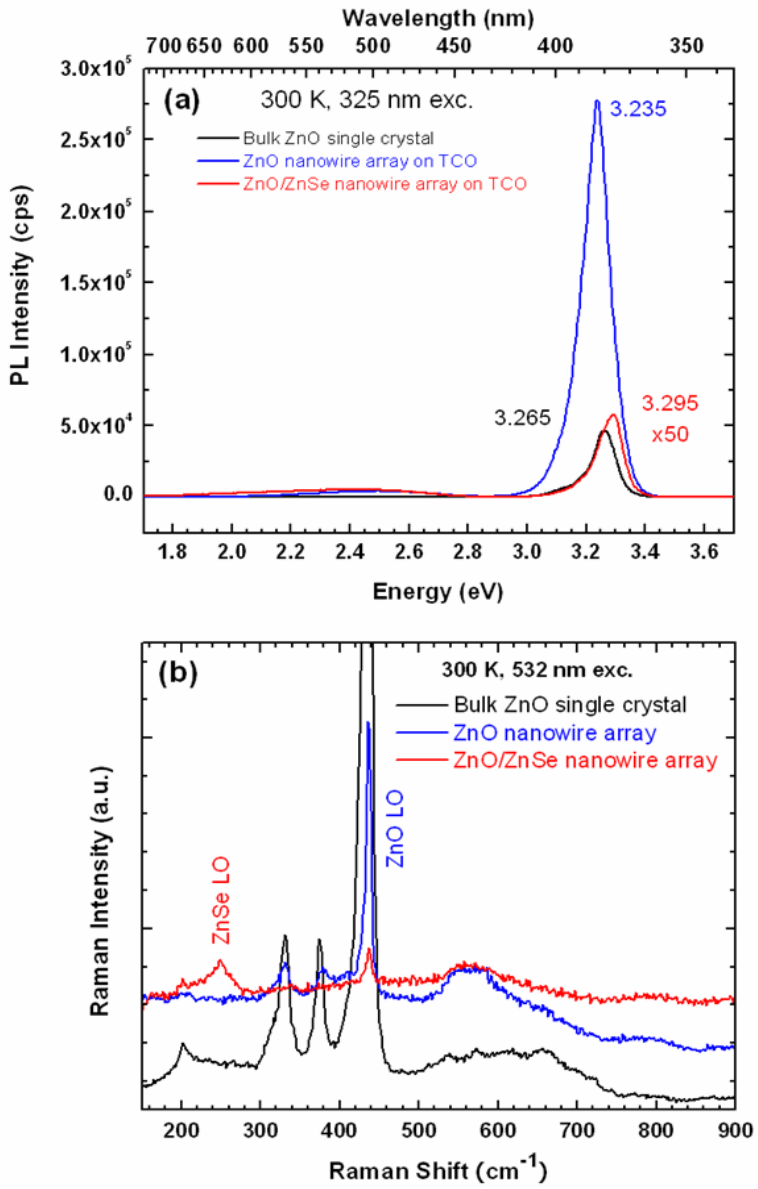

Figure 3.7. (a) Photoluminescence and (b) Raman spectra of ZnO and ZnO/ZnSe nanowire arrays, compared with those of a bulk single crystal ZnO.

Figure 3.7(a) shows the PL spectra of ZnO, ZnO/ZnSe core-shell nanowires, compared with the spectrum of a high quality bulk *c*-plane ZnO single crystal purchased from Tokyo Denpa, Ltd. The reference sample shows bright emission visible to the naked eyes at the excitation of ~ 5mW 325 nm laser, with its bandgap excitonic emission at 3.265 eV and a weak defect-related emission band at ~2.4 eV of ~ 0.5% of the band edge peak. Despite without any intentional surface passivation effort, for the bare ZnO nanowire array, the PL peak (at 3.235 eV) near the band edge of ZnO is found to be surprisingly very strong, even exceeding that of the ZnO single crystal reference (that shows the strongest band edge emission among the several bulk ZnO samples tested) under the nominally same measurement conditions. Additionally, the ZnO nanowire array also shows a weak visible emission band (at ~2.49 eV, ~1.5% of the band edge peak). On one hand, the high PL intensity indicates the high interior crystal quality of the nanowires; on the other hand, two photonic crystal related effects might contribute to the high external quantum efficiency: (1) the waveguide effect of the nanowire eliminates the lateral propagation[27], and (2) a smaller effective dielectric constant of the array, as a result of averaging between the ZnO and air, than the bulk ZnO facilitates the escaping of light from the sample. However, it is a puzzle that the large surface area of the nanowires, thus the expected large number of surface defects, does not seem to cause a detrimental effect on the carrier recombination. For the core-shell nanowire array, the band edge emission remains strong but shifted to 3.295 eV, although reduced by roughly a factor of 300 from that of the bare ZnO nanowire array or ~ 50 from that of the bulk ZnO reference. There could be several possible reasons for the reduction: (1) the charge separation between the core and shell (namely the hole relaxes into the shell but the electron remains in the core), (2) non-radiative recombination at the possible defect sites of the core-shell interface, and (3) the absorption of the shell to the excitation and emission photons. Although the ZnSe shell is relatively thin and the absorption of a single path is relatively small (~5% per 10 nm), the multiple scattering in the nanowire array could significantly increase the absorption. Further investigation on the carrier dynamics associated with the core-shell interface and growth optimization are definitely needed, but we could at least conclude that the interface defects are not as detrimental as one might expect for such highly mismatched heterostructure. No clearly identifiable emission is found from the shell, which is understandable giving the fact that the bandgap energy of the ZnSe shell overlaps with that of the defect band of the ZnO, thus, the ZnSe emission, if any, will be obscured, and also the

ZnSe shell is relatively thin. However, for the core-shell nanowire array, a Raman peak of ZnSe LO phonon at 248 cm^{-1}, as shown in Figure 3.7(b), is observed in addition to the Raman features of ZnO (e.g., E_2 mode at 438 cm^{-1}), indicating the ZnSe shell is of crystalline or polycrystalline phase.

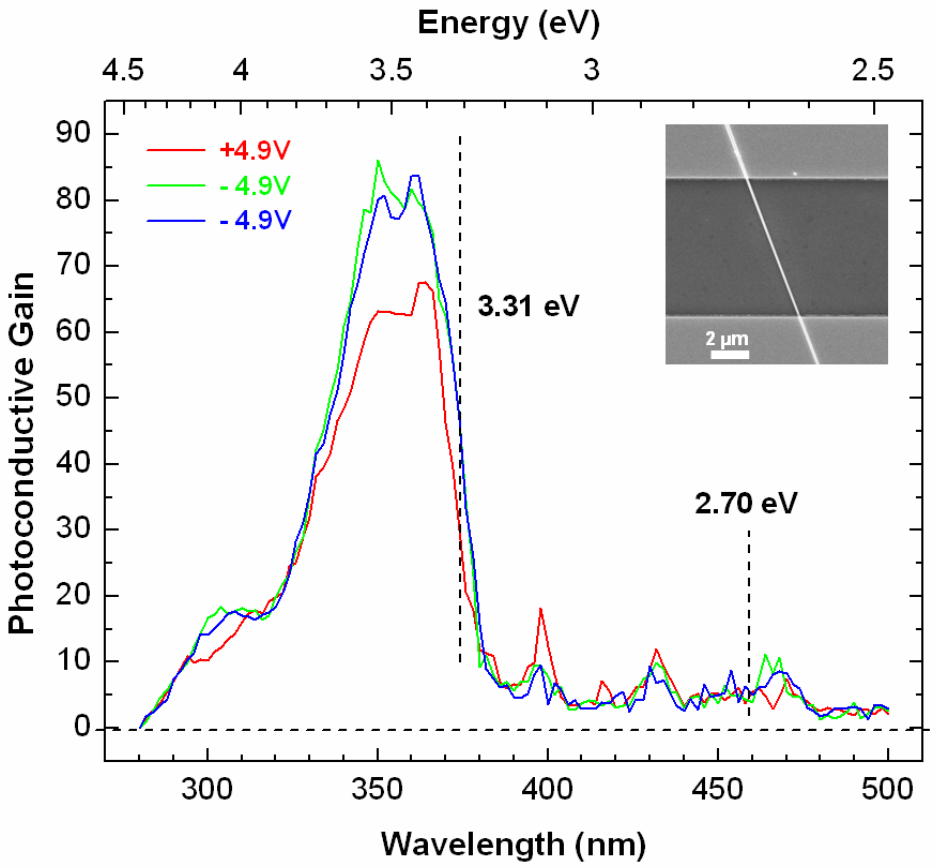

Figure 3.8. Photo-conductivity spectra for a single ZnO/ZnSe nanowire measured under different biases and at different days. The inset shows the SEM picture of the single-nanowire device for photo-response measurements.

3.2.4 Photoresponse

Photo-response measurements were performed on a very preliminary device: a single core-shell nanowire sitting on two Au electrodes at the two ends. Since the contacts are symmetric, the device is not expected to function as a single nanowire solar cell[13], and a bias is needed to generate the photo-current. Figure 3.8 shows the photo-response spectra under positive and

negative bias (switching the polarity of the bias voltage). A standard procedure for solar cell quantum efficiency measurement was followed, but with a bias, thus, the result should be considered as photo-conductivity gain. Despite the photo-current being rather small (a few pA maximum), and the gain being significantly smaller than what has been reported previously for pure ZnO nanowires with more robust contacts[29], the result is repeatable, stable, and perhaps more significantly the response shows an extension to the wavelength region below that of ZnO bandgap. The existence of the photo-conductivity in the ZnSe spectral region indicates that the carriers are not fully depleted by either defects at the ZnO/ZnSe interface or the ZnSe surface, despite the ZnSe shell being fairly thin.

3.3 ZnO/ZnS core-shell nanowire array

3.3.1 Experimental

Synthesis of ZnO/ZnS core-shell nanowire

Briefly, vertically aligned ZnO nanowire arrays were grown on an ITO substrate at 600°C. A continuous ZnO seed layer formed before the actual growth of the nanowire, because of heating the zinc foil during the initial chemical vapor deposition process. This layer is in fact necessary for the PV device serving as a hole blocking layer. The nanowire array then served as a template for further ZnS coating by PLD. To facilitate possible epitaxial growth, the PLD was performed at 500^{o}C, which is a higher temperature than that used for synthesizing the ZnO/ZnSe core-shell structure last section. The ZnO seed layer also prevents the ZnS coating from contacting the ITO electrode.

Characterization

A Philips X'Pert-MPD X-ray diffractometer (XRD), a Carl Zeiss 1530 VP field-emission scanning electron microscope (SEM), and a FEI Tecnai F20-UT high-resolution transmission electron microscope (FETEM) equipped with a nanoprobe energy-dispersive X-ray spectroscope (EDS) were used to characterize structure, morphologies, and compositions of the nanowires. Photoluminescence (PL) measurements were carried out at room temperature using a setup

consisting of a SPEX 1403 0.85-m double-grating spectrometer, cooled RCA C31034 GaAs photomultiplier tube. The 325-nm line (~5 mW) of a He-Cd laser was used for excitation, and 100-µm slits were used. For Raman measurements, the slit width was increased to 400 µm.

3.3.2 Structures analysis of ZnO/ZnS core-shell nanowire

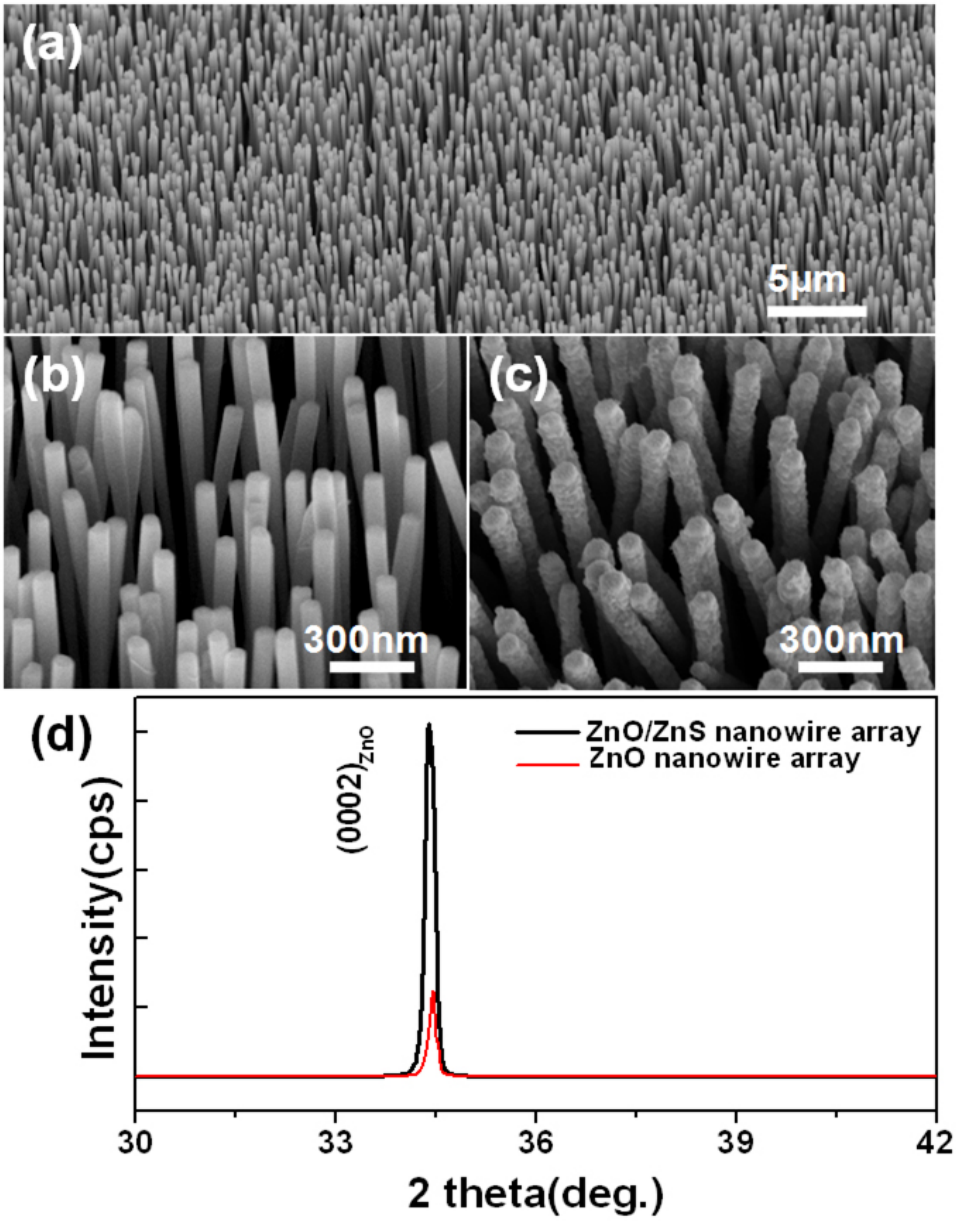

Figure 3.9 (a) Low-magnification SEM image of a well-aligned ZnO nanowire array grown on TCO substrate by chemical vapor deposition. The average length of the nanowires is about 7 µm and the diameters are about 50~120 nm. (b) and (c) Magnified SEM images of bare ZnO and ZnO/ZnS Core-shell nanowire arrays, respectively. (d) XRD patterns of ZnO and ZnO/ZnS nanowire arrays.

Figure 3.9(a) shows a typical low-magnification SEM image of an as-synthesized ZnO nanowire array, revealing perpendicular growth of ZnO nanowires on the ITO glass with an average length of ~7 μm and diameters in the range of 50~120 nm. Higher-magnification SEM images before and after the pulsed-laser deposition of ZnS are presented in Figures. 3.9(b) and (c), respectively. Compared to the bare ZnO nanowire, we found a noticeable increase in the diameter and rough surface for the ZnO/ZnS nanowires, which implies that ZnS is successfully deposited over the ZnO nanowire. XRD patterns of the bare and shelled ZnO nanowire array are shown in Figure 3.9(d). Only the strong hexagonal ZnO (0002) diffractive peak was observed in XRD patterns for the bare ZnO nanowire array, indicating strong preferred orientation along the *c* axis of wurtzite (WZ) ZnO. For the XRD pattern of the ZnO/ZnS nanowire array, the intensity of the (0002) peak from ZnO increases significantly because the PLD was performed at the relatively high temperature of 500°C; thus, the crystalline quality of the ZnO core was improved as a result of an annealing effect. No additional diffraction peak was observed in the pattern of ZnO/ZnS nanowires, perhaps because the ZnS layer is fairly thin. However, a slight position shift of the ZnO peak to a lower angle was observed for the ZnO/ZnS core-shell structure, which may indicate the presence of lattice distortion.

Figure 3.10(a) shows a typical low-magnification TEM image of a ZnO/ZnS core-shell nanowire. The sharp interface between the core and shell clearly shows that the ZnO nanowire is fully sheathed by a ZnS layer along the entire length. The ZnS layer is □12 nm thick and has a rough surface. Figure 3.10(b) is a high-resolution TEM image of the rectangular area b in Figure 3.10(a) that shows the detailed interface structure between the ZnO core and ZnS shell. Although lattice distortion (in ZnO) and stacking faults (in ZnS) can be observed along the interface, both the core and shell exhibit lattice fringes and can be further identified as WZ and zinc-blende (ZB) structures, respectively, thus indicating that the ZnS shell layer was successfully grown over the ZnO core. To achieve more precise information about the growth relationship, the magnified HRTEM image of the core and shell taken from rectangles c and d in Figure 3.10(a) and their corresponding fast Fourier transform (FFT) patterns are shown in Figures. 3.10(c) and (d). The marked inter-planar *d* spacings of 0.31 and 0.52 nm correspond, respectively, to the $(\bar{1}1\bar{1})$ lattice plane of ZB ZnS with the [011] zone axis and the (0001) lattice plane of WZ ZnO with the $[2\bar{1}\bar{1}0]$ zone axis. Thus, the core and shell are determined as epitaxial growth with the growth

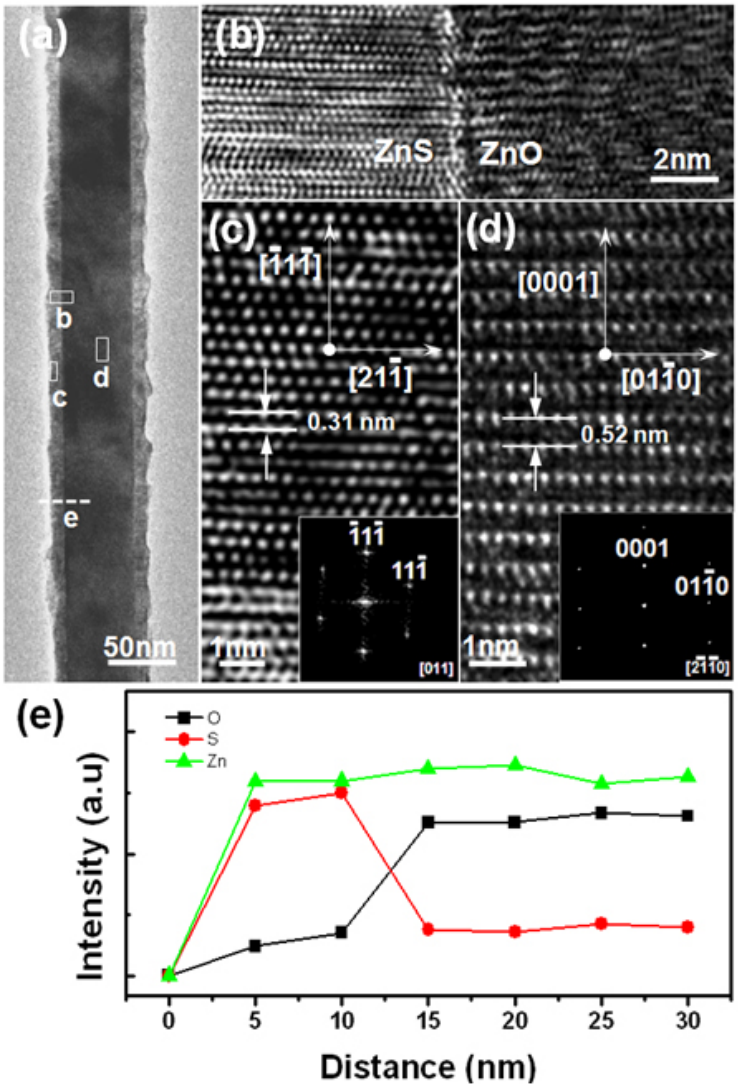

Figure 3.10 Structural characterization of ZnO/ZnS Core-shell nanowire array. (a) Low-magnification TEM micrograph of a ZnO/ZnS Core-shell nanowire, showing a thin layer of ZnS coated on the ZnO nanowire. (b) High-resolution TEM image of the interface of the Core-shell heterostructure, enlarged from the rectangular area in (a), showing the epitaxial growth relationship of ZnO wurtzite core and ZnS zinc-blende shell. (c) and (d) Atomic resolution images of the core and shell areas taken from the rectangular areas in (a), respectively. The insets in (c) and (d) represent the corresponding fast Fourier transfer patterns. (e) EDS nanoprobe line-scan across the Core-shell interface.

relationship of $[0001]_{ZnO}//[\bar{1}1\bar{1}]_{ZnS}$ and $[01\bar{1}0]_{ZnO}//[21\bar{1}]_{ZnS}$, in contrast to that for the previously studied ZnO/ZnSe system, where $[0001]_{ZnO}//[001]_{ZnSe}$ was observed[17]. As shown in Figure.

3.10(e), EDS data scanned along the line labeled as "e" in Figure 3(a) reveal the spatial distribution of Zn, O, and S across the core-shell interface, further confirming that the ZnS was deposited homogeneously over the ZnO and formed the core-shell structure.

The epitaxial growth of WZ ZnS and ZnO has been reported in many nanoheterostructures in the planar form even though a large mismatch (~20%) exists[31-33]. In our case, though the lattice mismatch between the WZ ZnO and ZB ZnS is still fairly large (~19%), it appears that various factors, including perhaps the geometry of the "substrate" (the ZnO nanowire), size of the core, growth temperature, and non-thermal equilibrium condition, play roles in successfully growing such a epitaxial core-shell heterostructure that is unlikely to be feasible in the planar form. However, due to the large lattice mismatch, the structure defects, such as stacking faults and lattice distortion as shown in Figure 3.10 (b), inevitably exist in order to release strain energy when the shell layer grows thicker. Furthermore, the formation of the rough external surface of ZnS shell could be understood as a transition from the initial cylindrical growth to the island growth in core-shell nanowire system[34].

3.3.3 Optical properties of ZnO/ZnS

The optical properties of the ZnO/ZnS core-shell nanowire were investigated by PL spectrum and resonant Raman scattering. Figure 3.11 shows the PL spectra of ZnO and ZnO/ZnS nanowire arrays measured at room temperature. The PL spectrum of the bare ZnO nanowire array consists of two emission peaks at 3.228 and 2.450 eV. Although close to the bandgap, the higher energy peak is still likely defect- or impurity-related, because for high-quality bulk ZnO, the room-temperature emission peak has been found at somewhat higher energy, for instance, 3.265 eV.[30] The lower energy peak is obviously non-intrinsic and is often believed to be associated with oxygen-vacancy [35]or surface-related states[36], although the exact origin of this transition remains unclear. Compared with the bare ZnO nanowire array, the peak position of the UV emission in ZnO/ZnS sample shows a small blue shift, and the intensity is reduced by a factor of 63. The intensity of the visible peak is also reduced, but to a much lesser extent (by ~30%). Qualitatively, the effect of a ZnS coating is similar to that of a ZnSe coating reported previously[30]. It was recently reported that a ZnS coating over ZnO nanotubes or nanorods enhanced UV emission [37,38] , which appears to agree with conventional wisdom that the coating

of a large-bandgap material diminishes the loss through surface recombination and the UV emission is from the bulk part of ZnO. However, this understanding is not expected to hold true for the type II combination such as ZnO/ZnS, even though ZnS has a larger bandgap. In principle, one should expect that the charge-separation effect should quench, instead of enhance, the PL signal, because the type II core-shell structure should result in depleting the holes in the ZnO core. However, if this mechanism were indeed responsible for the observed quenching of the UV emission in our core-shell structure we should have seen the quenching of both UV and visible emission in a similar degree, which should also hold true if the coating introduces nonradiative defect centers at the heterojunction interface. That the reduction is relatively small for the visible peak and much more significant for the UV peak may suggest that the visible emission could be from the volume of the ZnO nanowire, whereas the UV emission could be surface related and thus more sensitive to the coating that has modified the electronic structure of the bare ZnO nanowire surface, either by introducing nonradiative centers or inducing the transfer of holes to the ZnS shell from the surface bound excitons.

Resonant Raman features with up to fifth-order longitudinal optical (LO) phonons were observed in the same PL measurement in the ZnO/ZnS nanowire array. The spectrum is included

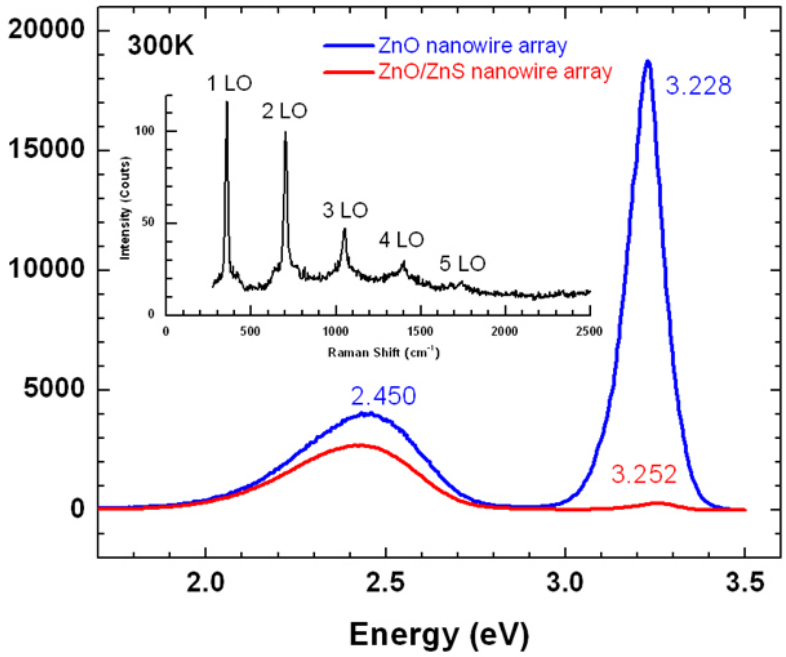

Figure 3.11 Room-temperature photoluminescence spectra of ZnO and ZnO/ZnS Core-shell nanowire arrays. Inset shows the resonant Raman features of ZnS shell.

in Figure 3.11. Following the observation of the resonant Raman features in bulk ZnS crystal,[39] such features have also been reported for ZnS hollow microspheres.[40] The observation of the multiple orders of resonant Raman features may indicate the good crystalline quality of the material. The LO phonon energy is 347 cm^{-1}, which is close to the room-temperature value recently reported in the literature (348 cm^{-1}) [40].

3.3.4 Photovoltaic performance of ZnO/ZnS nanowire array

The architecture of the type II PV device, schematically shown in Figure 3.12(a), employs the ZnO/ZnS core-shell nanowire array as the active layer and carrier transport medium, using ITO and gold as the anode and cathode, respectively. The cell is illuminated from the bottom.Figure3.12 (b) illustrates the key steps of photo-carrier generation, charge separation, and transportation. Ideally, once the incident photon with energy greater than the bandgap of the type

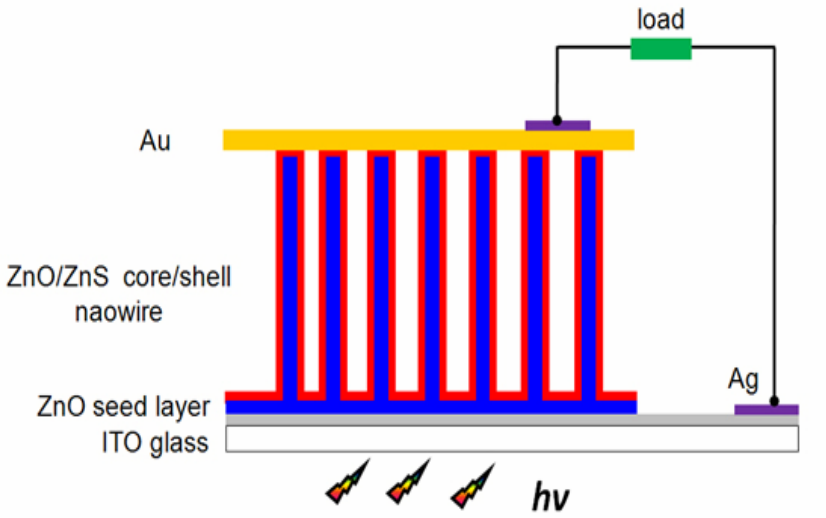

Figure 3.12. Schematic diagram showing the strategy to develop a PV device using a type II core-shell nanowire array. An array of ZnO/ZnS nanowires, vertically aligned on an ITO glass substrate, serves as the active layer and the transport medium. A gold layer is sputtered on the tips of the nanowire array, contacting the ZnS shell, as the top electrode and the cell is illuminated from the bottom.

II herterojunction is absorbed, the photoexcited electron-hole pair will be generated and

immediately separated into the ZnO core and ZnS shell due to the quasi-electric field near the interface. The ZnO nanowire cores and ZnS shells then serve as the transport channels to deliver the carriers to the counter electrodes.

PV devices were fabricated using a cover-etch-deposit approach, similar to the process for fabricating the *p*-GaN/*n*-Si nanowire array PV device[41]. The air space of the ZnO/ZnS nanowire array was first filled with photoresist (Shipley 1813) by spin coating, followed by several-second acetone etching to expose the tips of the nanowires. For fabricating electrodes, a gold layer 50 nm thick was sputtered onto the exposed nanowire tips to form the top electrode (Figure 3.13(a)), and the bottom (ITO) electrode was exposed by removing the ZnO nanowire near the edge of the substrate via diluted hydrochloride (10%). Finally, the photoresist was removed by dipping in acetone for several seconds. To maintain the same active area, the top gold electrodes of the devices were sputtered using the same mask. The cross-section of the final device was shown in Figure 3.13(b).

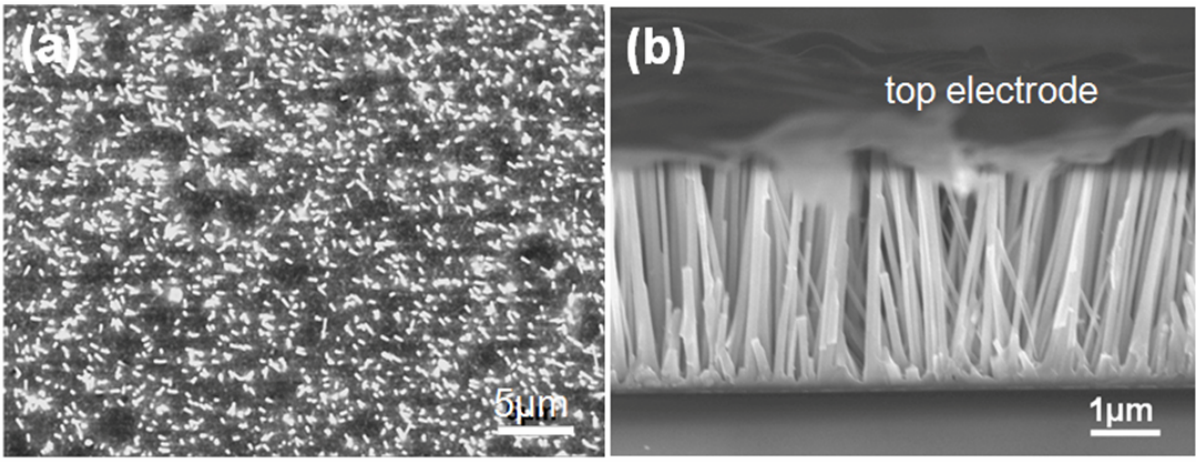

Figure.3.13 (a) Top-view of the nanowire array embedded in photoresist after etching. (b)Cross-section of photovoltaic device based on a ZnO/ZnS core-shell nanowire array.

The solar cell performance was tested using a home-made solar cell testing station, at 25^{o}C and under the illumination of a Xe lamp. The light intensity corresponding to 1 sun AM1.5G illumination was calibrated using a Si photodiode. The *I-V* curves were measured using a Keithley 238 current source measurement unit. The time-dependent photocurrent was first measured without external bias, as shown in Figure 3.14(a).

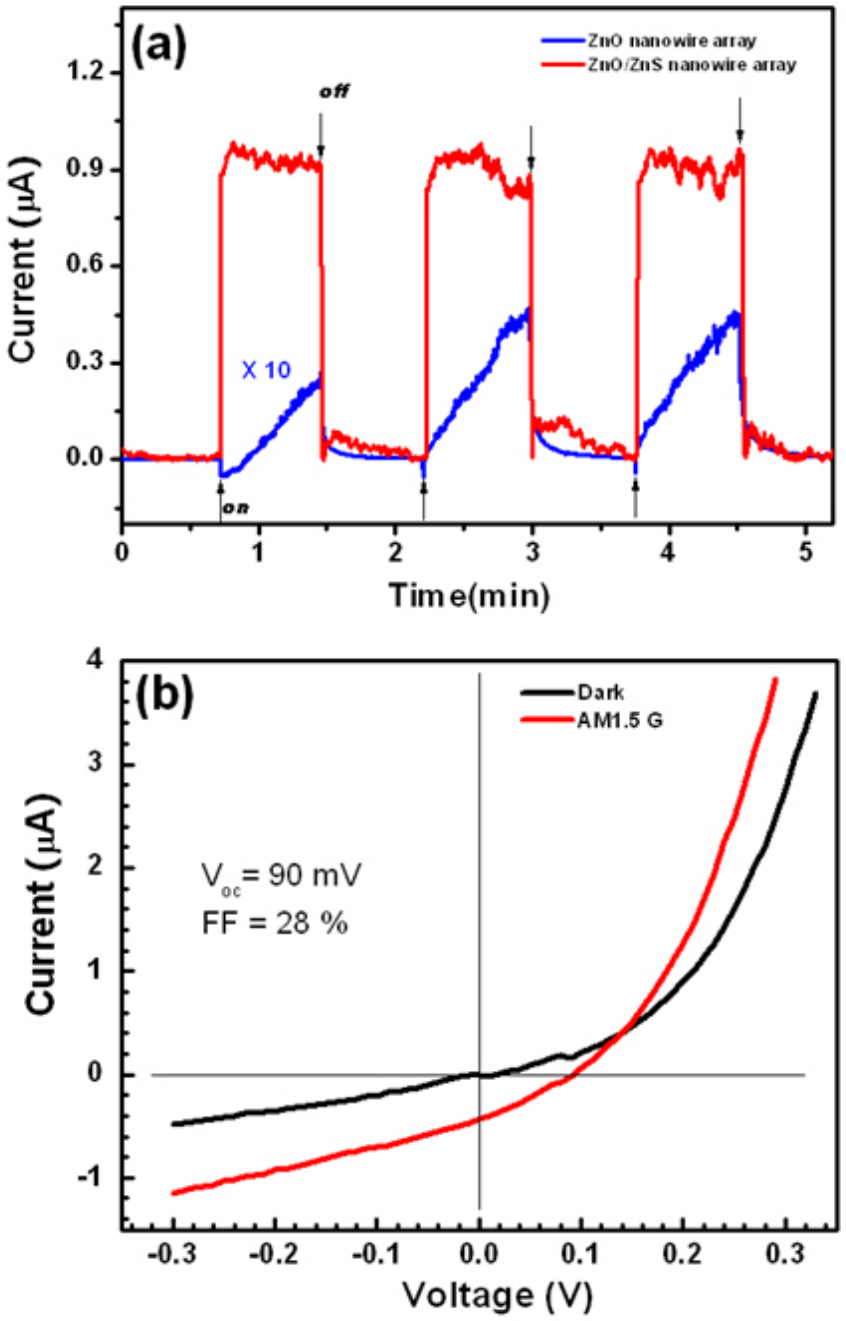

Figure 3.14 (a) Time-dependent photocurrent of bare ZnO and ZnO/ZnS core-shell nanowire arrays without external bias. (b) Current *(I) vs* voltage *(V)* for the solar cell in the dark and under simulated AM1.5G illumination with intensity of 1000 W/m^2, showing the PV effect.

The photocurrent responded (rise/decay) instantly as the incident light was turned on/off. Although the photocurrent increase was also observed in the device composed of a bare ZnO nanowire array, the signal was about 30 times weaker for the same device size that was determined by the contacted area. Moreover, the photoresponse observed in the ZnO device was slower than that in the ZnO/ZnS device, which may be attributed mainly to a heating effect or surface-related absorbates (O_2^-)[42]. The enhanced photocurrent and faster response observed in ZnO/ZnS, despite of the quenching of the UV emission, could indicate the realization of the key feature of the type II heterostructure – the charge separation, although we cannot exclude other possibilities (such as the ZnS/Au contact is different from ZnO/Au). However, because of the large thickness of the nanowire layer, the light absorption occurs mostly in the bulk part of the ZnO nanowire core, the core-shell interface has to serve the function of separating the electrons and holes.

Figure 3.14(b) shows the current-voltage *(I-V)* curve of the device under an illumination of 1,000 W/m^2. The open-circuit voltage V*oc* is 0.09 V, with a fill factor FF of 0.28. The energy efficiency could not be given because of the uncertainty of the actual device area. The primary reason is that a significant number of nanowires might not actually be connected to the electrodes, because of two factors: i) some ZnO nanowires might break off from the seed layer during the device fabrication process; ii) the ZnO nanowires vary slightly in length, resulting in that some of them remained covered by photoresist after chemical etching before top electrode deposition. Therefore, the current density was inaccurate if simply using the area defined by the electrode. However, the open circuit voltage V*oc* should not be affected by the area. Although the device performance is far from satisfactory, this prototype device demonstrated the feasibility of fabricating a core-shell nanowire solar cell based on the type II heterostructure and a whole array of such devices. Several possible reasons exist for the low performance, including: (1) defect formation at the heterostructure interface, (2) quality of the shell material, and (3) quality of the top contact (between the ZnS shell and cathode). We note that because of the relatively large core nanowire size and the large bandgaps for both materials, this particular device cannot be expected to deliver a high energy efficiency, even in the ideal situation. The large core size means no bandgap tuning expected in the true quantum region where the bandgap of the new structure could be significantly smaller than those of the two components. Also, the large core size means more recombination loss in the bulk part of ZnO nanowire, before the carrier can

reach the interface. Furthermore, the crystalline quality of the shell depends on the core size and curvature, and in general a small core size leads to a stable shell growth. Further investigation will address these issues and will explore other material combinations that form type II heterojunctions, but with less lattice mismatch and smaller bandgaps.

3.4 Conclusion

In summary, large area well aligned air-stable ZnO/ZnSe and ZnO/ZnS core-shell nanowire array was fabricated directly on TCO substrate by combining CVD and PLD techniques and their structures and optical properties were investigated in detail. For ZnO/ZnSe core-shell nanowire array, SEM and TEM studies revealed that the ZnO nanowire were uniformly and perpendicularly grown on the TCO substrate and the ZnSe shell with a thickness of 5-8 nm were epitaxially grown on the ZnO nanowires core. Absorption and photo-conductivity studies show an extension of photo-response into the region well below ZnO bandgap. Such a core-shell nanowire array represents a novel architecture that could lead to a stable and efficient as well as low-cost solar cell technology for solar energy harvesting. In fact, our successful synthesis of directly grown ZnO/ZnSe core-shell nanowire array on TCO, implying the potential Type-II heterojunction PV devices, has inspired a series of research activities on ZnO/ZnSe nanowires system[43-48]. Noticeably, recent studies further revealed the threshold of the photo-response is found to be at around 1.6 eV, which corresponds to an efficiency limit of 29% under one-sun,and a large open circuit voltage of 0.7 V[47].

For ZnO/ZnS core-shell nanowire array, HRTEM study revealed another unusual epitaxial relationship of the heterostructure of two crystalline phases, ZnO-(0001)/ZnS-(111), which shows very intriguing growth phenomena for the future study in nanoheterostructure growth. A type II heterojunction-based PV device using a ZnO/ZnS nanowire array as the active material was fabricated. Although the device performance is far from satisfactory at current stage of development, the PV device demonstrated here would expand the opportunities for designing and optimizing nanoscale PV and other optoelectronic devices beyond the conventional *p-n* junction approach.

Reference

1 M. Gratzel, Nature **414**, 338 (2001)
2 I. Robel, V. Subramanian, M. Kuno, and P. V. Kamat, Journal of the American Chemical Society **128**, 2385 (2006)
3 P. R. Yu, K. Zhu, A. G. Norman, S. Ferrere, A. J. Frank, and A. J. Nozik, Journal of Physical Chemistry B **110**, 25451 (2006)
4 W. U. Huynh, J. J. Dittmer, and A. P. Alivisatos, Science **295**, 2425 (2002)
5 I. Gur, N. A. Fromer, M. L. Geier, and A. P. Alivisatos, Science **310**, 462 (2005)
6 M. Adachi, Y. Murata, J. Takao, J. T. Jiu, M. Sakamoto, and F. M. Wang, J. Am. Chem. Soc. **126**, 14943 (2004)
7 J. B. Baxter and E. S. Aydil, Appl. Phys. Lett. **86**, (2005)
8 M. Law, L. E. Greene, J. C. Johnson, R. Saykally, and P. D. Yang, Nature Materials **4**, 455 (2005)
9 Y. M. Kang, N. G. Park, and D. Kim, Appl. Phys. Lett. **86**, (2005)
10 Y. Zhang, L.-W. Wang, and A. Mascarenhas, Nano Lett. (USA) **7**, 1264 (2007)
11 J. Schrier, D. O. Demchenko, and L. W. Wang, Nano Lett. (USA) **7**, 2377 (2007)
12 B. M. Kayes, H. A. Atwater, and N. S. Lewis, Journal of Applied Physics **97**, (2005)
13 B. Z. Tian, X. L. Zheng, T. J. Kempa, Y. Fang, N. F. Yu, G. H. Yu, J. L. Huang, and C. M. Lieber, Nature **449**, 885 (2007)
14 S. Kim, B. Fisher, H. J. Eisler, and M. Bawendi, J. Am. Chem. Soc. **125**, 11466 (2003)
15 B. M. Kayes, H. A. Atwater, and N. S. Lewis, J. Appl. Phys. **97**, 114302 (2005)
16 B. Tian, X. Zheng, T. J. Kempa, Y. Fang, N. Yu, G. Yu, J. Huang, and C. M. Lieber, Nature **449**, 885 (2007)
17 K. S. Leschkies, R. Divakar, J. Basu, E. Enache-Pommer, J. E. Boercker, C. B. Carter, U. R. Kortshagen, D. J. Norris, and E. S. Aydil, Nano Lett. **7**, 1793 (2007)
18 Y. J. Lee, D. S. Ruby, D. W. Peters, B. B. McKenzie, and J. W. Hsu, Nano Lett. **8**, 1501 (2008)
19 M. Law, L. E. Greene, J. C. Johnson, R. Saykally, and P. Yang, Nat. Mater. **4**, 455 (2005)
20 J. Schrier, D. O. Demchenko, L. W. Wang, and A. P. Alivisatos, Nano Lett. **7**, 2377 (2007)
21 J. Noborisaka, J. Motohisa, S. Hara, and T. Fukui, Applied Physics Letters **87**, (2005)
22 M. Law, L. E. Greene, A. Radenovic, T. Kuykendall, J. Liphardt, and P. D. Yang, Journal of Physical Chemistry B **110**, 22652 (2006)
23 A. P. Goodey, S. M. Eichfeld, K. K. Lew, J. M. Redwing, and T. E. Mallouk, Journal of the American Chemical Society **129**, 12344 (2007)
24 L. E. Greene, M. Law, J. Goldberger, F. Kim, J. C. Johnson, Y. F. Zhang, R. J. Saykally, and P. D. Yang, Angewandte Chemie-International Edition **42**, 3031 (2003)
25 H. M. Lin, Y. L. Chen, J. Yang, Y. C. Liu, K. M. Yin, J. J. Kai, F. R. Chen, L. C. Chen, Y. F. Chen, and C. C. Chen, Nano Letters **3**, 537 (2003)
26 J. J. Liu, M. H. Yu, and W. L. Zhou, Applied Physics Letters **87**, (2005)
27 M. H. Huang, S. Mao, H. Feick, H. Q. Yan, Y. Y. Wu, H. Kind, E. Weber, R. Russo, and P. D. Yang, Science **292**, 1897 (2001)
28 S. A. Ivanov, A. Piryatinski, J. Nanda, S. Tretiak, K. R. Zavadil, W. O. Wallace, D. Werder, and V. I. Klimov, Journal of the American Chemical Society **129**, 11708 (2007)
29 C. Soci, A. Zhang, B. Xiang, S. A. Dayeh, D. P. R. Aplin, J. Park, X. Y. Bao, Y. H. Lo, and D. Wang, Nano Letters **7**, 1003 (2007)
30 K. Wang, J. J. Chen, W. L. Zhou, Y. Zhang, Y. F. Yan, J. Pern, and A. Mascarenhas, Adv. Mater. **20**, 3248 (2008)
31 M. Y. Lu, J. H. Song, M. P. Lu, C. Y. Lee, L. J. Chen, and Z. L. Wang, ACS Nano **3**, 357 (2009)

32 J. Yan, X. S. Fang, L. D. Zhang, Y. Bando, U. K. Gautam, B. Dierre, T. Sekiguchi, and D. Golberg, Nano Lett. **8**, 2794 (2008)
33 X. Wu, P. Jiang, Y. Ding, W. Cai, S. S. Xie, and Z. L. Wang, Adv. Mater. **19**, 2319 (2007)
34 J. E. Allen, E. R. Hemesath, D. E. Perea, J. L. Lensch-Falk, Z. Y. Li, F. Yin, M. H. Gass, P. Wang, A. L. Bleloch, R. E. Palmer, and L. J. Lauhon, Nature Nanotechnology **3**, 168 (2008)
35 V. A. Fonoberov, K. A. Alim, A. A. Balandin, F. X. Xiu, and J. L. Liu, Phys. Rev. B **73**, 165317 (2006)
36 B. D. Yao, Y. F. Chan, and N. Wang, Appl. Phys. Lett. **81**, 757 (2002)
37 H. C. Liao, P. C. Kuo, C. C. Lin, and S. Y. Chen, J. Vac. Sci. Technol. B **24**, 2198 (2006)
38 Y. M. Yu, M. H. Hyun, S. Nam, D. Lee, B. S. O, K. S. Lee, P. Y. Yu, and Y. D. Choi, J. Appl. Phys. **91**, 9429 (2002)
39 J.F. Scott, T.C. Damen, W.T. Silfvast, R.C.C. Leite, and L.E. Cheesman, Opt. Commun. **1**, 397 (1970)
40 Y. Y. Luo, G. T. Duan, and G. H. Li, Appl. Phys. Lett. **90**, 201911 (2007)
41 Y. B. Tang, Z. H. Chen, H. S. Song, C. S. Lee, H. T. Cong, H. M. Cheng, W. J. Zhang, I. Bello, and S. T. Lee, Nano Lett. **8**, 4191 (2008)
42 C. Soci, A. Zhang, B. Xiang, S. A. Dayeh, D. P. R. Aplin, J. Park, X. Y. Bao, Y. H. Lo, and D. Wang, Nano Lett. **7**, 1003 (2007)
43 S. Cho, J. W. Jang, J. Kim, J. S. Lee, W. Choi, and K. H. Lee, Langmuir **27**, 10243 (2011)
44 S. Cho, J. W. Jang, J. S. Lee, and K. H. Lee, Nanoscale **4**, 2066 (2012)
45 J. Chung, J. Myoung, J. Oh, and S. Lim, Journal of Physics and Chemistry of Solids **73**, 535 (2012)
46 S. Cho, J. W. Jang, S. H. Lim, H. J. Kang, S. W. Rhee, J. S. Lee, and K. H. Lee, Journal of Materials Chemistry **21**, 17816 (2011)
47 Z. M. Wu, Y. Zhang, J. J. Zheng, X. G. Lin, X. H. Chen, B. W. Huang, H. Q. Wang, K. Huang, S. P. Li, and J. Y. Kang, Journal of Materials Chemistry **21**, 6020 (2011)
48 J. J. Zheng, Z. M. Wu, W. H. Yang, S. P. Li, and J. Y. Kang, Journal of Materials Research **25**, 1272 (2010)

Chapter 4 ZnO/CuO Core-Shell Nanowires

4.1 Background

High cost of the materials hinders the popularity of the solar energy. Along with improving the energy conversion efficiency of solar cells, numerous works have been devoted to reducing the cost by considering the expense of materials in terms of synthesis, manufacturing, and processing. Through the thin-film processing technologies, second generation solar cells significantly reduce the cost but exhibit a relatively low efficiency. In addition, they also rely on some less abundant elements, such as indium and gallium, and toxic element like cadmium[1,2]. DSSCs, using low-cost organic dyes and titanium dioxide (TiO_2) nanoparticles in place of expensive semiconductors to absorb sunlight, leave an open question about the stability because of the problems arising from the liquid electrolytes[3,4]. Organic solar cells also suffer from the low efficiency and relatively short lifetime[5]. Generally, from materials selection point of view, several rules need be followed in searching for solar cell materials. First, elements involved should be abundant in earth's crust and economically affordable. Second, the materials should be environmentally friendly, i.e., green, to impose no potential hazard/contamination to human body and environment. Third, the materials should be chemical stable and especially inert to oxygen in pursuit of a longer operating lifetime. In light of these requirements, all-oxide semiconductors hold great promise to harvest solar light at affordable price, while maintaining acceptable energy conversion efficiency[6].

ZnO is an intrinsic *n*-type semiconductor because of the presence of oxygen vacancies and zinc interstitials. As we mentioned in Chapter 2, the band gap of ZnO is too large for visible light absorption, and therefore it is mainly used as widow layer or transparent conductive oxide in current solar industry. In the past decades, several concepts have been proposed to engineer the band gap of ZnO, in attempt to extend its absorption profile to visible light. One strategy to use ZnO in solar cells is coupling it with other narrow band gap semiconductors that act as light absorbing materials. CuO, another important semiconductor metal oxide, is a kind of intrinsic *p*-

type semiconductor with a narrow band gap (1.2~1.9 eV), which is close to the ideal energy gap of 1.4 eV for solar cells and allows for good solar spectral absorption. To date, several literatures about ZnO/CuO nanostructures for solar energy harvesting have been reported[6-9]. In this chapter, ZnO/CuO core-shell nanowires were fabricated by using a relatively simple and low-cost approach that combines CVD and PVD techniques, and the structures were characterized by electron microscopes.

To fabricate a single core-shell nanowire solar cell, two asymmetric electrodes are required to contact the core and shell respectively. A common approach is to chemically etch the shell at one end of an as-synthesized core-shell nanowire, where the area is defined by lithography techniques. However, the etching process is very sensitive to the etching time, etchant and involved several-time *e*-beam lithography, making it time-consuming and vulnerable to contamination from the etchant[10]. Therefore, another motivation of this work is to develop a new approach, from synthesis point of view, to fabricate core-shell nanowires where the cores are partly exposed. One part of the structure is consisting of a core-shell nanowire while the other part consisting of a single-component nanowire. To simplify, this structure is referred as *asymmetric core-shell nanowire* in the following contexts in this dissertation.

4.2 Experimental

Synthesis of ZnO oxide nanowire array on sapphire substrate

The details for synthesizing well-aligned ZnO nanowire array on *a-plane* sapphire substrate were described in Section 2.3 in Chapter 2.

Fabrication of ZnO/CuO core-shell nanowire array on sapphire substrate

Two geometries of ZnO/CuO core-shell nanowires were fabricated. One is ZnO/CuO core-shell nanowire and the other one is asymmetric ZnO/CuO core-shell nanowire. In realization of the first geometry, ZnO nanowire array grown on sapphire substrate was loaded in PVD chamber to conduct CuO sputtering. The thickness of the coating can be read from the thickness monitor. To fabricate core-exposed ZnO/CuO core-shell nanowire, a detailed process will be described later.

Device fabrication

The as-synthesized nanowires were removed from the sapphire substrate and ultrasonically dispersed in alcohol. For device fabrication, several drops of nanowire-alcohol solution were then deposited onto Si/SiO_2 (600nm) substrates with photolithographically defined electrodes. Two layer of PMMA was spin-coated on the substrate and baked at 100^oC for 90s. The substrate was then transferred to SEM for e-beam lithography. After development and metallization, lift-off process was conducted in acetone. The final devices were completed by connecting the lead to the pads defined by photolithography.

Characterization

The as-synthesized nanowires were first characterized by a Carl Zeiss 1530 VP FESEM and a JEOL 2010 conventional TEM. The initial composition analyses were conducted by the EDS equipped on the FESEM and TEM. Detailed structural characterization was achieved by high-angle annual dark-field (HAADF) scanning TEM (STEM) by a JEM-2100 F field emission TEM with CEOS C_s-corrector and the HAADF detection angle was 73-194 mrad. The basic *I-V* characteristics of these devices were measured by Keithley 2400 source meter.

4.3 Results and discussion

4.3.1 ZnO/CuO core-shell nanowire

SEM images of ZnO/CuO core-shell nanowire array are shown in Figure 4.1(a)~(c). After CuO sputtering, the nanowire array still remained vertically aligned, although a few nanowires adhere together. Most of the nanowires exhibited a larger diameter in top section than that of the bottom section, because the nanowires had an average length of 5~μm and prevented the CuO species from diffusion to the bottom of ZnO nanowire array. From the high magnification SEM image taken from the tips of the nanowires in Figure 4.1(c), we can observe the diameter evolution. XRD pattern of ZnO/CuO core-shell nanowire array was shown in Figure 4.1(d). Two high intensity peaks were ascribed to (002) planes of ZnO and (110) planes of Al_2O_3,

respectively. Surprisingly, no peak corresponding to CuO was indentified, possibly owing to the small volume ratio of CuO with respect to ZnO in this core-shell system.

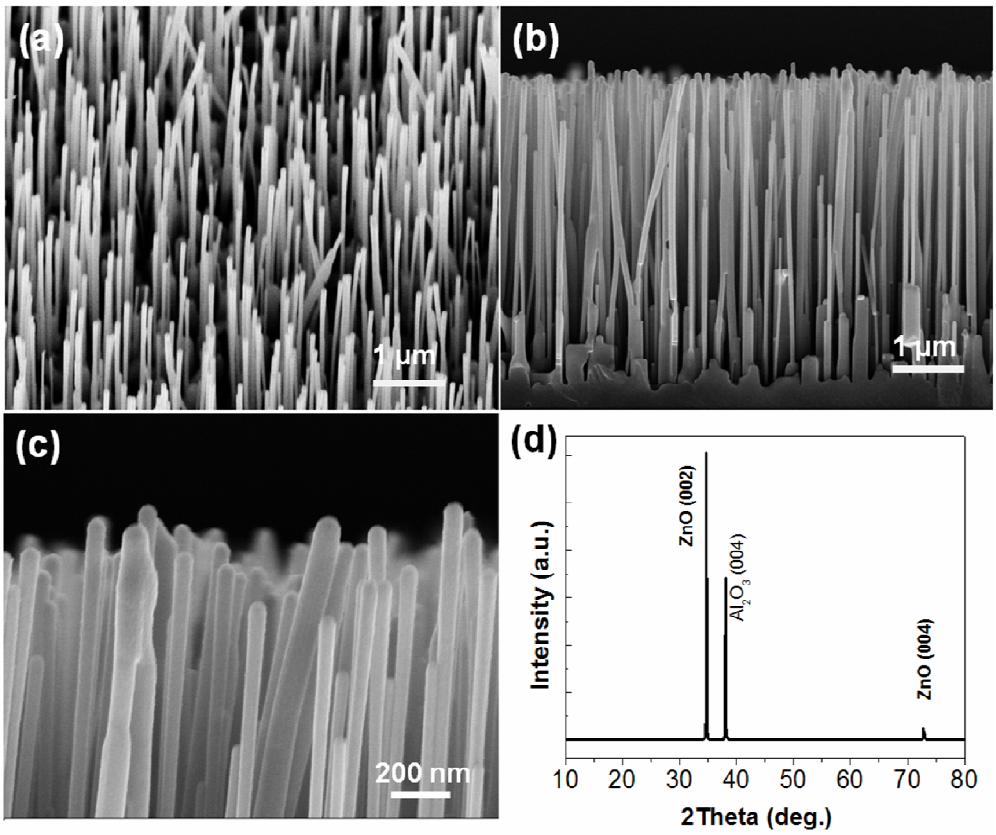

Figure 4.1 (a) Titled view magnification SEM images of ZnO/CuO core-shell nanowire array on sapphire substrate. (b) and (c) are the cross-section view SEM images of ZnO/CuO core-shell nanowire array and its corresponding higher magnification of the tips,respectively. (d) XRD pattern of ZnO/CuO core-shell nanowire array on sapphire substrate.

Figure 4.2 (a) shows a low magnification TEM image of ZnO/CuO core-shell nanowire, which exhibited obvious core-shell geometry. A layer of CuO with the thickness of 40 nm was directly deposited over the ZnO nanowire, as shown in Figure 4.2 (b) and (c), despite slightly thicker coating in the tip. Some *Moiré* fringes can be easily observed in the shell layer, indicating that the CuO shell was crystallized in polycrystalline form. HRTEM image was recorded along the interface and shown in Figure 4.2(d). ZnO core was revealed to be grown along *c*-axis.

Nanoprobe EDS line scanning was conducted along the dot array in Figure 4.2(e), further confirming the core-shell geometry.

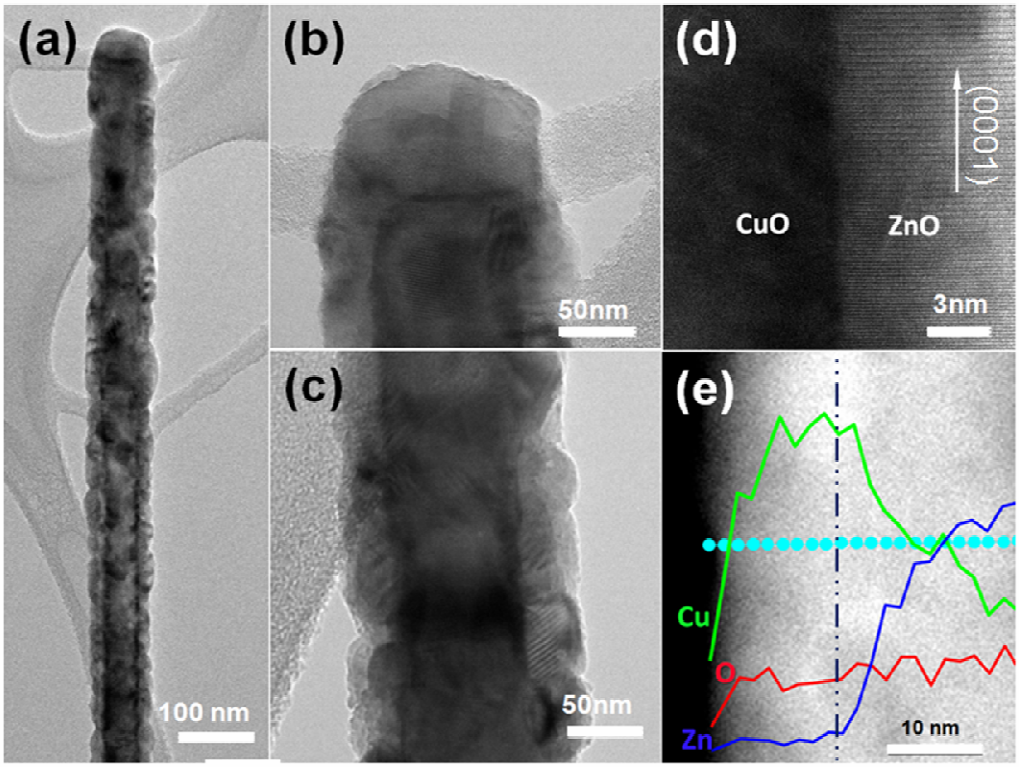

Figure 4.2 TEM analysis of ZnO/CuO core-shell nanowire. (a) Lower magnification TEM images of ZnO/CuO nanowire, showing the evident interface; (b) and (c) are the higher magnification TEM images of ZnO/CuO nanowire, respectively; (d) HRTEM of the interface; (e) STEM analysis of the element distribution of the interface. HRTEM image was recorded from the interface between the core and shell.

4.3.2 ZnO/CuO asymmetric core-shell nanowire

The schematic for fabricating asymmetric ZnO/CuO core-shell nanowire is depicted in Figure 4.3, as well as the corresponding SEM images during the procedure. A layer of PMMA was spin coated on the nanowire array. Note that PMMA need to be diluted by acetone to facilitate the filling speed. Note that a well aligned ZnO nanowire array is highly desired to facilitate the photoresist filling and CuO coating.

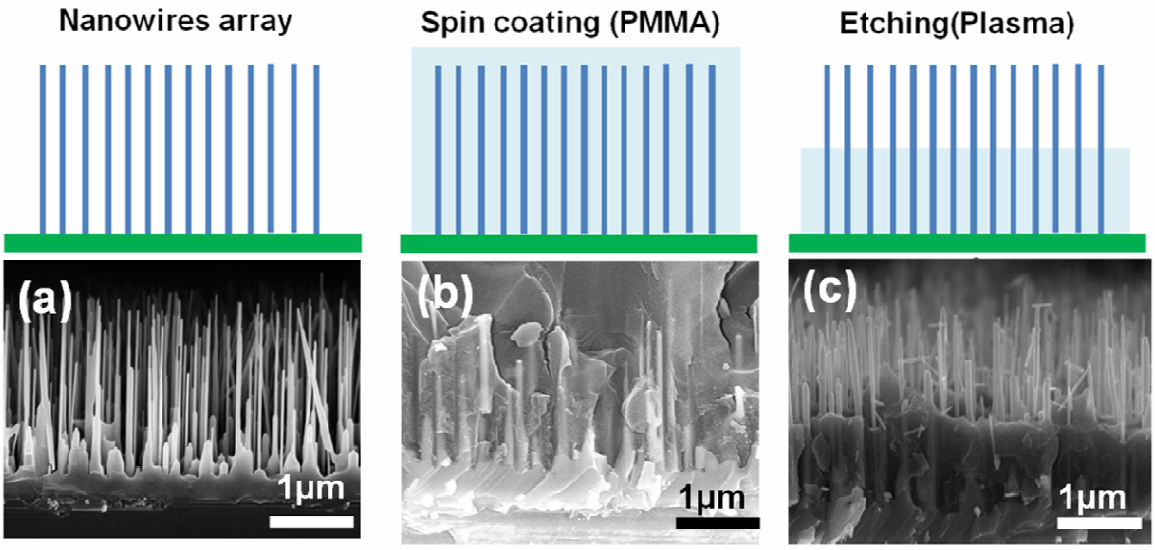

Figure 4.3 The upper row shows schematics of the procedure to fabricate half-exposed nanowire. (a)~(c) SEM images of nanowire array before coating PMMA, after coating PMMA and with part of PMMA removed by oxygen plasma.

The cross-section SEM images of ZnO nanowire array were recorded during the process and shown in Figure 4.3(a)~(c). Figure 4.3 (a) is a representative SEM image of ZnO nanowire array, exhibiting vertical alignment and a length of ~5 micrometers. After coated with modified PMMA, all nanowires were embedded in the photoresist, as shown in Figure 4.5(b). To eliminate the charge accumulation during SEM observation, a 5 nm-thick gold layer was sputtered over the cross-section. Figure 4.5(c) displays the cross section SEM image of ZnO nanowire after 10 min oxygen plasma etching, clearly showing that the nanowire array is partly exposed. The sample was then transferred to PVD chamber for CuO coating. Finally, the PMMA was removed by dipping the substrate in acetone for seconds.

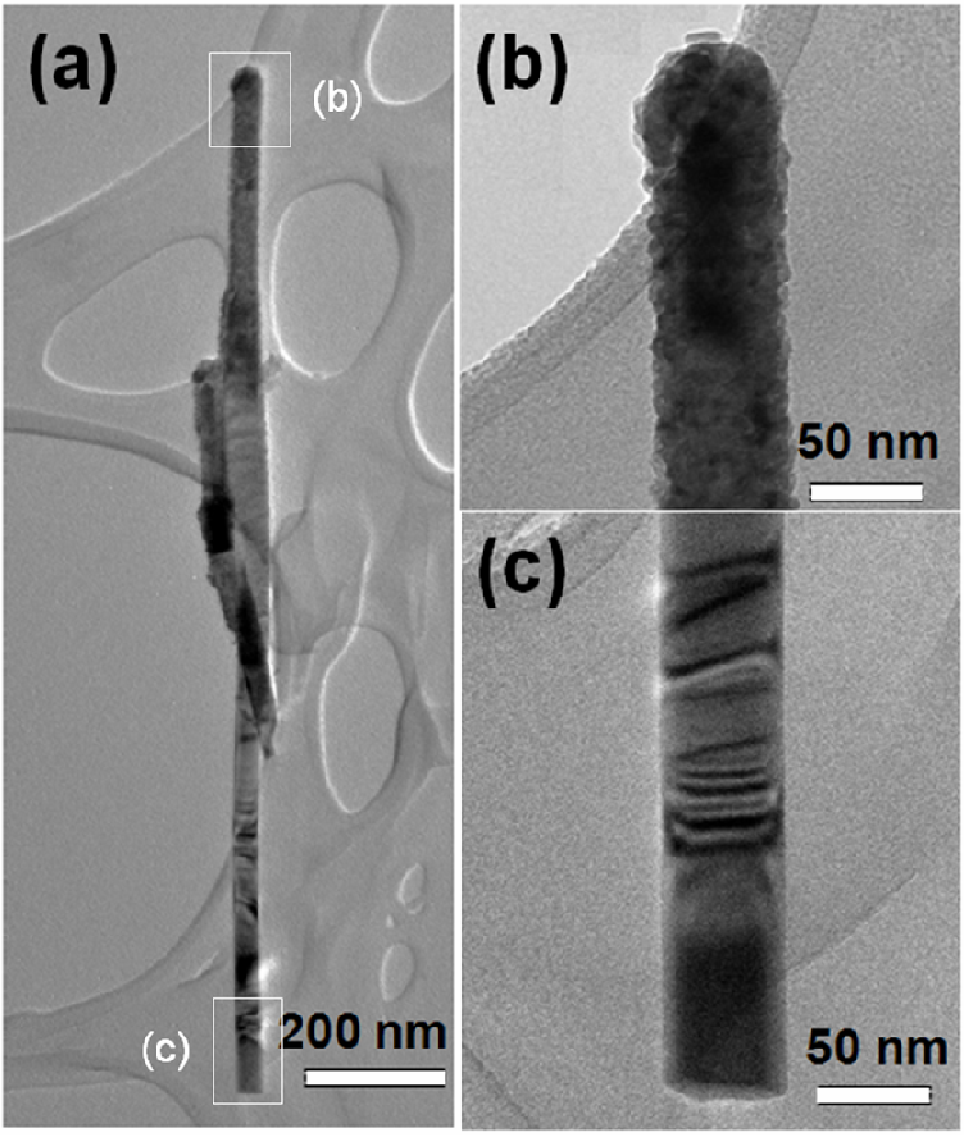

Figure 4.4 (a)Low magnification TEM image of ZnO/CuO asymmetric core-shell nanowire.(b) TEM images taken from the frames labeled in (a), confirming that the top section of ZnO nanowire was coating with CuO.

Subsequently, the nanowires were removed from the sapphire substrate and dispersed in alcohol for TEM sample preparation and device fabrication. A low magnification TEM image of a ZnO/CuO asymmetric core-shell nanowire was shown in Figure 4.4(a), revealing a coated tip and a bare bottom part. Corresponding high magnification TEM images of the top and bottom parts have been taken from the frame (b) and (c) labeled in Figure 4.4(a), confirming that the tip part was fully coated with CuO and the bottom part was bare ZnO.

The device was fabricated based on a ZnO/CuO asymmetric core-shell nanowire. The process was simplified because no further shell etching process was required. The SEM image of a typical device was displayed in the inset of Figure 4.5 (a), showing a nanowire bridged across a

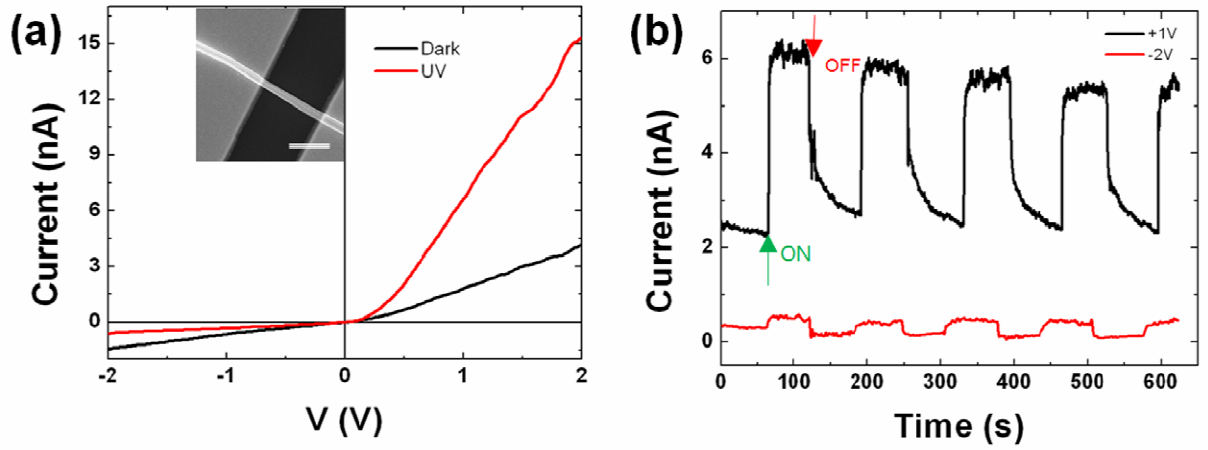

Figure 4.5 (a) Current *(I) vs* voltage *(V)* for an individual ZnO/CuO nanowire, revealing the diode characteristic of ZnO/CuO heterojunction; Inset shows the device of ZnO/CuO nanowire bridged gold electrode. Scale bar is 300 nm. (b) Time-dependent photocurrent of ZnO/CuO nanowire with +1V and -2V external bias.

pair of gold electrodes. The electrical properties of ZnO/CuO core-shell nanowire were measured with and without UV illumination. A *rectifying* behavior was observed, suggesting the possibility of the *p-n* junction formation between *n*-type ZnO core and *p*-type CuO shell. However, the contribution of the Schottky contact between gold and ZnO to the rectifying characteristic cannot be totally ruled out.

Figure 4.5 (b) shows the dynamic photoresponses measured from the fabricated ZnO/CuO nanowire device. The dark current was measured for 60 sec under a dark environment, and then the UV lamp was turned on for 60 sec to measure the photocurrent. With a +1 V applied bias, it was found that the current of CuO/ZnO nanowire photodiode was around 2.5 nA. Upon UV illumination, it was found that the current increased to 6.5 nA. When the UV lamp was turned OFF again, the current decreased to its original value. While a -2 V voltage was applied, the current was found to increase from 0.25nA to 0.5nA when UV lamp was switched OFF to ON. The response and recovery speeds are also important parameters for the photodiode. One can define the times required reaching 90% of the final equilibrium value as the response/recovery

time, in analogy to evaluate the gas sensing response/recover rate. It was found that the photoresponse curve had steep rise edge (less than 5s) but an obvious decay tail (more than 45s), when +1 V bias was applied. Given the polycrystalline CuO shell and low quality interfaces, the prolonged decay edge can be attributed to the gradual release of the trapped electrons after light is turned off. The similar results were also observed in photoconductivity of CdSe nanowire[11].

4.4 Conclusion

In summary, *n*-ZnO/*p*-CuO core-shell nanowires were successfully synthesized and the structural and electrical properties were investigated. In order to simplify single nanowire solar cell fabrication, a new approach was developed to fabricate asymmetric core-shell nanowires. As a demonstration, ZnO/CuO core-shell nanowires exhibited obvious rectifying behavior. Notably, a similar concept has been demonstrated on Si/TiO_2 asymmetric core-shell nanowire array by Yang *et al.* in UC Berkley[12]. Although this approach needs to be optimized for depositing shell materials at high temperature, it provides the feasibility to fabricate a large number of asymmetric core-shell nanowires without any etching steps.

Reference

1 M. A. Green, Journal of Materials Science-Materials in Electronics **18**, S15 (2007)

2 S. Martinuzzi, Solar Cells **5**, 243 (1982)

3 M. I. Asghar, K. Miettunen, J. Halme, P. Vahermaa, M. Toivola, K. Aitola, and P. Lund, Energy & Environmental Science **3**, 418 (2010)

4 G. Hashmi, K. Miettunen, T. Peltola, J. Halme, I. Asghar, K. Aitola, M. Toivola, and P. Lund, Renewable & Sustainable Energy Reviews **15**, 3717 (2011)

5 A. Pivrikas, N. S. Sariciftci, G. Juska, and R. Osterbacka, Progress in Photovoltaics **15**, 677 (2007)

6 B. D. Yuhas and P. D. Yang, Journal of the American Chemical Society **131**, 3756 (2009)

7 X. H. Zhao, P. Wang, and B. J. Li, Chemical Communications **46**, 6768 (2010)

8 H. T. Hsueh, S. J. Chang, W. Y. Weng, C. L. Hsu, T. J. Hsueh, F. Y. Hung, S. L. Wu, and B. T. Dai, Ieee Transactions on Nanotechnology **11**, 127 (2012)

9 Jhin-Wei Chen, Dung-Ching Perng, and Jia-Feng Fang, Solar Energy Materials and Solar Cells **95**, 2471 (2011)

10 Q. L. Bao, C. M. Li, L. Liao, H. B. Yang, W. Wang, C. Ke, Q. L. Song, H. F. Bao, T. Yu, K. P. Loh, and J. Guo, Nanotechnology **20**, (2009)

11 Z. B. He, J. S. Jie, W. J. Zhang, W. F. Zhang, L. B. Luo, X. Fan, G. D. Yuan, I. Bello, and S. T. Lee, Small **5**, 345 (2009)

12 C. Liu, Y. J. Hwang, H. E. Jeong, and P. D. Yang, Nano Letters **11**, 3755 (2011)

Chapter 5 Core-Shell Nanowires with High Quality Interfaces for Single Nanowire Photovoltaic Device Fabrication

5.1 Background

To date, nanowire solar cells, processed from either an individual nanowire or nanowire array, exhibit inferior energy conversion efficiency in comparison to their counterpart planar solar cells, even though numerous efforts have been dedicated to this field[1-4]. This could be mainly ascribed to the severe non-radiative recombination loss in reduced dimensionality. On one hand, owing to its large surface-to-volume ratio, nanowires have a high surface recombination velocity, thus shortening the carrier lifetime by a factor of 4-5[5]. This is the inherent drawback of using nanowires in carrier collection, which is notably detrimental to the device performance of silicon or other III-V nanostructures. In order to minimize the surface recombination, several groups adapted surface passivation techniques, i.e., formation of a layer of materials on the nanowire surface, which has demonstrated remarkable improvement of the device performance[6,7]. Alternatively, materials with lower surface recombination velocity can be chosen to build a nanowire solar cell. On the other hand, the interface recombination occurring along the material junction in nanowire solar cells, especially for those having core-shell geometries, is another factor that drastically limits the photovoltaic performance. Evidently, to enhance the efficiency in core-shell nanowire solar cells, the straightforward task is to seek a material combination with high quality interfaces and a rational approach to realize it. An example of this, is the recent report of CdS/Cu_2S core-shell nanowire solar cell fabricated by cations exchange in chemical solution, manifesting a high quality interface, and demonstrating a remarkable efficiency of 5.4%[8].

In general, group II-VI compound semiconductors have a relatively lower surface recombination velocity[9,10], and therefore, hold the potential to build nanowire solar cells delivering high energy conversion efficiency without any further surface passivation. To construct a *p*-*n* heterojunction among the II-VI semiconductors, one has the option of using *p*-ZnTe and *p*-CdTe to couple with *n*-type CdS, CdSe, ZnS and ZnSe, respectively, because of

the challenging remains in doping ZnTe to *n*-type. Moreover, in order to obtain the possibility of heteroepitaxial growth, i.e., a high quality interface, several factors, including the lattice mismatch, thermal expansion coefficients, cross-diffusion, auto doping, and traps and interface sates, etc., should be taken into account[11,12]. In this regard, CdSe and ZnTe stand out of all II-VI semiconductors for heteroepitaxial junction fabrication, because of their distinguished parameters/properties over others in terms of less lattice mismatch, similar thermal expansion coefficients, type-II band offset and well-established doping capability. In detail, from a structure point of view, both CdSe and ZnTe can be crystallized as wurtzite and zinc-blende. CdSe can be easily *n*-doped and crystallizes in wurtzite structures naturally; however, it could be grown on ZnTe substrate in zinc-blende structure with a lattice mismatch of only 0.3%. Similarly, ZnTe could be grown on CdSe substrate to maintain a wurtzite structure with a lattice mismatch of 0.4%, even though its equilibrium crystal structure is zinc blende. The possible heteroepitaxial growth between ZnTe and CdSe enables us to obtain a high quality interface with extremely low defect density. Moreover, the similar thermal expansion coefficient between CdSe and ZnTe could contribute to the formation of a stable and reliable device structure. Additionally, type-II band alignment lies in between CdSe and ZnTe and the doping capability of ZnTe and CdSe allow for tailoring the optical and electrical properties of the whole device, leading to various applications in optoelectronics beyond solar energy harvesting.

As a good candidate combination in solar cell applications, CdSe/ZnTe heterojunction has attracted considerable attention for the fabrication of thin film solar cells in the past decades. Double layer structured thin film solar cells, comprising of indium-doped CdSe and ZnTe, have been reported with a total efficiency of 1.86%[13]. Recent progress of CdSe/ZnTe heterojunction solar cell consisting of MBE grown ZnTe and CdSe on GaSb substrate, showed an open-circuit voltage and fill factor of 0.4V and 53% respectively[14]. Significantly, this lattice-matched materials combination is a very promising system for fabricating multiple junction solar cells. Covering the visible region of spectrum from 470 nm to 860 nm, a monolithic three-terminal tandem cell, *n*-ZnSe/*p*-ZnTe/*n*-CdSe, has demonstrated an efficiency of 10.8%, while the ZnTe/CdSe device had the largest contribution to the overall efficiency[15].

Despite several literatures about the nanocrystals or nanocables with special emphasis on the materials synthesis, up to date, there is no report on the CdSe/ZnTe or ZnTe/CdSe nanowire

optoelectronics, principally because of the interface issue and the lack of efficient approaches to realize the device[16-19]. Notably, CdSe/ZnTe core-shell nanocrystals, or quantum dots, have been intensively investigated as a well-known type-II system, exhibiting interesting phenomena such as ultra fast holes transfer[17], extended absorption spectrum, interfacial band emission, etc. CdSe/ZnTe nanocables have been demonstrated in a solution system, though representing discontinuous epitaxial ZnTe shell or nanoislands on CdSe quantum wires[18].

In this chapter, a two-step technique was employed to fabricate core-shell nanowires. Firstly, both ZnTe and CdSe nanowires, acting as templates for the further coating, were synthesized by either thermal evaporation or pulsed laser ablation on various substrates. Specially, vertically aligned CdSe nanowire array was synthesized on muscovite mica substrates through thermal evaporation. Secondly, two types of coaxial nanoheterostructures, ZnTe/CdSe and CdSe/ZnTe core-shell nanowire were attempted to be obtained by pulsed laser ablation of respective target materials over the templates. Morphologies and structural information was collected and analyzed by SEM, TEM, XRD and Raman spectra. Finally, solar device based on an individual CdSe/ZnTe core-shell nanowire was demonstrated, which suggested that such a core-shell geometry with heteroepitaxial growth hold the promise to improve the efficiency of nanowire solar cells.

5.2 Synthesis and structural analysis of ZnTe/CdSe heterostructured nanowires

Previous works on ZnTe/CdSe heterojunction and superlattice in thin film majorly fabricated CdSe on ZnTe substrates[12,20] or grew the CdSe layer after the ZnTe layer was done[13]. In the same manner, we first grew ZnTe nanowire and then coated the ZnTe with CdSe in order to obtain ZnTe/CdSe core-shell nanowire. ZnTe, a direct band gap semiconductor, has wide application in green-light emitting diodes, X-ray detectors and solar cells. Various techniques have been used to synthesize ZnTe nanostructures, such as hydrogen assisted thermal evaporation[21], molecular beam epitaxy[22], and pulsed electrochemical deposition[23]. Moreover, the *p*-type conductivity of ZnTe nanostructures have been reported in as-synthesized, copper and nitrogen doped ZnTe nanowires and nanoribbons[24,25].

Experimental

Synthesis of ZnTe nanowires

Herein, a modified hydrogen assisted-thermal evaporation technique was used to obtain ZnTe nanowires. Specifically, 0.3g commercial-grade ZnTe power (99.99%, Alfa Aesar) was located in an alumina crucible and placed in the center of a 1-inch diameter horizontal tube furnace. A piece of silicon substrate sputtered with 2nm gold was located in the downstream to collect the products. A gas mixture of 160:40 SCCM of Ar/H_2 was introduced into the tubes and the pressure in the tube was maintained at 760Torr. The furnace was elevated to 800^{o}C at a ramping rate of 25^{o}C/min and the duration of reaction was 45 minutes. The dark-brownish product was collected on the silicon substrate after the furnace was cooled down to room temperature.

Synthesis of ZnTe/CdSe nanowires

In order to synthesize ZnTe/CdSe core-shell nanowires, the silicon substrate with as-grown ZnTe nanowires was transferred into a home-made pulsed laser ablation system. CdSe powder (99.95%, Alfa Aesar) was cold-pressed into a pellet as the ablation source. The distance between target and silicon substrate was measured as 40mm. Before the laser beam was directed to the target, the system was pumped down to 30mTorr and the temperature was increased to 350^{o}C. A Nd:YAG laser (LOTIS-TII,LS2147) with wavelength 1064 nm was used in the deposition. The energy flux of the laser beam was set as 360mJ/cm^2 with a wavelength of 1064 nm and a frequency of 5Hz. The ablation was performed for 15min, and the final product was collected for structure characterization.

5.2.1 Structure analysis of ZnTe nanowires

As shown in the SEM image in Figure 5.1(a), ZnTe nanowires obtained by thermal evaporation had a diameter of 100nm and most of them exhibited a length of tens of micrometers. Figure 5.1(b) shows XRD pattern of ZnTe nanowires on silicon substrate. All the diffraction peaks can be indexed to a standard diffraction card (JCPDS No. 15-0746), indicating that ZnTe nanowire crystallizes in zinc blende structures (space group F-43m (216)). Two representative microstructures of ZnTe nanowires were revealed by low-magnification TEM images in Figure

5.1 (c) and (e). One is straight and the other one exhibits periodic twins through the entire nanowire. HRTEM and corresponding SEAD analysis of the straight nanowire, as shown in Figure 5.1 (d), suggested the single crystalline nature of ZnTe nanowire and the preferential growth direction. The lattice plane distance measured as 0.35nm corresponds to the planes {111}. Figure 5.1 (f) shows the HRTEM image of the twin nanowires. The twin nanowire still grows along the [111] direction and the angle between two symmetry facets is 141^{o}. The formation of periodic twins is believed to result from periodic surface tension because of eutectic liquid droplet in VLS growth mechanism, which had been elucidated in references[21,26]. Note that an amorphous layer, as marked by dashed lines in Figure 5.1 (c) and (e), was observed in the surfaces of the both nanowires. Because the entire growth process was carried out in hydrogen contained atmosphere, the amorphous layer could be ascribed to the exposure to air during the transfer and storage. The outside layer was also observed in ZnTe nanowires synthesized by molecular beam epitaxy, and it was identified as ZnO nanocrystal embedded in amorphous layer[27,28]. This native oxide layer plays a crucial role to hinder the growth of an epitaxial shell on the nanowire, which will be discussed later in this section.

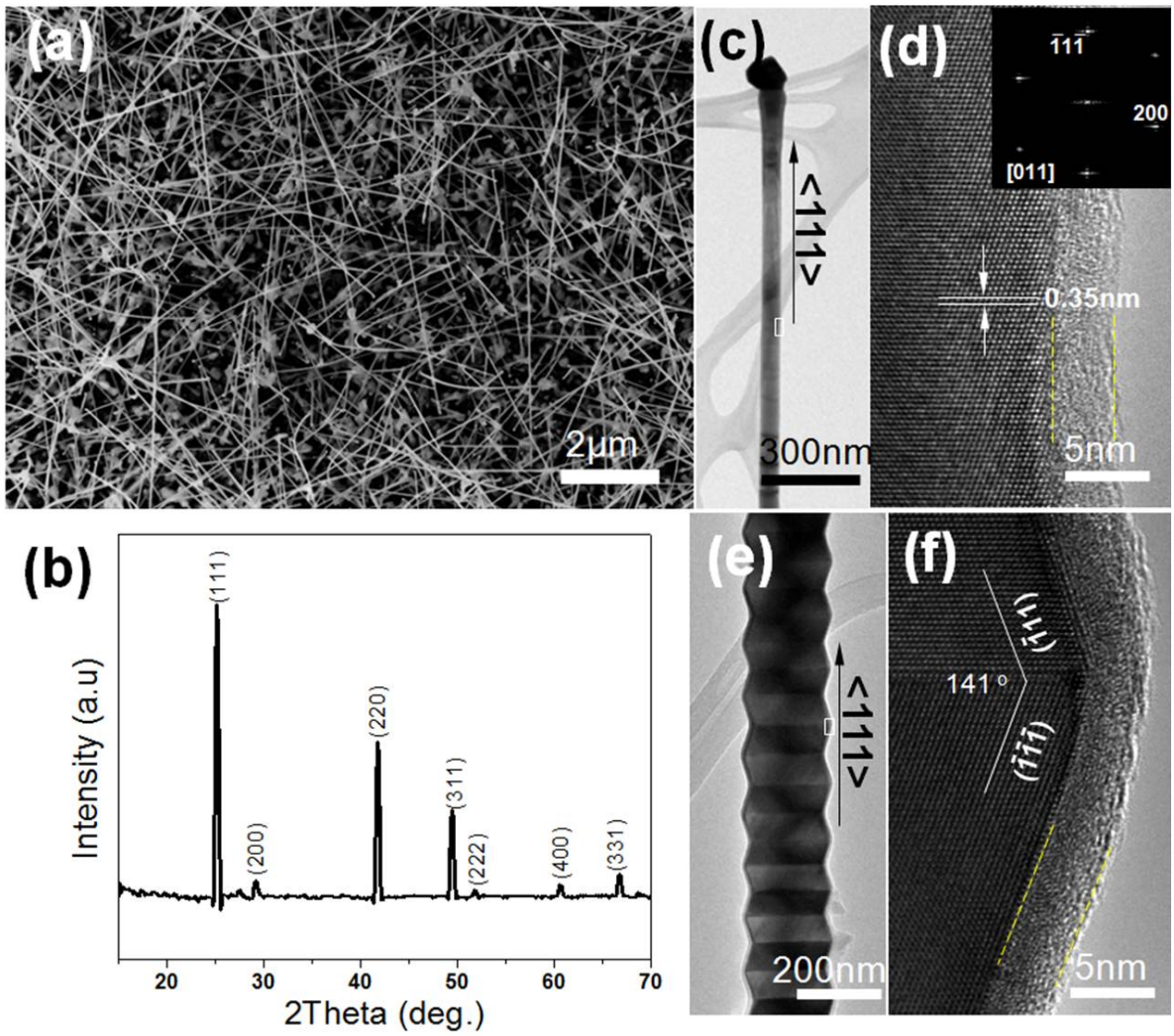

Figure 5.1 Structure analyses of ZnTe nanowires synthesized by thermal evaporation. (a) SEM image of ZnTe nanowires collected on silicon substrate.(b)XRD pattern of ZnTe nanowires.(c) and (d) Low magnification TEM images of ZnTe nanowires, implying two different microstructures. (e) and (f) HRTEM images of ZnTe nanowire, corresponds to the frame marked in (c) and (e), respectively. The native oxide layer was highlighted by dash line.

5.2.2 Structure analysis of ZnTe/CdSe nanowires

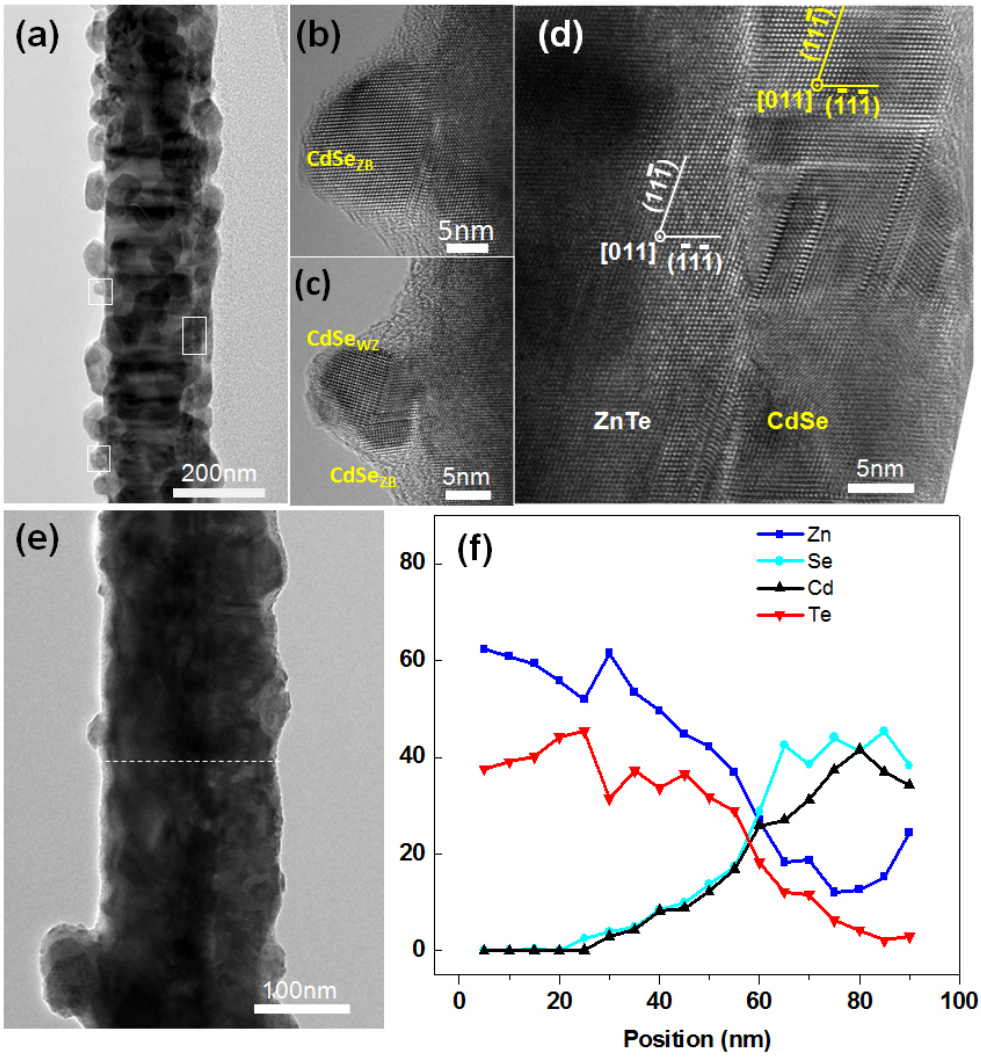

Figure 5.2 Structure analysis of ZnTe/CdSe nanowires.(a) Low magnification TEM images of ZnTe/CdSe nanowires.(b) and(c) HRTEM images of CdSe nanocrystals epitaxially grown over ZnTe nanowires. (c) Interface of ZnTe/CdSe nanowire exhibiting epitaxial relationship. (e)A low magnification TEM images of ZnTe/CdSe nanowires showing the inhomogeneous coating because of non-alignment. (f) Nanoprobe EDS result recorded along the dash line marked in (e).

To investigate the possible growth relationship between the $ZnTe_{ZB}$ and CdSe, we carried out the coating procedure. SEM image was not shown here because no obvious change in morphologies before and after coating were observed, except a rough surface. Detailed morphologies and structural information were recorded and analyzed by TEM. Low magnification TEM image in Figure 5.2 (a) revealed that several CdSe nanocrystals were attached on one side of the ZnTe nanowire and the other side of the ZnTe was covered by a continuous layer. Higher magnification TEM images of the nanocrystals, taken from the white frames in Fig.5.2 (a), were shown in Figure 5.2 (b) and (c). Zinc blende CdSe nanocrystal, stacking in a sequence of ……*ABCABCAB*……, was observed in Figure 5.2 (b). Additionally, HRTEM image in Figure 5.2 (b) revealed that both wurtzite and zinc blende crystal structures coexisted in an individual CdSe nanocrystal. Note that all the CdSe nanocrystals indeed, grow epitaxially over the surface of ZnTe nanowire with a continuous lattice fringe. Especially, wurtzite CdSe nanocrystals were formed by taking zinc-blende CdSe layer as a barrier in conjunction to the zinc blende ZnTe nanowire. On the thick layer side, CdSe layer crystallized in zinc blende structure, despite a number of dislocations and other defects. A epitaxial relationship between the core and shell layer could be identified as $(011)_{ZnTe}//(011)_{CdSe}$ and $(11\text{-}1)_{ZnTe}//(11\text{-}1)_{CdSe}$. It should be noting that most of the nanowires were inhomogeneous coated, primarily because they were randomly distributed and the ablated CdSe vapor was blocked. This assumption was further verified by the low magnification TEM image and corresponding nanoprobe line-scan EDS spectrum. Clearly, the ZnTe nanowire shown in Figure 5.2 (e) had one side coated and the other side barely coated. Notably, as compared to the clean and sharp surface of CdSe nanocrystals, the native oxide was still observed in ZnTe nanowires, which possibly hinders the epitaxial growth in this system.

ZnTe nanowires synthesized by thermal evaporation exhibited different structures and tended to form amorphous layer, which are not ideal candidates to obtain conformal shells. However, significantly, the observation that the nanocrystals epitaxially grew over the nanowires fabricated by pulsed laser ablation, provides potential way to synthesize quantum dots in a gas phase and enhance the efficiency of current quantum dots optoelectronics. To date, most of the quantum dots are synthesized in the solution phase because this route offer more parameters to tailor the size, shape and composition and therefore the properties of quantum dots. However, the unavoidable surfactants in this method generally degrade the device performance. Even though some challenges, such as dispersion, shape controllability, and yield, can be expected, pulsed

laser ablation is a promising way to achieve surfactant-free QDs. This, together with the possible epitaxially gown quantum dots on nanowire, will benefit for the charge collection and transport in optoelectronics. For instance, QDSSCs composed of nanowire, taking QDs as light absorber, suffer from the recombination loss arising from the interfaces between the nanocrystals and nanowires. By deliberately controlling the deposition parameters and the materials, nanocrystals can be epitaxially grown on nanowires, leading to enhanced energy conversion efficiency by dramatically minimizing the interfacial recombination.

5.3 Synthesis and structural analysis of CdSe/ZnTe core-shell nanowires

5.3.1 Synthesis and structure analysis of CdSe nanowire

1D CdSe nanostructures, such as nanowires, nanobelts, and nanorods, have been synthesized by different techniques, ranging from thermal evaporation, pulsed laser deposition to cation-exchange, chemical electrodeposition and hydrothermal/solvothermal routes, which are believed to have wide applications in optoelectronics, laser, luminescence, and biomedical imaging. Among of all the techniques, gas vapor transport is the most popular method to obtain CdSe nanostructures. In this section, various CdSe nanostructures were synthesized by thermal evaporation and pulsed laser ablation methods on silicon and muscovite mica substrates. The morphologies and structures were characterized by electron microscopes and X-ray diffractometer. Finally, a well separated CdSe nanowire on silicon substrate, acting as templates, was then transferred to a coating system in pursuit of CdSe/ZnTe core-shell nanowires.

Experimental

Synthesis of CdSe nanowires on silicon substrate by pulsed laser ablation

First, a disc-shaped target of CdSe was fabricated by cold pressing the commercially available powder (Alfa Aesar, 99.95% purity, metal basis). The target was then positioned in the middle of quartz tube, which was inserted in the horizontal tube furnace. Subsequently, a silicon substrate coated with ~ 10 nm gold thin films was used to collect the products. In order to investigate the influence of laser power, temperature, and pressure on the morphologies of CdSe

nanostructures, two sets of parameters were used for the laser ablation processes. In the first set of parameters, the collecting substrate was placed in front of the target at a distance of 2 cm and the entire system was pumped down to 40mTorr. The laser wavelength used for the ablation was the fundamental wave (1064 nm) with the repetition rate of 5 Hz, and the energy of 27mJ/pulse. After the temperature of the furnace was increased to 450^{o}C, the laser beam was directed to ablate CdSe target. The pressure of the system was maintained at 45mTorr, and the samples were collected for an ablation time of 5mins and 15mins. In the second set of parameters, the system was pumped down to 40mTorr and backfilled with argon three times to ensure no oxygen remains. Finally, a 200 SCCM Ar/H_2 (88%/12%) gases was introduced and the whole system was maintained at atmospheric pressure. The temperature was increased to 750^{o}C at a ramping rate of 25 ^{o}C/min. A 30mJ/pulse pulsed Nd:YAG laser (1064 nm, 10 Hz) was used to ablate the target and the substrates were located in the downstream at a distance of 8cm from the center of the furnace. After the furnace was cooled down to room-temperature, the substrates were taken out from the tube. A very thin yellowish layer from the first set parameters and a thick brown layer of products from the second set parameters were observed by naked eyes, respectively. Both samples were then characterized by electron microscopes and XRD.

Synthesis of CdSe nanowires on silicon substrate by thermal evaporation

The thermal evaporation of CdSe was conducted in a horizontal tube furnace in Ar/H_2(4:1) mixtures atmosphere. Briefly, 0.1g CdSe powder (Alfa Aesar, 99.95% purity, metal basis) was loaded in to a crucible and positioned in the center of quartz reactor which was placed in the furnace. Prior to increasing temperature, the quartz reactor was pumped down to 30mTorr in order to eliminate oxygen. The quartz reactor was then backfilled with Ar/H_2 gases and maintained at atmospheric pressure. While the source was allowed to evaporate at 770^{o}C for 45min under a 150 SCCM Ar/H_2 gases, the CdSe nanowires were collected from the 10nm-gold coated silicon substrate in the downstream. The substrate was taken out at room temperature and a dark -grey- product on the substrate was observed.

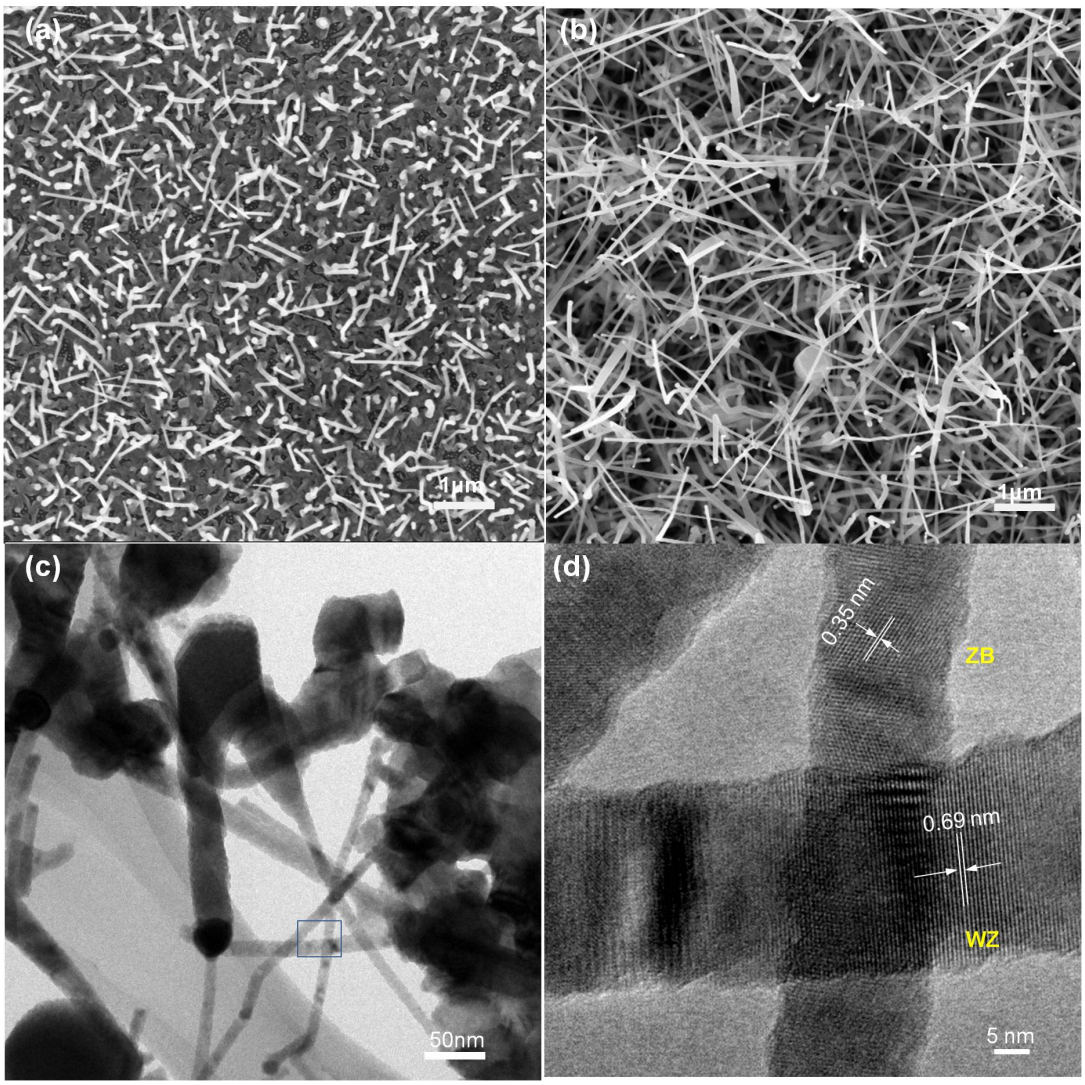

Figure 5.3 Structure analysis of CdSe nanowires synthesized at 450°C. (a) and (b) SEM images of CdSe nanowires collected after 5 min and 10 min laser ablation. (b) Low magnification TEM image of CdSe nanowires collected after 5mins laser ablation. (d) High magnification TEM image from the frame labeled in (c), showing both stacking sequence of zinc blende and wurtzite structure.

5.3.1.1 CdSe nanowires on silicon substrate by pulsed laser ablation

Figure 5.3 (a) and (b) shows the typical SEM images of CdSe nanowires collected after laser ablation for 5min and 15min, respectively. With 5min ablation, nanowires with length of several micrometers were observed directly grown on CdSe layer, which was formed in the initial vapor deposition. High aspect ratio CdSe nanowires were harvested after 15mins ablation, as shown in Figure 5.3(b), exhibiting tangled morphologies with a few tapered ribbon structures. TEM

sample was prepared from the sample collected at 5mins and the corresponding TEM images were shown in Figure 5.3(c) and (d). The diameters of the nanowires were measured around 20nm and mixed with CdSe nanoparticles, which are assumed to be scratched from the substrate during the TEM samples preparation. In an enlarged area marked in Figure 5.3(c), both wurtzite and zinc blende structures of CdSe were identified. The lattice plane distances of 0.69nm and

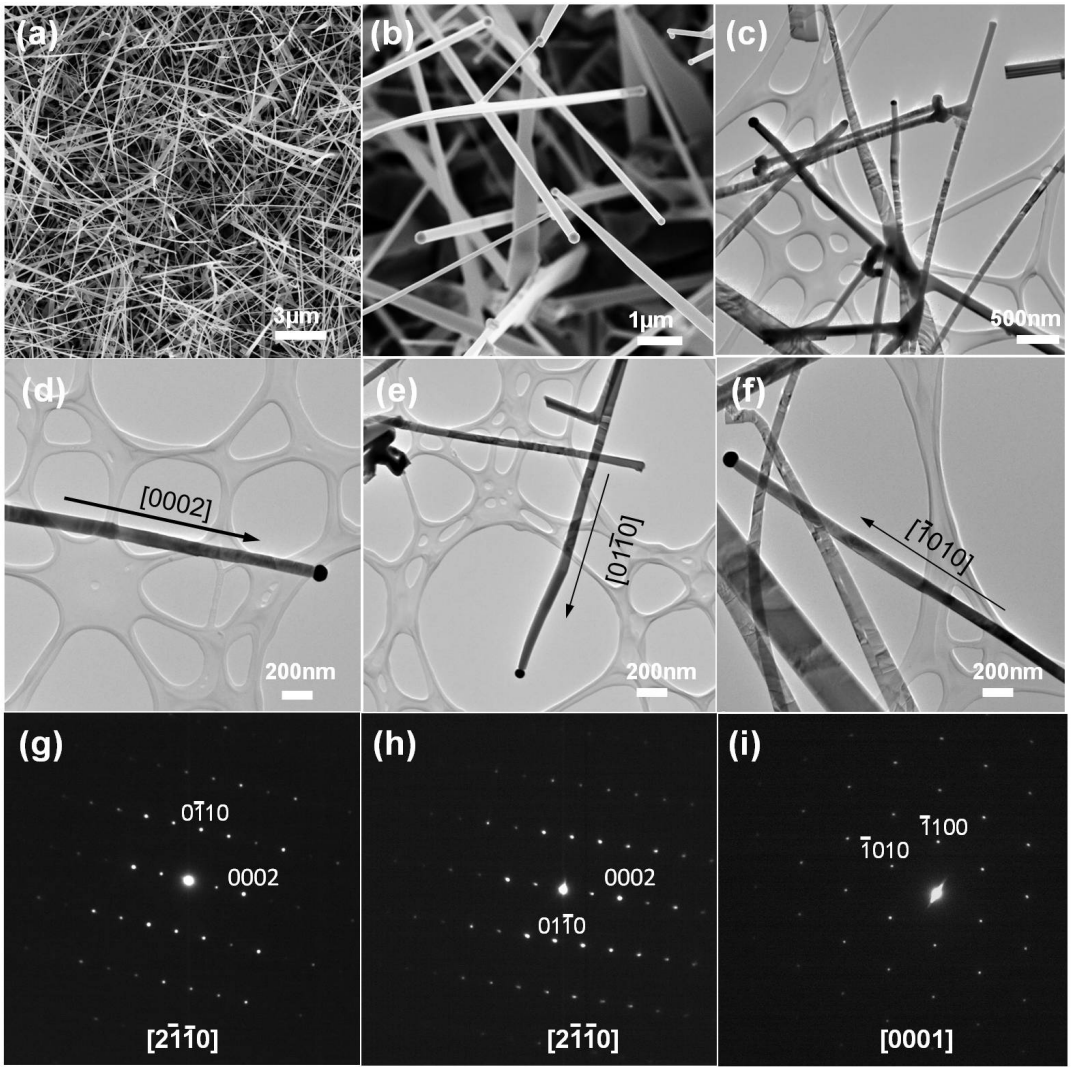

Figure 5.4 (a) and (b) low and high magnification SEM images of CdSe nanostructures synthesized by laser ablation with a higher energy flux. (c) Low magnification TEM image of CdSe nanostructures, showing nanowires, nanobelts and branched structures. (d)~(f) Representative TEM images of CdSe nanowires with growth directions, [0002], [01$\bar{1}$0] and [$\bar{1}$010], respectively.(g)~(i) SEAD patterns recorded from the CdSe nanowires labeled the growth direction in (d)~(f),respectively.

0.35nm could be indexed as (0001) of wurtzite and (111) of zinc blende, respectively. The mixed crystalline structures observed in CdSe nanowires could be attributed to the lower temperature during the ablation. It is well known that CdSe crystallizes in both wurtzite and zinc blende structure and generally stabilizes as zinc blende structure if the fabrication temperature is low[29,30].

SEM images of CdSe nanowires synthesized by laser ablation at 750^{o}C with higher energy flux were shown in Figure 5.4(a) and (b), revealing a high density of CdSe nanostructures with different morphologies. Most of them were observed with gold catalysts sitting on the tips, as shown in the enlarged SEM image in Figure 5.4(b), which confirms the classical VLS mechanism mediated the growth. The results were further confirmed by a typical low-magnification TEM image, as shown in Figure 5.4(c). Several morphologies of CdSe nanostructures, such as straight wires, tapered belts and branched wires, were observed. Considering the objective of core-shell nanowire fabrication, we further focused on the crystal structures of the straight CdSe nanowires. Figure 5.4 (g)~(i) show the SEAD patterns corresponding to the CdSe nanowires in Fig.5.4(d)~(f), respectively. Three different growth directions of CdSe nanowires, i.e., [0002], [01$\bar{1}$0] and [$\bar{1}$010], were determined by indexing the SEAD patterns. No zinc blende CdSe nanowire was observed. Various growth directions of CdSe nanowires originate from the polarity of wurtzite structures, similar to that of ZnO nanowires. The high density and randomly distributed CdSe nanowires with different growth directions, making it an intriguing platform for structural analysis, hinders the exploration of coaxial heterostruture fabrication. A new approach needs to be developed in order to gain an ideal template for shell coating.

5.3.1.2 CdSe nanowires on silicon substrate by thermal evaporation

Figure 5.5(a) and (b) shows the SEM images of the CdSe nanowires collected on silicon substrates. The nanowires exhibited several micrometers in length and very rigid morphology. Regardless of their random orientations on substrate, the nanowires were well separated at low density. Inset of Figure 5.5(a) is a higher magnification SEM image showing that the nanowires were terminated with catalysts. As shown in the cross-section view SEM images (Figure 5.5(b)), the nanowires were directly grown on the micrometer oriented CdSe grains with a thickness of around 2μm. TEM images were also recorded to figure out the crystal structure of CdSe nanowires. The diameters of the nanowires were around 80 nm and, clearly, the growth was

governed by VLS because of the catalysts observed on the tip of nanowire, as shown in Figure 5.5(c). The lattice planar distance was measured as 0.69 nm and the growth direction of CdSe nanowire was then identified as (0001), which is also confirmed by FFT shown in the inset. Unlike the surface of the ZnTe nanowires, no amorphous layer was observed on the surface of the CdSe nanowire. The clean surface, together with the rigidity and low density of the CdSe nanowires, implies the possible homogenous coating and high quality interfaces in the core-shell nanowires.

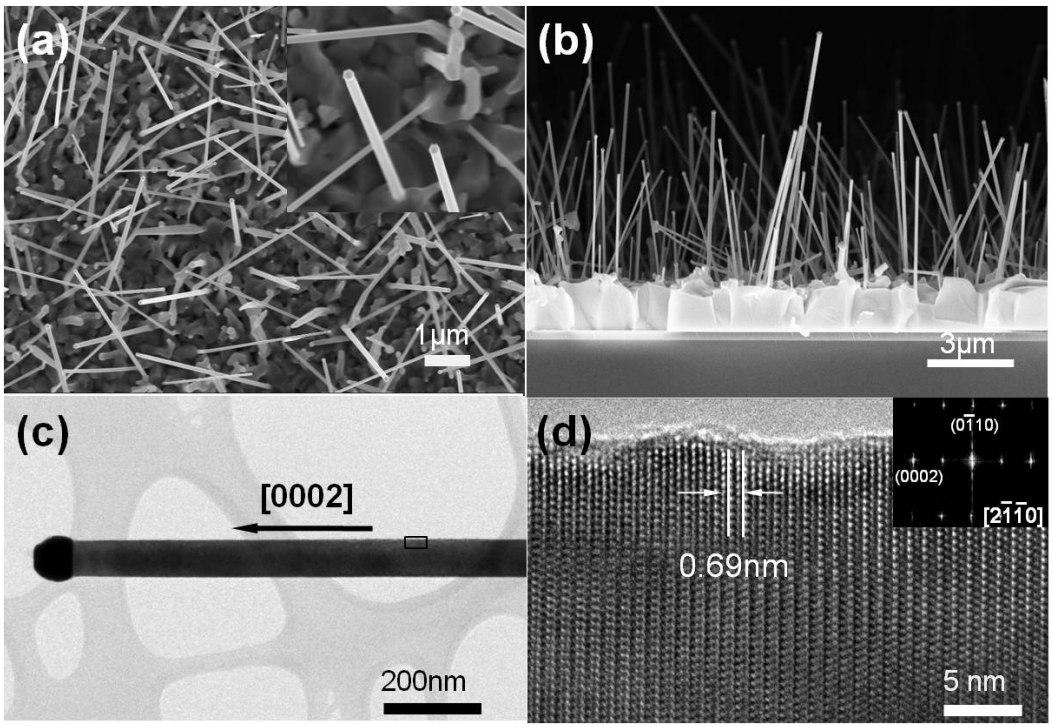

Figure 5.5 (a) SEM image of low density rigid CdSe nanowires synthesized by thermal evaporation. Inset is the high magnification image showing the catalysts on the tip of nanowires. (b)cross-section of CdSe nanowires directly grown on a thick CdSe oriented layer.(c) TEM image of an individual CdSe nanowire with a catalyst on the tip.(d) HRTEM of CdSe nanowire taken from the frame in (c). Inset displays the corresponding FFT of the high magnification image.

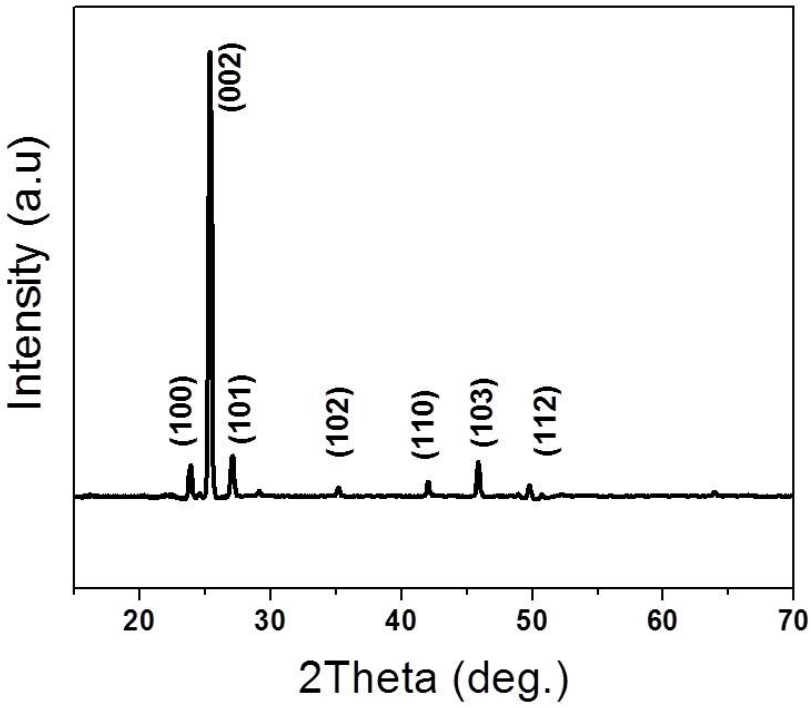

Figure 5.6 XRD pattern of CdSe nanowires collected on silicon substrate.

XRD pattern of the CdSe nanowires grown on silicon substrate was shown in Figure 5.6. A very intense diffraction peak, (002), indicated CdSe product has a *c*-axis preferred orientation. Because a relatively thicker CdSe layer was observed in SEM, we cannot solely attribute this to the *c*-axis growth habit of CdSe nanowires. In fact, similar to ZnO, CdSe naturally crystallizes in wurtzite structures, preferring a *c*-axis growth. Once the furnace is heated to a certain temperature, CdSe is evaporated and the high density vapor in the initial period condensed on the silicon substrate, leading to a *c* oriented thin film on silicon substrate. The thickness of the thin film is determined by the temperature gradient and the amount of the source vapor. Meanwhile, gold catalysts initialize the nanowire growth by using this oriented thin film as a seed layer. This could explain why the CdSe nanowires grown by this method were rigid in this method.

5.3.2 Structure analysis of CdSe/ZnTe core-shell nanowires

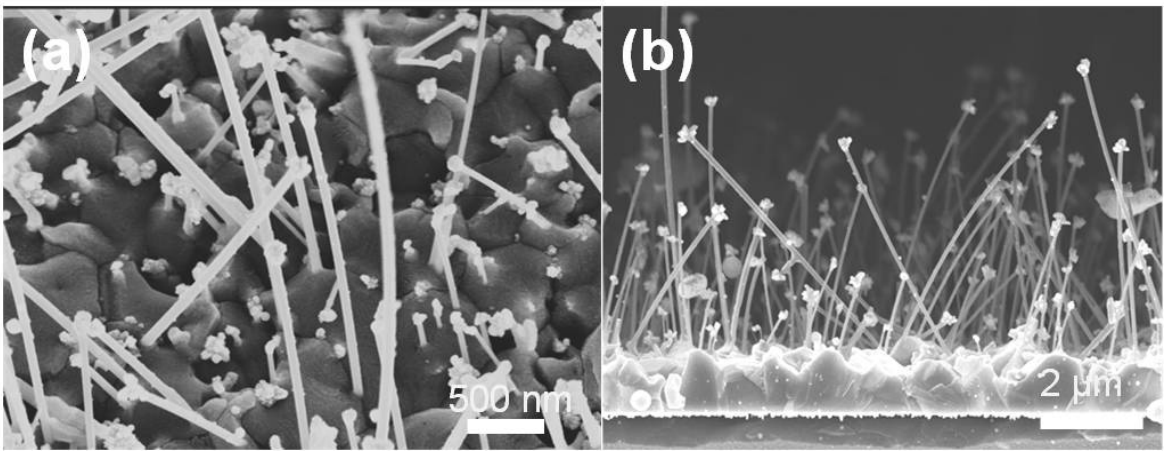

Figure 5.7 SEM images of CdSe/ZnTe core-shell nanowires (a) top-view and (b) cross-section.

Figure 5.7 (a) and (b) represents the top-view and cross-section view of the CdSe nanowire coated with ZnTe by pulsed laser ablation of ZnTe target for 15min. A few small particles covered the catalyst particles on the tips of the nanowires, exhibiting flower-bud morphology. A few nanoparticles were also observed on the surface of nanowires.

Detailed structure characterization was further performed by TEM equipped with nanoprobe EDS. Figure 5.8(a) shows a lower magnification TEM image of several CdSe/ZnTe nanowires. The morphology of coated nanowires presented some nanoparticles on the surface, in good agreement with the observation in SEM images. This presence of these nanoparticles could be attributed to the emission of microscopic particulates from solid targets when irradiated by a laser beam, which is an intrinsic disadvantage in pulsed laser deposition techniques for production of thin films[31]. The geometry for deposition on a substrate that placed at a 90^{o} angle with respect to the target surface in our home-made pulsed laser ablation aggravates the generation of particulates. One representative lower magnification TEM image of a single coated nanowire in Figure5.8 (b) revealed that the nanowire exhibited core-shell geometry, regardless of microscopic particulates on the surface. The interface of core and shell can be easily distinguished by the phase contrast, as highlighted by the dash lines. The core had a diameter of 80nm and the thickness of the shell was around 20nm. To obtain detailed information about the interface, a high resolution TEM image was recorded at the interface area and shown in

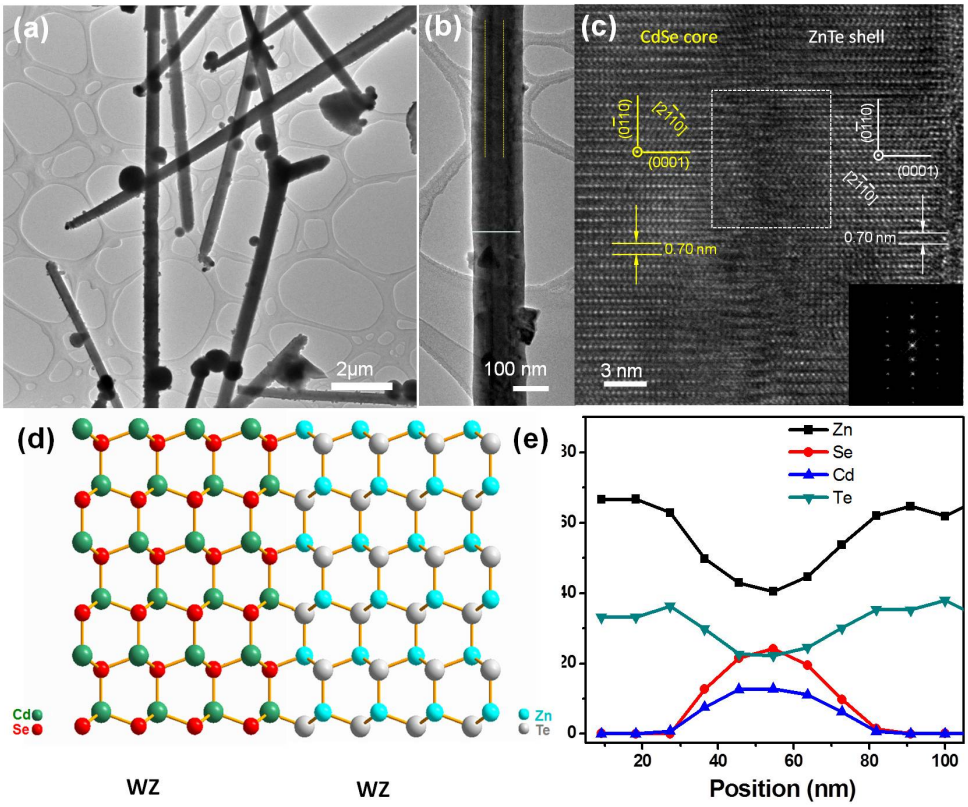

Figure 5.8 (a) Low magnification TEM image of CdSe/ZnTe core-shell nanowires.(b) A representative TEM image of an individual CdSe/ZnTe core-shell nanowire, clearly showing the smooth surface and core-shell geometry.(c) HRTEM images of a typical core-shell interface manifesting the epitaxial growth relationship of $CdSe_{WZ}$ and ZnTe $_{WZ}$; Inset shows the FFT of the area marked as dashed frame ; (c) Ball and stick model of the relaxed CdSe (WZ) /ZnTe (WZ) structure. (d) Nanoprobe EDS scanning along the line marked in(b), suggesting the conformal shelling and absence of interfacial diffusion.

Fig.5.8(c). Most of the lattice fringes of the core and shell along the interface of the nanowire were well matched and continuous, in spite of few dislocations. Further structural analysis revealed that both the core and shell were crystallized in wurtzite structures and an epitaxial growth relationship could be assigned as $(0001)_{CdSe}//(0001)_{ZnTe}$ and $(01\bar{1}0)_{CdSe}//(01\bar{1}0)_{ZnTe}$. The FFT of the area labeled in the white frames across the interface shows one set of diffraction pattern, further confirming the well epitaxial growth between the core and shell. An atomistic model of a wurtzite/wurtzite heterostructure was illustrated in Figure5.8 (d). The Cd and Se atoms have been marked in green and red, for wurtzite CdSe, respectively, while Zn and Te atoms have been marked in cyan and grey, respectively, for wurtzite ZnTe. Owing to the same

wurtzite crystal structure and close lattice parameters, the near identical atom arrangement was demonstrated. A special concern in fabricating core-shell nanowire is the interfacial diffusion between the core and shell. To clarify this in CdSe/ZnTe core-shell nanowire, we employed nanoprobe EDS line scanning along the white line marked in Figure 5.8(a). The element dispersive distribution data, as shown in Figure 5.8 (e), verified that there was no interfacial diffusion occurring between the core and shell in this synthesis condition. Additionally, this result also further confirmed the conformal coating of ZnTe on CdSe nanowires. Note that ZnTe is thermodynamically stable in cubic zinc blende structures and it has barely been reported as hexagonal wurtzite structure in nanocrystalline regime[32]. To our best knowledge, this is the first time to achieve single-crystalline wurtzite ZnTe by taking wurtzite CdSe as the template. From the structure point of view, this interesting observation opens the avenue to explore unique structures such as wurtzite ZnTe nanotubes and 1D CdSe-ZnTe superlattice[33,34]. Moreover, both the core and shell crystallize in wurtzite structure with non-neglected strains along the interface which can generate a piezoelectric field, facilitate the axial charge separation and hence have a potential in other optotronics[35].

5.4 AFM and optical spectra of CdSe nanowire and CdSe/ZnTe core-shell nanowire

A typical AFM and PL images were shown in Figure 5.9(a) and (b). The morphologic information obtained in AFM, catalyst on the tip and smooth surface, is in good agreement with the observation in previous electron microscope analysis. The spectrum with a central peak located at 750 nm, which was collected from the area marked in white circle in Fig.5.9(b), corresponds to the band emission of CdSe. AFM image of CdSe/ZnTe core-shell nanowire exhibited a rough surface, which also confirmed the TEM result. However, no photoluminescence was recorded on the shelled CdSe nanowires. Considering their band energy diagrams, as shown in the Figure 5.9 (e), we attribute this photoluminescence quench to the charge separation induced by the type-II band alignments, similar to that we observed in ZnO/ZnSe and ZnO/ZnS core-shell combinations.

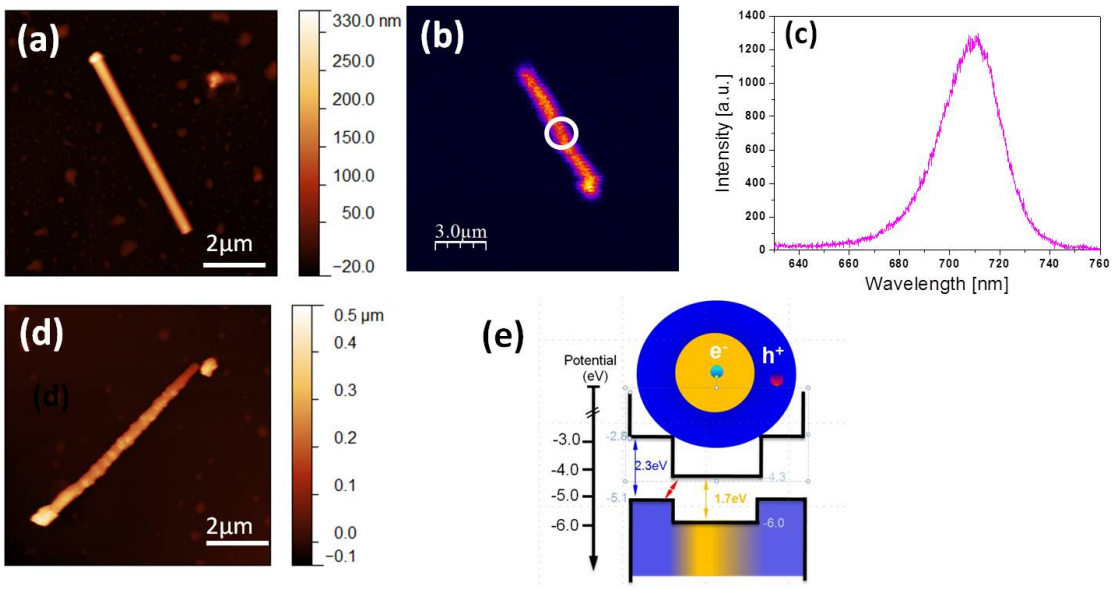

Figure 5.9 (a) and (d) AFM images of an individual CdSe and CdSe/ZnTe core-shell nanowire. (b) PL image of a single CdSe nanowire. (c) A spectrum of CdSe nanowire collected from the area marked by circle in (b). (e) Band diagram of CdSe/ZnTe core-shell nanowires, displaying the charge separation and possible interfacial transition.

5.5 Photovoltaic properties of an individual CdSe/ZnTe core-shell nanowire

Device fabrication

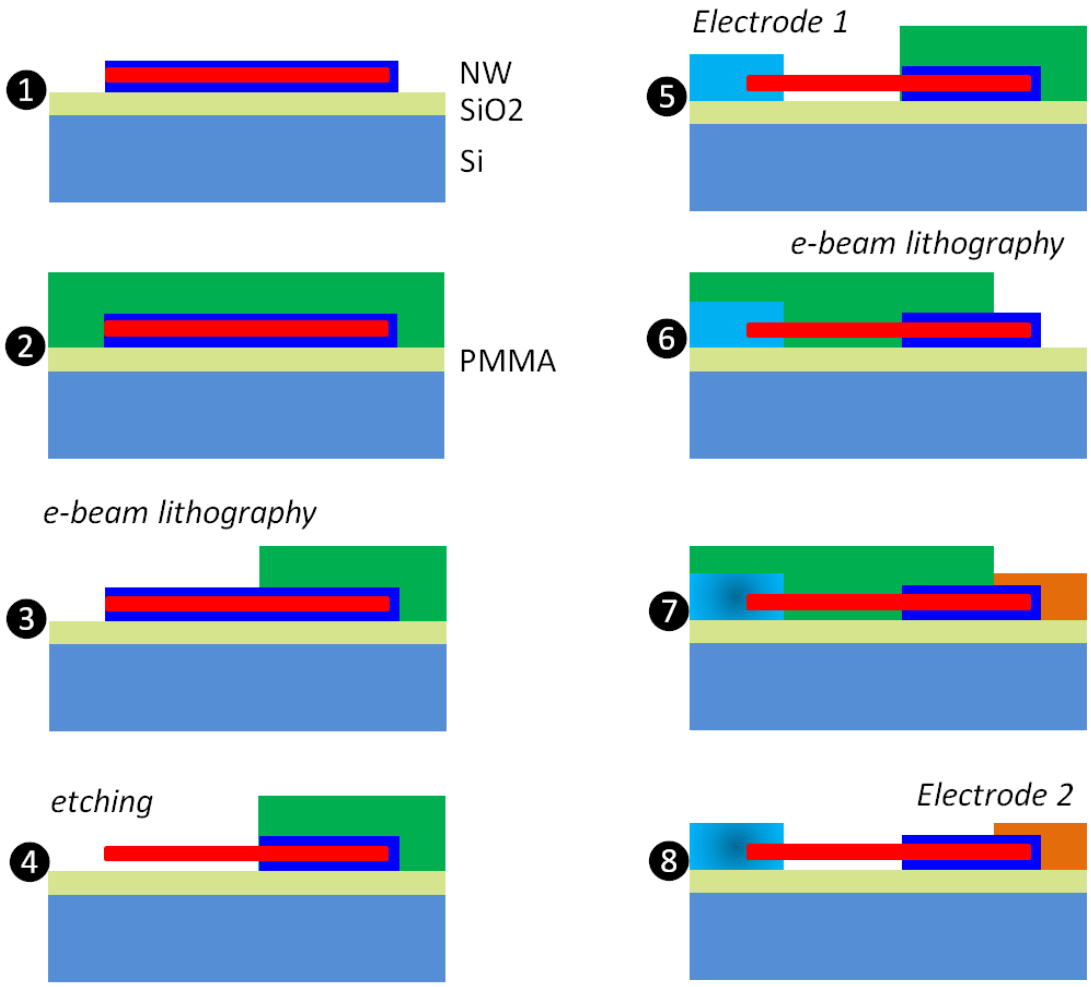

Figure 5.10 Schematics of the procedures for fabricating a PV device based on an individual core-shell nanowire.

To fabricate photovoltaic devices, the CdSe/ZnTe core-shell nanowires were first removed from the collecting substrates and then dispersed in alcohol. The nanowire suspension was then dropped on the silicon substrate, which has a thermal oxide layer and electrodes fabricated by photolithography. Three times EBLs were carried out in the whole process, as illustrated in Figure 5.10. Briefly, two layers of PMMA were spin-coated on the silicon substrates with nanowires, followed by the first time EBL to expose one end of the core-shell nanowire. Chemical etching then was used to remove the shell layer of the nanowires. Here, we used 39%

$FeCl_3$ solution as the etchant, referring to the treatment process for contact interface in CdS/CdTe thin film solar cells[36]. The etch rate was estimated about 3nm/second in our process. After removal of the etching residue and the photoresist, the second EBL was performed followed by metallization. To ensure the Ohmic contact, indium was selected as the electrode to CdSe. Finally, the third EBL, metallization and lift off were conducted. Nickel was used as electrode materials to ZnTe, because of its high work functions. The devices were completed by contacting the leads and the electrodes with silver paste. After stabilized in air for 12 hours, the devices were ready for photovoltaic properties testing.

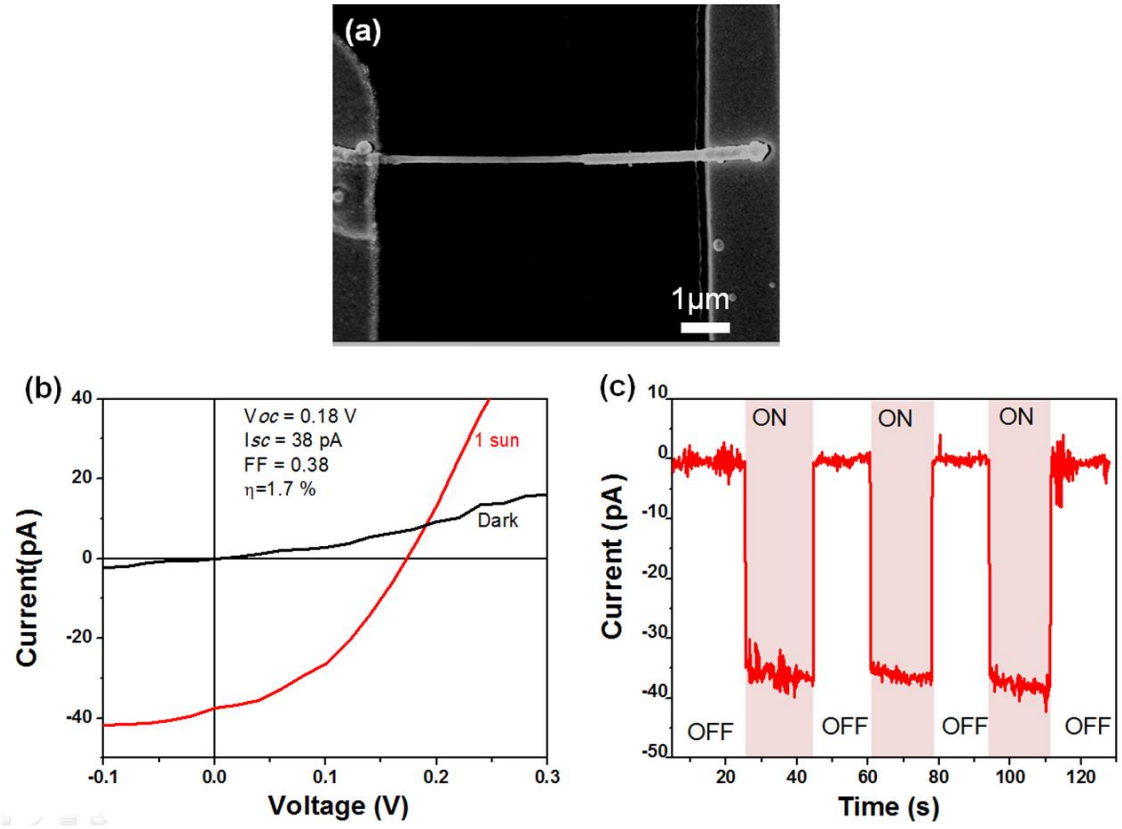

Figure 5.11 (a) SEM image of an individual CdSe/ZnTe core-shell nanowire solar cell. (b) Current-Voltage (*I-V*) characteristics for efficiency extraction. (c) Photoresponse of nanowire device at 0V bias.

Measurement

A standard solar simulator (Newport, Oriel) with calibrated 1-sun intensity was used in conjunction with semiconductor characterization system (Keithley,4200SCS) to obtain all device transport characteristics.

Figure 5.11(a) shows a representative SEM image of photovoltaic device processed from CdSe/ZnTe core-shell nanowire. Upon illumination, core-shell nanowire exhibited obvious photovoltaic behavior. A current-voltage (*I-V*) curve was measured with and without 1 sun light illumination of 100mW/cm^2 light intensity at 25^{o}C. The total efficiency, η, was calculated by dividing the maximum generated power density, P_{out}, by the total incident energy density, P_{in}. The best cell exhibited an open circuit voltage, V_{oc}, of 0.18V, a short-circuit current, *Isc*, of 38 *p*A, and a fill factor of 0.38, which yields an overall solar energy conversion efficiency of 1.7%. Without applying external bias, we also investigated the photoresponse of the devices and the plot was shown in Figure 5.11(c). A stable photocurrent of ~38 *p*A generated and annihilated instantaneously while the illuminated light was on and off, indicating the efficient charge separation and transport between the core and shell.

5.6 Synthesis of CdSe nanowires on muscovite mica substrate by vapor transport method

Experimental To obtain vertically aligned CdSe nanowire array with controllable diameters and density, a seed layer and the catalysts are highly desired. In detail, fresh cleaved muscovite mica substrate (SPI, Grade V-5 research quality) was loaded into electron beam evaporation system (Kurt J. Lesker, PVD75) for CdSe seed layer deposition. CdSe (Alfa Aesar, 99.999% purity, metal basis) loaded in the molybdenum crucible was used as the source materials. The evaporation rate was set as 0.3 Å/s and the substrate temperature was maintained 380^{o}C. After coated with 100nm CdSe thin film, the substrate was transferred to sputtering system (Cressington coating system, 308R) for catalyst deposition. Then the mica substrate with seed layer and catalyst is ready for CdSe nanowire array growth. Subsequently, the growth was carried out in a typical thermal evaporation horizontal tube furnace. As usual, the substrate was located in the downstream in order to collect the products. The gas flow, temperature, pressure, duration of this process were 150 SCCM mixture gases of Ar/H_2 (4:1), 750^{o}C, 760Torr and 20

mins, respectively. The color of the final product on mica varied due to the difference of the nanowire density. In general, the color is black in high density and brownish in lower density, which can be easily distinguished by the naked eye and confirmed by SEM observation later on.

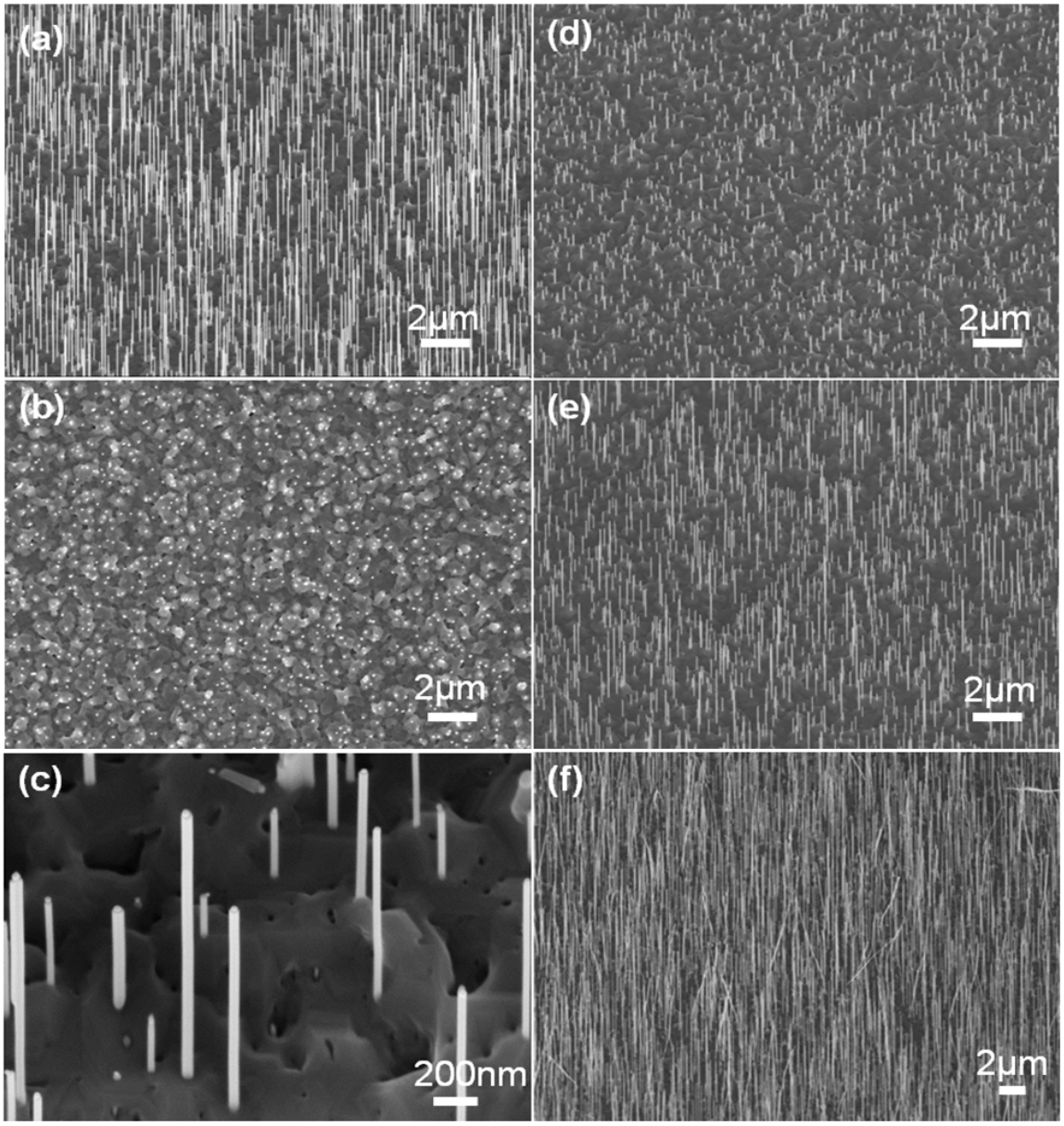

Figure 5.12 (a) 30° tilted view and (b) top-view of SEM images of CdSe nanowire array. (c) High magnification SEM image showing gold catalyst on tips of nanowires. (d)~(f) CdSe nanowire array harvested on different area of mica substrate.

In order to investigate the influence of seed layer and catalysts on the morphologies of the nanowires, other samples were also synthesized for comparison. In detail, mica substrates without the seed layer and with the seed layer in different thicknesses were also used to collect

samples. Gold colloid (Ted Pella) with a diameter of ~200 nm was used to catalyze CdSe nanowire growth for a better understanding of the catalysis process. A TEM copper grid was also used to generate pattern and lower density catalysts.

Figure 5.12 shows representative SEM images of CdSe thin film and CdSe nanowire array obtained on muscovite substrates. Large-area CdSe nanowire array was observed to have vertically grown from substrates, as shown in SEM image (Figure 5.12 (a)) with a 30^{o} titled view. The diameters of nanowires are around 60 nm and show a uniform distribution. Top-view SEM image of CdSe nanowire array was also recorded in Figure 5.12(b), manifesting a well separated alignment normal to substrate. The density of the nanowires was hence calculated as 5 nanowires per μm^2. Large magnification SEM of CdSe nanowires clearly manifested that each nanowire was terminated with a spherical or semi-spherical catalyst on the tip, revealing that the growth of CdSe herein was governed by the classical VLS mechanism. Owning to the temperature gradient, CdSe nanowire array harvested in a one-inch-long mica substrate varied in density, length and diameter. Figure 5.12 (d)~(f) represents the influence of the temperature and location on the morphologies of the CdSe nanowire array. Shorter and lower density of CdSe nanowire array was collected at higher temperature zone ($740^{o}C$), while longer and higher density of nanowire was obtained at zone where temperature was around $720\ ^{o}C$. Array of CdSe nanowire with high aspect ratio, as shown in Figure 5.12 (f), tended to collapse and tangle together under the electrons illuminate in SEM. It should be noted that beyond this temperature window, high density of CdSe nanowires can be obtained at around ~$700^{o}C$ but in a random dispersion, which was not shown here; no nanowire could be observed on mica at the temperature above $750\ ^{o}C$, and the mica will be totally damaged while be loaded in the high temperature zone($760^{o}C$).

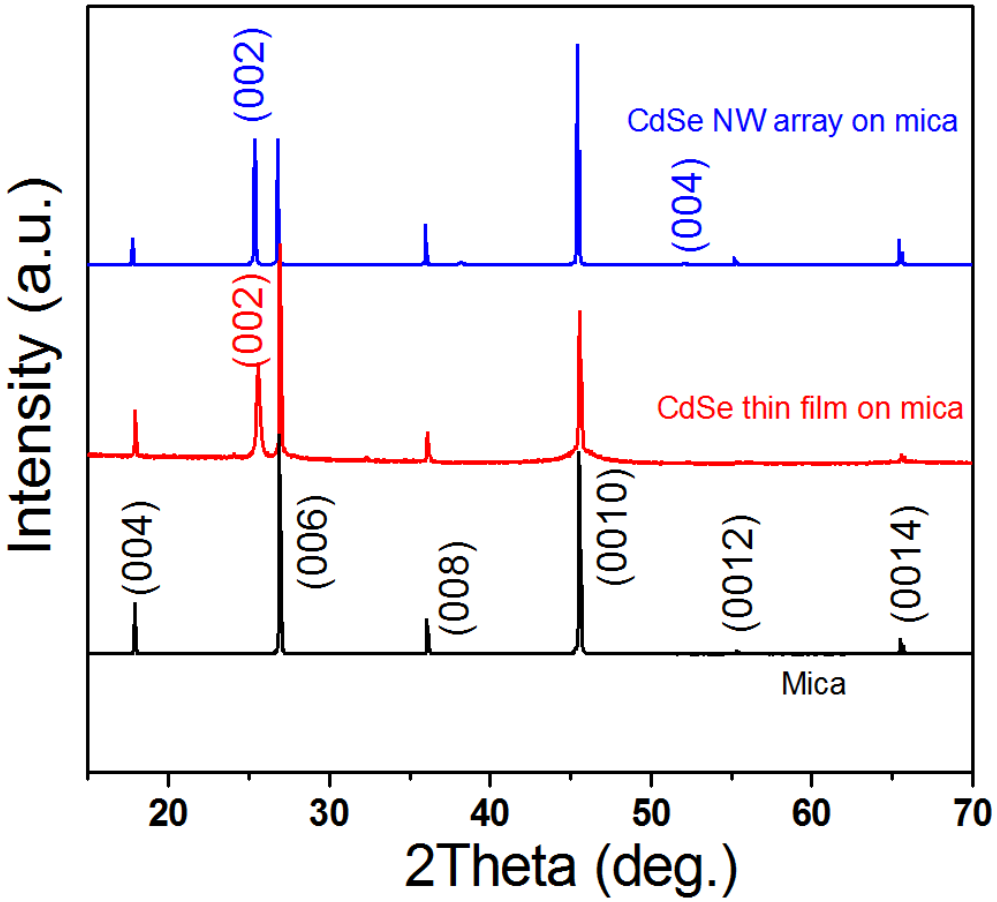

Fig.5.13 XRD patterns of muscovite mica, mica with CdSe seed layer and mica with CdSe nanowire array, clearly showing that both CdSe seed layer and CdSe nanowire array have a preferential growth direction along (002).

XRD patterns of mica, mica with CdSe thin film and mica with nanowires were shown in Figure 5.13. Muscovite mica substrate has very tense peaks that can be identified as (004) to (0014), which indicated the highly crystallinity of the substrate. In contrast, only one additional diffraction peak, which can be identified as (002) of CdSe, was observed in the mica coated CdSe thin film, implying the high oriented growth of the CdSe thin film. A comparable intensity peaks, (002) peak form CdSe and (006) peak of mica substrate, and the large intensity ratio of (002) and (004) peaks form CdSe, suggesting that the nanowires we obtained were preferentially grown along *c*-axis.

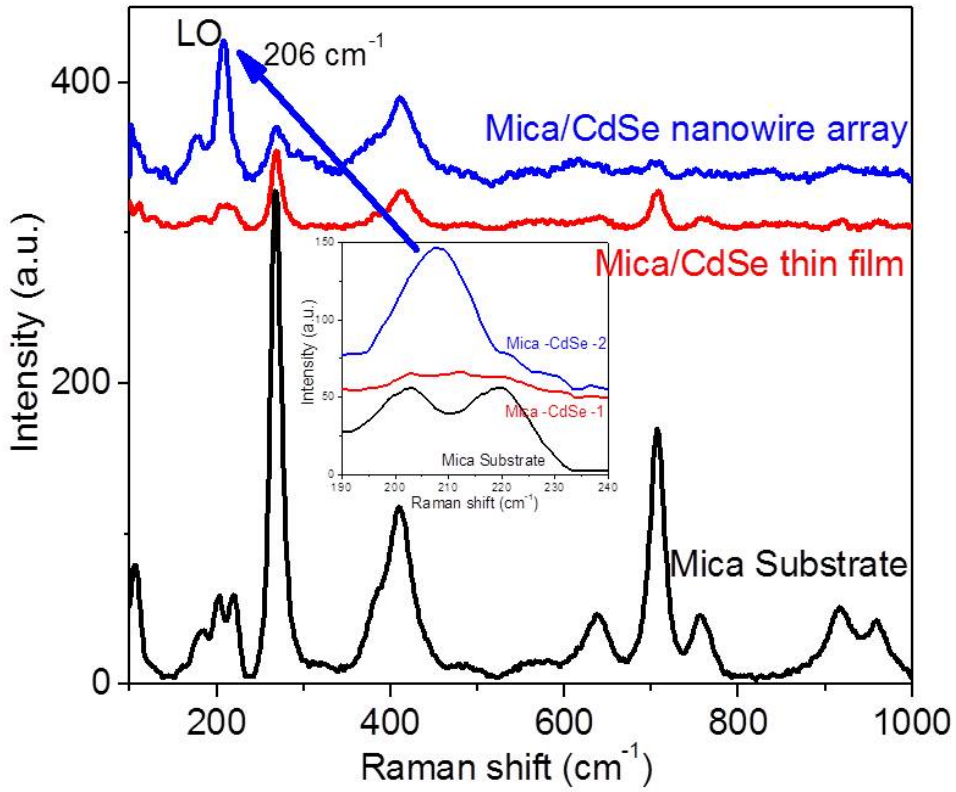

Figure 5.14 Raman spectra from muscovite mica, mica with CdSe seed layer and mica with CdSe nanowire array, respectively. Inset shows large magnification section to highlight the LO mode of nanowire located at 206 cm^{-1}.

The crystal structures of the mica, mica with CdSe thin film and nanowire were further investigated by Raman spectroscopy. Note that the phonon frequencies of the second order longitudinal optical (2LO) mode of CdSe nanowire array, which is supposed to be located at 418.8 cm-1, could be overlapped by that of the mica substrate (Figure 5.14). However, the peak centered at 206cm^{-1} can be indexed to the longitudinal optical phonon (LO) of CdSe nanowires. A little deviation to that of the corresponding bulk materials could arise from the lattice contraction and phonon confinement[37].

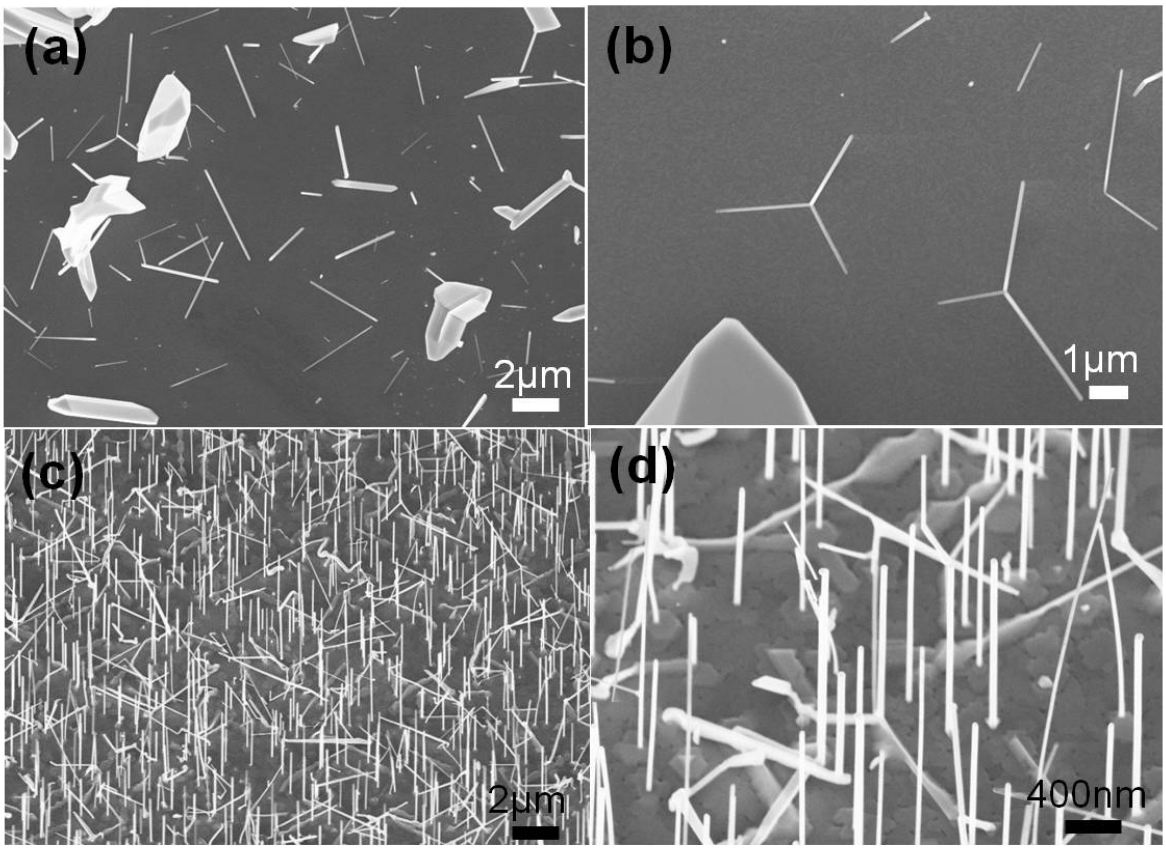

Figure 5.15 (a) and (b)SEM images of CdSe nanostructures collected on muscovite mica without any seed layer and catalysts.(c)and(d) low and higher magnification SEM images of CdSe nanowires obtained on mica substrate with 150 nm CdSe seed layer.

Figure 5.15 (a) and (b) display the SEM images of CdSe nanostructures on a fresh cleaved mica substrate. Only few CdSe nanowires varied in diameter were found to randomly distribute on mica, as well as some micrometers CdSe crystals. Interestingly, several tripod nanocrystals were also obtained on bared mica substrate, similar to the recent report[38]. These observations implied that no vertically aligned nanowire array could be achieved without any further modification of the freshly cleaved mica substrates. It is also found that the thickness of CdSe seed layer deposited on mica through *e*-beam evaporation is crucial in obtaining a well-aligned CdSe nanowire array. Figure 5.15(c) and (d) presents low and high magnification SEM images of the CdSe nanowire array grown on mica with a 150nm-thick CdSe seed layer. Obviously, the vertical alignment of the nanowire was not as good as the one achieved on the 50nm-thick CdSe coated mica substrates.

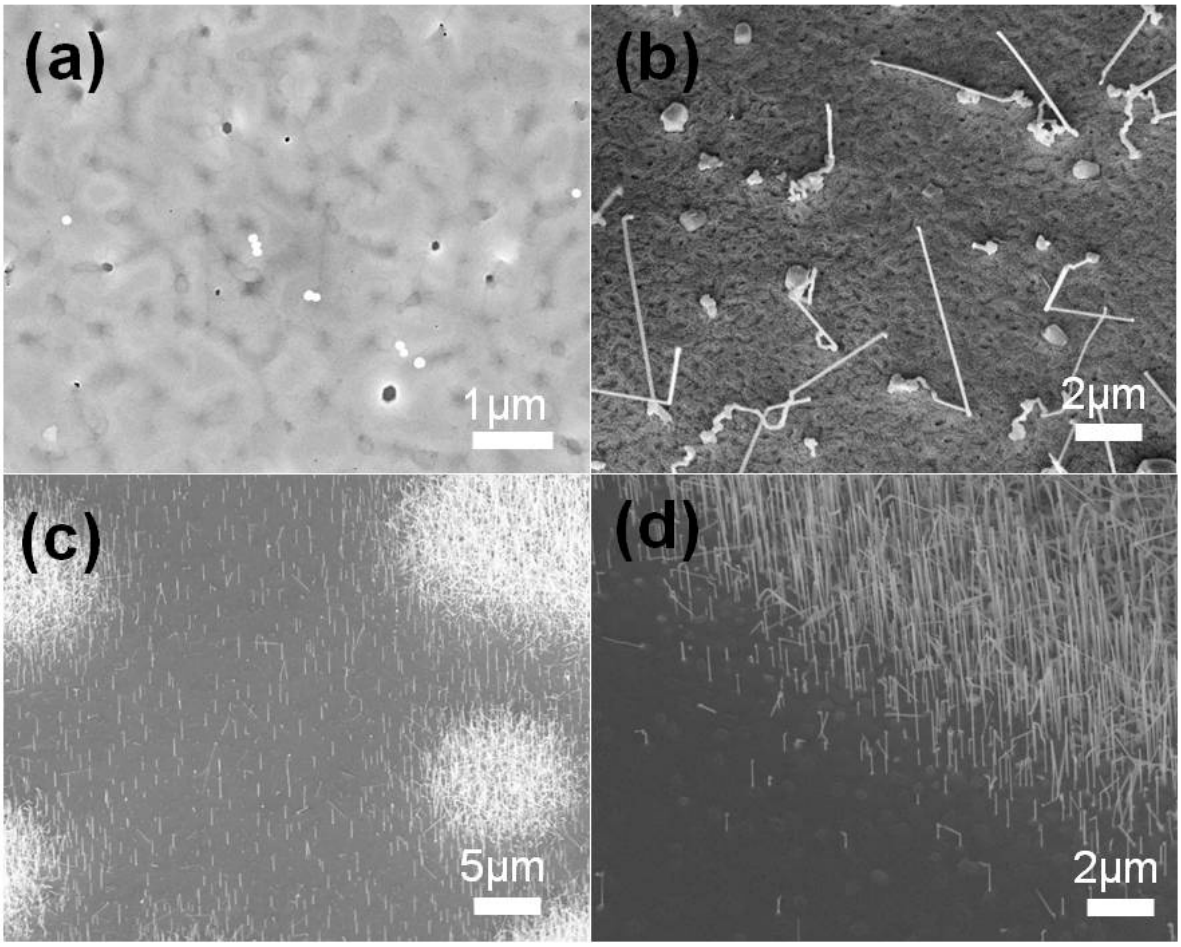

Figure 5.16 SEM images of (a) 200nm gold colloids dispersed on CdSe seed layer coated mica substrate. (b) CdSe nanostructures catalyzed by gold colloids. (c)and(d) low and higher magnification SEM images of CdSe nanowires with patterned catalysts via a TEM copper grid.

Different types of catalysts were used to initialize the CdSe nanowire growth. Figure 5.16(a) is the SEM image of gold colloids deposited on CdSe thin film/mica. The diameter of the gold colloid is around 200 nm and some of them still aggregated together. The morphologies of CdSe nanowire catalyzed by colloid gold were shown in Figure 5.16(b). Definitely, no alignment of nanowire was observed. All nanowires exhibit curved shape at the initial stage and then straight in the top section. In the further experiments, we also realized that the density of catalyst, i.e., the thickness of the metal film, was a crucial factor in achievement of aligned CdSe nanowire array. Because the edge of the copper grid (pattern mask) is not perfectly smooth, a few metal nanoparticles could be diffused to the area near to the edge of the patterns. Vertically aligned

CdSe nanowire with small diameters was hence observed on the edge of the patterns, as shown in Figure 5.16(c) and (d). In the area with thicker gold catalysts, however, the alignment did not sustain anymore and longer, higher density and tangled CdSe nanowires were observed. Meanwhile, we also conducted the similar growth using mica substrate with CdSe seed layer but without any catalyst. However, no nanowire was collected, which evidently highlights the importance of the catalyst.

All the observations about catalysts and seed layer implied that the seed layer with an appropriate thickness and lower density of catalysts are the two important parameters in fabrication of a vertically-aligned array of CdSe nanowire. The whole process actually involved two significant epitaxial strategies, i.e., van der Waals epitaxy and homoepitaxy. Generally, epitaxy between two materials requires the small lattice mismatch and close thermal expansion coefficient. However, the interface of the van der Waals epitaxial heterojunction between the material and substrate is controlled by van der Waals interaction instead of chemical bonding. Unlike traditional heteroepitaxy, this permits the release of the train induced by lattice mismatch and then enables the growth of monocrystalline film from various semiconductors, regardless of their lattice mismatching to the substrates[39-41]. Muscovite mica, with a layered structure and inert cleavage surface, is a popular substrate to facilitate van de Waals epitaxy of monocrystalline epilayer[42,43]. The CdSe thin film deposited on mica by *e*-beam evaporation show smooth surface and high orientation is obvious an epilayer, which was confirmed XRD data. Still, the strain in the epilayer could not be entirely released while the thickness increase, resulting in slight misorientation of the seed layer. This could explain the alignment of nanowire array obtained on the 150 nm seed layer is poor compared to that obtained on the 50 nm seed layer. The process of CdSe nanowire array directly grown from CdSe epilayer is a typical homoepitaxy. Without any seed layer, i.e., epilayer, the nanowires and tripod nanocrystallines were still achieved but in poor quantity. The whole process is still governed by Van der Waals epitaxial. Yet, the detailed underlying mechanism behind is not very clear so far. Recent papers claimed that it was a general route to obtain II-VI tripod nanocrystals by using muscovite mica as collecting substrates[38]. We attempted to control the diameters of CdSe nanowires by controlling the catalyst size, especially using gold colloids, which is a universe way in controlling the diameters of most oxides and semiconducting nanowires[44,45]. Surprisingly, this strategy did not function well in the case of CdSe nanowires array growth. We attribute the failure to i) the solvent for stabilizing

gold particles passivated/contaminate the surface of CdSe epitaxy layer; ii) gold particles are also covered by surfactant, which hinders the adhesion of gold nanoparticles on CdSe layer. Notably, the latter reason could be responsible for the initial curved morphologies of the nanowires. It is interesting to find that the vertical alignment of nanowire occurred only at low density catalysts. Technically, thin layer of catalyst tends to aggregate as bigger particles at higher temperature, leading to nanowires with larger diameters. However, CdSe is a material that is easy to sublime; thus, the catalyst assisted growth may be initialized before aggregation, given the fact that the growth could be initialized at 450^{o}C in section 5.1. Numerous catalysts have likelihood to interfere each other and lose the possible homoepitaxy. It should be pointed out that there is still much room for controlling the diameters and density of CdSe nanowire in our approach. For example, a novel catalyst generating system for fabricate aerosol gold nanoparticles[46], which is well-known for III-V nanowire growth, could be adapted to provide better controllability.

In fact, vertically aligned CdSe nanowire array directly grown on muscovite mica substrate was recently reported[47]. However, the surface of freshly cleaved mica requires surface modification by poly-l-lysine to enhance the quality of nanowire. In addition, the yield is relatively low and the density and diameters of the nanowire are difficult to control. More importantly, the integration of the nanowire array with substrate as an electrical unit confronts big challenges, because the muscovite mica is naturally insulating. By contrast, our approach using CdSe seed layer and catalysts to grow nanowire allows for size and density controllability and the direct integration in existing MEMS, offering more degrees of freedom of and a useful platform to investigate the array of CdSe nanowire physical properties.

5.7 Conclusion

In summary, we have been able to synthesize wurtzite CdSe and zinc blende ZnTe nanowires on silicon substrates by thermal evaporation or pulsed laser ablation. Especially, by combining van de Waals epitaxy and homoepitaxy, a vertically aligned CdSe nanowire array was successfully achieved on muscovite mica substrates, where a layer of CdSe thin film and metal thin film were deposited as seed layer and catalysts, respectively. By using the as-grown ZnTe and CdSe nanowires as the templates, ZnTe/CdSe and CdSe/ZnTe coaxial nanoheterostrutures have been sought via laser ablation of a target. It turned out that ZnTe/CdSe heterojunction exhibited a rough surface with CdSe nanoislands, either in wurtzite or zinc blende, partly because of the oxides layer in ZnTe nanowires. CdSe/ZnTe core-shell nanowires exhibited a sharp interface between the core and shell, and both the core and shell crystallize in wurtzite structure. An epitaxial relationship, $(0001)_{CdSe}//(0001)_{ZnTe}$ and $(01\bar{1}0)_{CdSe}//(01\bar{1}0)_{ZnTe}$, could be indentified in the CdSe and ZnTe in the core-shell structure. The photovoltaic device based on a single CdSe/ZnTe core-shell nanowire was also fabricated, demonstrating an overall energy conversion efficiency of ~1.7%. Considering the well-established doping capability of *n*-type CdSe and *p*-type ZnTe, there is still much room to improve the efficiency by optimizing the device configuration and materials modification. For instance, core-multiple shells nanostructure, in analogy to tandem-cell structures, could be exploited by taking advantage of lattice-matched interfaces, core-shell geometry and aligned morphology. The intriguing growth relationship observed in the coaxial heterostructure, offer the opportunity of manipulating the crystalline structure of the shell by controlling that of the core, regardless of the equilibrium crystalline structure of the shell. These findings in this section also provided the possibility to understand the coupling effects of photovoltaic and piezoelectric in low dimensionality and harvesting hybrid energy in either array or single core-shell nanowire.

Reference

1 E. C. Garnett and P. D. Yang, Journal of the American Chemical Society **130**, 9224 (2008)

2 M. D. Kelzenberg, D. B. Turner-Evans, B. M. Kayes, M. A. Filler, M. C. Putnam, N. S. Lewis, and H. A. Atwater, Nano Letters **8**, 710 (2008)

3 L. Tsakalakos, J. Balch, J. Fronheiser, B. A. Korevaar, O. Sulima, and J. Rand, Applied Physics Letters **91**, (2007)

4 T. J. Kempa, B. Z. Tian, D. R. Kim, J. S. Hu, X. L. Zheng, and C. M. Lieber, Nano Letters **8**, 3456 (2008)

5 J. E. Allen, E. R. Hemesath, D. E. Perea, J. L. Lensch-Falk, Z. Y. Li, F. Yin, M. H. Gass, P. Wang, A. L. Bleloch, R. E. Palmer, and L. J. Lauhon, Nature Nanotechnology **3**, 168 (2008)

6 P. T. N. Hieu, Y. L. Chang, I. Shih, and Z. T. Mi, Ieee Journal of Selected Topics in Quantum Electronics **17**, 1062 (2011)

7 Y. P. Dan, K. Seo, K. Takei, J. H. Meza, A. Javey, and K. B. Crozier, Nano Letters **11**, 2527 (2011)

8 J. Y. Tang, Z. Y. Huo, S. Brittman, H. W. Gao, and P. D. Yang, Nature Nanotechnology **6**, 568 (2011)

9 R. Cohen, V. Lyahovitskaya, E. Poles, A. Liu, and Y. Rosenwaks, Applied Physics Letters **73**, 1400 (1998)

10 Y. Rosenwaks, L. Burstein, Y. Shapira, and D. Huppert, Applied Physics Letters **57**, 458 (1990)

11 M. W. Wang, M. C. Phillips, J. F. Swenberg, E. T. Yu, J. O. McCaldin, and T. C. McGill, Journal of Applied Physics **73**, 4660 (1993)

12 S. Aldallal, Physica Status Solidi a-Applied Research **44**, 183 (1977)

13 A. K. Pal, A. Mondal, and S. Chaudhuri, Vacuum **41**, 1460 (1990)

14 D Ding S Wang, R Scott, J Chen, M DiNezza, X Liu, J Furdyna, Y H Zhang, 2009 34th IEEE Photovoltaic Specialists Conference PVSC (2009) 001654 (2009)

15 P. Gashin, A. Focsha, T. Potlog, A. V. Simashkevich, and V. Leondar, Solar Energy Materials and Solar Cells **46**, 323 (1997)

16 C. Y. Chen, C. T. Cheng, J. K. Yu, S. C. Pu, Y. M. Cheng, P. T. Chou, Y. H. Chou, and H. T. Chiu, Journal of Physical Chemistry B **108**, 10687 (2004)

17 S. Kaniyankandy, S. Rawalekar, S. Verma, and H. N. Ghosh, Journal of Physical Chemistry C **115**, 1428 (2011)

18 J. A. Goebl, R. W. Black, J. Puthussery, J. Giblin, T. H. Kosel, and M. Kuno, Journal of the American Chemical Society **130**, 14822 (2008)

19 C. T. Cheng, C. Y. Chen, C. W. Lai, W. H. Liu, S. C. Pu, P. T. Chou, Y. H. Chou, and H. T. Chiu, Journal of Materials Chemistry **15**, 3409 (2005)

20 Y. M. Park, R. Andre, J. Kasprzak, L. S. Dang, and E. Bellet-Amalric, Applied Surface Science **253**, 6946 (2007)

21 Q. F. Meng, C. B. Jiang, and S. X. Mao, Journal of Crystal Growth **310**, 4481 (2008)

22 E. Janik, P. Dluzewski, S. Kret, A. Presz, H. Kirmse, W. Neumann, W. Zaleszczyk, L. T. Baczewski, A. Petroutchik, E. Dynowska, J. Sadowski, W. Caliebe, G. Karczewski, and T. Wojtowicz, Nanotechnology **18**, (2007)

23 L. Li, Y. W. Yang, X. H. Huang, G. H. Li, and L. D. Zhang, Journal of Physical Chemistry B **109**, 12394 (2005)

24 Q. F. Meng, C. B. Jiang, and S. X. Mao, Applied Physics Letters **94**, (2009)

25 S. Y. Li, Y. Jiang, D. Wu, L. Wang, H. H. Zhong, B. Wu, X. Z. Lan, Y. Q. Yu, Z. B. Wang, and J. S. Jie, Journal of Physical Chemistry C **114**, 7980 (2010)

26 S. Y. Li, Y. Jiang, D. Wu, B. B. Wang, Y. G. Zhang, J. W. Li, X. M. Liu, H. H. Zhong, L. Chen, and J. S. Jie, Applied Physics a-Materials Science & Processing **102**, 469 (2011)

27 H. Kirmse, W. Neumann, S. Kret, P. Dłużewski, E. Janik, G. Karczewski, and T. Wojtowicz, physica status solidi (c) **2**, 3780 (2008)
28 K. Davami, H. M. Ghassemi, R. S. Yassar, J. S. Lee, and M. Meyyappan, Chemphyschem **13**, 347 (2012)
29 Q. M. Yang, J. Zhao, M. Guan, C. Liu, L. J. Cui, D. J. Han, and Y. P. Zeng, Applied Surface Science **257**, 9038 (2011)
30 C. X. Shan, Z. Liu, and S. K. Hark, Applied Physics Letters **87**, (2005)
31 E. Agostinelli, S. Kaciulis, and M. Vittori-Antisari, Applied Surface Science **156**, 143 (2000)
32 J. Zhang, S. Y. Jin, H. C. Fry, S. Peng, E. Shevchenko, G. P. Wiederrecht, and T. Rajh, Journal of the American Chemical Society **133**, 15324 (2011)
33 S. C. Andrews, M. A. Fardy, M. C. Moore, S. Aloni, M. J. Zhang, V. Radmilovic, and P. D. Yang, Chemical Science **2**, 706 (2011)
34 B. B. Cao, T. T. Shi, S. J. Zheng, Y. H. Ikuhara, W. L. Zhou, D. Wood, M. Al-Jassim, and Y. F. Yan, Journal of Physical Chemistry C **116**, 5009 (2012)
35 F. Boxberg, N. Sondergaard, and H. Q. Xu, Nano Lett. **10**, 1108 (2010)
36 R.G. Dhere T.A. Gessert, J.N. Duenow, J.V. Li, S.E. Asher, and M.R. Young "Comparison of CdS/CdTe superstrate and substrate devices
fabricated with a ZnTe:Cu contact interface ", in *Photovoltaic Specialists Conference (PVSC), 2010 35th IEEE* (2010), pp. 000335
37 M. Mohr and C. Thomsen, Nanotechnology **20**, (2009)
38 M. I. B. Utama, Q. Zhang, S. F. Jia, D. H. Li, J. B. Wang, and Q. H. Xiong, Acs Nano **6**, 2281 (2012)
39 S. Steinberg, W. Ducker, G. Vigil, C. Hyukjin, C. Frank, M. Z. Tseng, D. R. Clarke, and J. N. Israelachvili, Science **260**, 656 (1993)
40 D. S. Kong, W. H. Dang, J. J. Cha, H. Li, S. Meister, H. L. Peng, Z. F. Liu, and Y. Cui, Nano Letters **10**, 2245 (2010)
41 A. Koma, Journal of Crystal Growth **201**, 236 (1999)
42 K. Ueno, K. Saiki, T. Shimada, and A. Koma, Journal of Vacuum Science & Technology a-Vacuum Surfaces and Films **8**, 68 (1990)
43 H. Enomoto, T. Kawano, M. Kawaguchi, Y. Takano, and K. Sekizawa, Japanese Journal of Applied Physics Part 2-Letters **43**, L123 (2004)
44 A. I. Hochbaum, R. Fan, R. R. He, and P. D. Yang, Nano Letters **5**, 457 (2005)
45 D. S. Kim, R. Scholz, U. Gosele, and M. Zacharias, Small **4**, 1615 (2008)
46 M. E. Messing, K. A. Dick, L. R. Wallenberg, and K. Deppert, Gold Bulletin **42**, 20 (2009)
47 M. I. B. Utama, Z. P. Peng, R. Chen, B. Peng, X. L. Xu, Y. J. Dong, L. M. Wong, S. J. Wang, H. D. Sun, and Q. H. Xiong, Nano Lett. **11**, 3051 (2011)

Chapter 6 Conclusion and Perspective

In this dissertation, my focus is on the use of II-VI core-shell nanowire, both single and array, in photovoltaic applications, with a special emphasis on materials synthesis and structure analysis.

ZnO nanowire arrays have been employed in nanowires solar cells as antireflective layer, carrier transport, and received extensively attraction in the last decades. Nonetheless, the optical and electrical properties of ZnO nanowire array synthesized by different techniques have not been systematically studied. In Chapter 2, ZnO nanowire arrays have been synthesized by CVD on different substrate and their properties were compared by photoluminescence spectrum of arrays and photoconductivity/ photoresponse of individual nanowire devices. These studies offered a deep insight to the potential application of ZnO nanowire array in solar cells. In addition, two interesting morphologies of ZnO nanostructures, i.e., nanourchins and ultra-wide nanobelts, were also reported, which enriched the family of ZnO nanomaterials.

In the type-II band alignment functioned in DSSCs and QDSSCs, the absorbers, i.e., dye molecular or narrow bandgap semiconductor QDs, were coupled with a wide bandgap semiconductor. In chapter 3, two type-II combinations constructed by wide band gap materials, ZnO/ZnSe and ZnO/ZnS, were synthesized in arrays of core-shell nanowires on ITO substrates. The photovoltaic devices based on a type-II ZnO/ZnS core-shell nanowire array have been demonstrated, which suggested the potential to use wide band gap semiconductors as active materials in solar energy harvesting.

One major concern of core-shell nanowires solar cells is the interfacial recombination that originates from the low-quality interface between the core and shell. In Chapter 5, a lattice matching II-VI combination of CdSe/ZnTe was selected to construct core-shell nanowires. ZnTe and CdSe nanowires were synthesized to act as templates for following shell deposition, respectively. It turned out that CdSe nanocrystals and high density defects epilayer was formed over ZnTe nanowire, which can be attributed the native oxide layer and the random distribution of ZnTe nanowires. A conformal ZnTe shell with smooth external surface was revealed to

epitaxially grow over CdSe nanowires. A photovoltaic device has been demonstrated in an individual CdSe/ZnTe core-shell nanowire, exhibiting an open-circuit voltage, V_{oc}, of 0.18V, a short-circuit current, *Isc*, of 38 *p*A, a fill factor of 0.38, and an overall solar energy conversion efficiency of 1.7%. Moreover, a controllable synthesis of CdSe nanowire array on muscovite mica substrate was discussed, opening the avenue to exploit a three dimension nanowire array device for hybrid energies harvesting.

Several works have to be done in the future in order to develop nanowire solar cells with comparable efficiency to that of the current planar photovoltaic device.

To improve the overall conversion efficiency, both theoretical and experimental work on optical engineering, electrical manipulation, and material and device design need to be conducted. For optical engineering, future work will need to be centered on optimization of various dimensional parameters including the length, diameter, arrangement, fill ratio, and unique feature, to further tailor the light absorption spectrum and reduce the material consumption. Detailed investigations of the nanowire arrangement would clarify the above mentioned confusions and determine the optimal arrangement. Along with the effort to develop novel architecture, theoretical calculation and modeling on the optical coupling have to be carried out on specific materials in different geometry, which may predict the optimal nanowire diameter to achieve maximum photons absorption. So far, apart from silicon nanowires and nanoholes array, there is little theoretical work focused on other nanostructures, which hinders the development of other nanowire array PV devices beyond silicon. In addition, to push the envelope of the photons collection, traditional concepts, such as antireflective coating, could also be incorporated in the nanowire array PV devices, even though the nanowire array itself could reduce the reflection.

In term of charge separation and collection, coaxial nanocable array has demonstrated advantages over the axial and planar devices. Furthermore, controllability of doping concentration and homogeneity, which is curial in tuning the bandgap and the electrical properties of materials, has to be fully explored to achieve broader absorption spectrum and lower series resistance. Additionally, novel device design is highly expected to reduce the shunt and contact resistance, which could further improve the charge collection.

Currently, the lack of low-cost, large-size and high-quality nanowire array still remains an obstacle. Thus, more effort is required to explore new synthetic routes in order to obtain large-

area nanowire arrays. Given the multiple functionalities of the nanowire and their possible coupling effects, such as piezoelectricity and thermoelectricity, the use of nanowire arrays for three dimensional PV applications is still a burgeoning field with outstanding potential.

Appendix:Copyright Permissions

JOHN WILEY AND SONS LICENSE
TERMS AND CONDITIONS

May 29, 2012

This is a License Agreement between KAI WANG ("You") and John Wiley and Sons ("John Wiley and Sons") provided by Copyright Clearance Center ("CCC"). The license consists of your order details, the terms and conditions provided by John Wiley and Sons, and the payment terms and conditions.

All payments must be made in full to CCC. For payment instructions, please see information listed at the bottom of this form.

License Number	2870580746216
License date	Mar 16, 2012
Licensed content publisher	John Wiley and Sons
Licensed content publication	Advanced Materials
Licensed content title	Direct Growth of Highly Mismatched Type II ZnO/ZnSe Core/Shell Nanowire Arrays on Transparent Conducting Oxide Substrates for Solar Cell Applications
Licensed content author	Kai Wang,Jiajun Chen,Weilie Zhou,Yong Zhang,Yanfa Yan,John Pern,Angelo Mascarenhas
Licensed content date	Sep 3, 2008
Start page	3248
End page	3253
Type of use	Dissertation/Thesis
Requestor type	Author of this Wiley article
Format	Electronic
Portion	Full article
Will you be translating?	No
Order reference number	
Total	0.00 USD
Terms and Conditions	

TERMS AND CONDITIONS

This copyrighted material is owned by or exclusively licensed to John Wiley & Sons, Inc. or one of its group companies (each a "Wiley Company") or a society for whom a Wiley Company has exclusive publishing rights in relation to a particular journal (collectively WILEY"). By clicking "accept" in connection with completing this licensing transaction, you agree that the following terms and conditions apply to this transaction (along with the billing and payment terms and conditions established by the Copyright Clearance Center Inc., ("CCC's Billing and Payment terms and conditions"), at the time that you opened your Rightslink account (these are available at any time at http://myaccount.copyright.com)

AMERICAN INSTITUTE OF PHYSICS LICENSE TERMS AND CONDITIONS

May 29, 2012

All payments must be made in full to CCC. For payment instructions, please see information listed at the bottom of this form.

License Number	2870591074329
Order Date	Mar 16, 2012
Publisher	American Institute of Physics
Publication	Applied Physics Letters
Article Title	Synthesis and photovoltaic effect of vertically aligned ZnO/ZnS core/shell nanowire arrays
Author	K. Wang, J. J. Chen, Z. M. Zeng, J. Tarr, et al.
Online Publication Date	Mar 23, 2010
Volume number	96
Issue number	12
Type of Use	Thesis/Dissertation
Requestor type	Author (original article)
Format	Electronic
Portion	Figure/Table
Number of figures/tables	3
Title of your thesis / dissertation	II-VI semiconductor nanowire solar cells
Expected completion date	May 2012
Estimated size (number of pages)	100
Total	0.00 USD
Terms and Conditions	

American Institute of Physics -- Terms and Conditions: Permissions Uses

American Institute of Physics ("AIP") hereby grants to you the non-exclusive right and license to use and/or distribute the Material according to the use specified in your order, on a one-time basis, for the specified term, with a maximum distribution equal to the number that you have ordered. Any links or other content accompanying the Material are not the subject of this license.

SPRINGER LICENSE
TERMS AND CONDITIONS

May 29, 2012

This is a License Agreement between KAI WANG ("You") and Springer ("Springer") provided by Copyright Clearance Center ("CCC"). The license consists of your order details, the terms and conditions provided by Springer, and the payment terms and conditions.

All payments must be made in full to CCC. For payment instructions, please see information listed at the bottom of this form.

License Number	2870590920284
License date	Mar 16, 2012
Licensed content publisher	Springer
Licensed content publication	Springer eBook
Licensed content title	Three-Dimensional Photovoltaic Devices Based on Vertically Aligned Nanowire Array
Licensed content author	Kai Wang
Licensed content date	Aug 3, 2011
Type of Use	Thesis/Dissertation
Portion	Excerpts
Author of this Springer article	Yes and you are a contributor of the new work
Order reference number	
Title of your thesis / dissertation	II-VI semiconductor nanowire solar cells
Expected completion date	May 2012
Estimated size(pages)	100
Total	0.00 USD
Terms and Conditions	

Introduction

The publisher for this copyrighted material is Springer Science + Business Media. By clicking "accept" in connection with completing this licensing transaction, you agree that the following terms and conditions apply to this transaction (along with the Billing and Payment terms and conditions established by Copyright Clearance Center, Inc. ("CCC"), at the time that you opened your Rightslink account and that are available at any time at http://myaccount.copyright.com).

VITA

Kai Wang was born in Kaixian County, Chongqing Municipality, China. In 1999, he attended Southwest Jiaotong University in Chengdu, China, where he received his Bachelor's and Master's degree in Materials Science and Engineering in 2003 and 2006, respectively. After that, he was employed as a visiting scholar in Advanced Materials Research Institute at University of New Orleans (UNO). In January, 2008, he joined the Ph.D program of Engineering and Applied Science in UNO and, under the guidance of Dr.Weilie Zhou, conducted research on nanostructured materials and devices for environment monitoring and solar energy harvesting